Titre: Title:	Natural and mixed convection in a horizontal circular cylinder
Auteur: Author:	Min Zhao
Date:	1996
Type:	Mémoire ou thèse / Dissertation or Thesis
Référence: Citation:	Zhao, M. (1996). Natural and mixed convection in a horizontal circular cylinder [Ph.D. thesis, École Polytechnique de Montréal]. PolyPublie. https://publications.polymtl.ca/30754/

UNIVERSITÉ DE MONTRÉAL

NATURAL AND MIXED CONVECTION IN A HORIZONTAL CIRCULAR CYLINDER

MIN ZHAO
DÉPARTEMENT DE GÉNIE MÉCANIQUE
ÉCOLE POLYTECHNIQUE DE MONTRÉAL

THÈSE PRÉSENTÉE EN VUE DE L'OBTENTION
DU DIPLÔME DE PHILOSOPHIAE DOCTOR (Ph.D.)
(GÉNIE MÉCANIQUE)

JUIN 1996

ISBN 0-612-17816-1

Name MIN ZHAO

Dissertation Abstracts International is arranged by broad, general subject categories. Please select the one subject which most nearly describes the content of your dissertation. Enter the corresponding four-digit code in the spaces provided.

Mechanical Engineering
SUBJECT TERM

0548
SUBJECT CODE

U·M·I

Subject Categories

THE HUMANITIES AND SOCIAL SCIENCES

COMMUNICATIONS AND THE ARTS
Architecture 0729
Art History 0377
Cinema 0900
Dance 0378
Fine Arts 0357
Information Science 0723
Journalism 0391
Library Science 0399
Mass Communications 0708
Music 0413
Speech Communication 0459
Theater 0465

EDUCATION
General 0515
Administration 0514
Adult and Continuing 0516
Agricultural 0517
Art 0273
Bilingual and Multicultural 0282
Business 0688
Community College 0275
Curriculum and Instruction 0727
Early Childhood 0518
Elementary 0524
Finance 0277
Guidance and Counseling 0519
Health 0680
Higher 0745
History of 0520
Home Economics 0278
Industrial 0521
Language and Literature 0279
Mathematics 0280
Music 0522
Philosophy of 0998
Physical 0523
Psychology 0525
Reading 0535
Religious 0527
Sciences 0714
Secondary 0533
Social Sciences 0534
Sociology of 0340
Special 0529
Teacher Training 0530
Technology 0710
Tests and Measurements 0288
Vocational 0747

LANGUAGE, LITERATURE AND LINGUISTICS
Language
- General 0679
- Ancient 0289
- Linguistics 0290
- Modern 0291

Literature
- General 0401
- Classical 0294
- Comparative 0295
- Medieval 0297
- Modern 0298
- African 0316
- American 0591
- Asian 0305
- Canadian (English) 0352
- Canadian (French) 0355
- English 0593
- Germanic 0311
- Latin American 0312
- Middle Eastern 0315
- Romance 0313
- Slavic and East European 0314

PHILOSOPHY, RELIGION AND THEOLOGY
Philosophy 0422
Religion
- General 0318
- Biblical Studies 0321
- Clergy 0319
- History of 0320
- Philosophy of 0322

Theology 0469

SOCIAL SCIENCES
American Studies 0323
Anthropology
- Archaeology 0324
- Cultural 0326
- Physical 0327

Business Administration
- General 0310
- Accounting 0272
- Banking 0770
- Management 0454
- Marketing 0338

Canadian Studies 0385
Economics
- General 0501
- Agricultural 0503
- Commerce-Business 0505
- Finance 0508
- History 0509
- Labor 0510
- Theory 0511

Folklore 0358
Geography 0366
Gerontology 0351
History
- General 0578
- Ancient 0579
- Medieval 0581
- Modern 0582
- Black 0328
- African 0331
- Asia, Australia and Oceania 0332
- Canadian 0334
- European 0335
- Latin American 0336
- Middle Eastern 0333
- United States 0337

History of Science 0585
Law 0398
Political Science
- General 0615
- International Law and Relations 0616
- Public Administration 0617

Recreation 0814
Social Work 0452
Sociology
- General 0626
- Criminology and Penology 0627
- Demography 0938
- Ethnic and Racial Studies 0631
- Individual and Family Studies 0628
- Industrial and Labor Relations 0629
- Public and Social Welfare 0630
- Social Structure and Development 0700
- Theory and Methods 0344

Transportation 0709
Urban and Regional Planning 0999
Women's Studies 0453

THE SCIENCES AND ENGINEERING

BIOLOGICAL SCIENCES
Agriculture
- General 0473
- Agronomy 0285
- Animal Culture and Nutrition 0475
- Animal Pathology 0476
- Food Science and Technology 0359
- Forestry and Wildlife 0478
- Plant Culture 0479
- Plant Pathology 0480
- Plant Physiology 0817
- Range Management 0777
- Wood Technology 0746

Biology
- General 0306
- Anatomy 0287
- Biostatistics 0308
- Botany 0309
- Cell 0379
- Ecology 0329
- Entomology 0353
- Genetics 0369
- Limnology 0793
- Microbiology 0410
- Molecular 0307
- Neuroscience 0317
- Oceanography 0416
- Physiology 0433
- Radiation 0821
- Veterinary Science 0778
- Zoology 0472

Biophysics
- General 0786
- Medical 0760

EARTH SCIENCES
Biogeochemistry 0425
Geochemistry 0996
Geodesy 0370
Geology 0372
Geophysics 0373
Hydrology 0388
Mineralogy 0411
Paleobotany 0345
Paleoecology 0426
Paleontology 0418
Paleozoology 0985
Palynology 0427
Physical Geography 0368
Physical Oceanography 0415

HEALTH AND ENVIRONMENTAL SCIENCES
Environmental Sciences 0768
Health Sciences
- General 0566
- Audiology 0300
- Chemotherapy 0992
- Dentistry 0567
- Education 0350
- Hospital Management 0769
- Human Development 0758
- Immunology 0982
- Medicine and Surgery 0564
- Mental Health 0347
- Nursing 0569
- Nutrition 0570
- Obstetrics and Gynecology 0380
- Occupational Health and Therapy 0354
- Ophthalmology 0381
- Pathology 0571
- Pharmacology 0419
- Pharmacy 0572
- Physical Therapy 0382
- Public Health 0573
- Radiology 0574
- Recreation 0575
- Speech Pathology 0460
- Toxicology 0383

Home Economics 0386

PHYSICAL SCIENCES
Pure Sciences
Chemistry
- General 0485
- Agricultural 0749
- Analytical 0486
- Biochemistry 0487
- Inorganic 0488
- Nuclear 0738
- Organic 0490
- Pharmaceutical 0491
- Physical 0494
- Polymer 0495
- Radiation 0754

Mathematics 0405
Physics
- General 0605
- Acoustics 0986
- Astronomy and Astrophysics 0606
- Atmospheric Science 0608
- Atomic 0748
- Electronics and Electricity 0607
- Elementary Particles and High Energy 0798
- Fluid and Plasma 0759
- Molecular 0609
- Nuclear 0610
- Optics 0752
- Radiation 0756
- Solid State 0611

Statistics 0463

Applied Sciences
Applied Mechanics 0346
Computer Science 0984
Engineering
- General 0537
- Aerospace 0538
- Agricultural 0539
- Automotive 0540
- Biomedical 0541
- Chemical 0542
- Civil 0543
- Electronics and Electrical 0544
- Heat and Thermodynamics 0348
- Hydraulic 0545
- Industrial 0546
- Marine 0547
- Materials Science 0794
- Mechanical 0548
- Metallurgy 0743
- Mining 0551
- Nuclear 0552
- Packaging 0549
- Petroleum 0765
- Sanitary and Municipal 0554
- System Science 0790

Geotechnology 0428
Operations Research 0796
Plastics Technology 0795
Textile Technology 0994

PSYCHOLOGY
General 0621
Behavioral 0384
Clinical 0622
Developmental 0620
Experimental 0623
Industrial 0624
Personality 0625
Physiological 0989
Psychobiology 0349
Psychometrics 0632
Social 0451

Nom MIN ZHAO

Dissertation Abstracts International est organisé en catégories de sujets. Veuillez s.v.p. choisir le sujet qui décrit le mieux votre thèse et inscrivez le code numérique approprié dans l'espace réservé ci-dessous.

Génie mécanique
SUJET

0548 U·M·I
CODE DE SUJET

Catégories par sujets

HUMANITÉS ET SCIENCES SOCIALES

COMMUNICATIONS ET LES ARTS
Architecture 0729
Beaux-arts 0357
Bibliothéconomie 0399
Cinéma 0900
Communication verbale 0459
Communications 0708
Danse 0378
Histoire de l'art 0377
Journalisme 0391
Musique 0413
Sciences de l'information 0723
Théâtre 0465

ÉDUCATION
Généralités 515
Administration 0514
Art 0273
Collèges communautaires 0275
Commerce 0688
Économie domestique 0278
Éducation permanente 0516
Éducation préscolaire 0518
Éducation sanitaire 0680
Enseignement agricole 0517
Enseignement bilingue et multiculturel 0282
Enseignement industriel 0521
Enseignement primaire. 0524
Enseignement professionnel 0747
Enseignement religieux 0527
Enseignement secondaire 0533
Enseignement spécial 0529
Enseignement supérieur 0745
Évaluation 0288
Finances 0277
Formation des enseignants 0530
Histoire de l'éducation 0520
Langues et littérature 0279
Lecture 0535
Mathématiques 0280
Musique 0522
Orientation et consultation 0519
Philosophie de l'éducation 0998
Physique 0523
Programmes d'études et enseignement 0727
Psychologie 0525
Sciences 0714
Sciences sociales 0534
Sociologie de l'éducation 0340
Technologie 0710

LANGUE, LITTÉRATURE ET LINGUISTIQUE
Langues
- Généralités 0679
- Anciennes 0289
- Linguistique 0290
- Modernes 0291

Littérature
- Généralités 0401
- Anciennes 0294
- Comparée 0295
- Médiévale 0297
- Moderne 0298
- Africaine 0316
- Américaine 0591
- Anglaise 0593
- Asiatique 0305
- Canadienne (Anglaise) 0352
- Canadienne (Française) 0355
- Germanique 0311
- Latino-américaine 0312
- Moyen-orientale 0315
- Romane 0313
- Slave et est-européenne 0314

PHILOSOPHIE, RELIGION ET THÉOLOGIE
Philosophie 0422
Religion
- Généralités 0318
- Clergé 0319
- Études bibliques 0321
- Histoire des religions 0320
- Philosophie de la religion 0322

Théologie 0469

SCIENCES SOCIALES
Anthropologie
- Archéologie 0324
- Culturelle 0326
- Physique 0327

Droit 0398
Économie
- Généralités 0501
- Commerce-Affaires 0505
- Économie agricole 0503
- Économie du travail 0510
- Finances 0508
- Histoire 0509
- Théorie 0511

Études américaines 0323
Études canadiennes 0385
Études féministes 0453
Folklore 0358
Géographie 0366
Gérontologie 0351
Gestion des affaires
- Généralités 0310
- Administration 0454
- Banques 0770
- Comptabilité 0272
- Marketing 0338

Histoire
- Histoire générale 0578
- Ancienne 0579
- Médiévale 0581
- Moderne 0582
- Histoire des noirs 0328
- Africaine 0331
- Canadienne 0334
- États-Unis 0337
- Européenne 0335
- Moyen-orientale 0333
- Latino-américaine 0336
- Asie, Australie et Océanie 0332

Histoire des sciences 0585
Loisirs 0814
Planification urbaine et régionale 0999
Science politique
- Généralités 0615
- Administration publique 0617
- Droit et relations internationales 0616

Sociologie
- Généralités 0626
- Aide et bien-être social 0630
- Criminologie et établissements pénitentiaires 0627
- Démographie 0938
- Études de l' individu et de la famille 0628
- Études des relations interethniques et des relations raciales 0631
- Structure et développement social 0700
- Théorie et méthodes. 0344
- Travail et relations industrielles 0629

Transports 0709
Travail social 0452

SCIENCES ET INGÉNIERIE

SCIENCES BIOLOGIQUES
Agriculture
- Généralités 0473
- Agronomie. 0285
- Alimentation et technologie alimentaire 0359
- Culture 0479
- Élevage et alimentation 0475
- Exploitation des pâturages 0777
- Pathologie animale 0476
- Pathologie végétale 0480
- Physiologie végétale 0817
- Sylviculture et faune 0478
- Technologie du bois 0746

Biologie
- Généralités 0306
- Anatomie 0287
- Biologie (Statistiques) 0308
- Biologie moléculaire 0307
- Botanique 0309
- Cellule 0379
- Écologie 0329
- Entomologie 0353
- Génétique 0369
- Limnologie 0793
- Microbiologie 0410
- Neurologie 0317
- Océanographie 0416
- Physiologie 0433
- Radiation 0821
- Science vétérinaire 0778
- Zoologie 0472

Biophysique
- Généralités 0786
- Medicale 0760

SCIENCES DE LA TERRE
Biogéochimie 0425
Géochimie 0996
Géodésie 0370
Géographie physique 0368
Géologie 0372
Géophysique 0373
Hydrologie 0388
Minéralogie 0411
Océanographie physique 0415
Paléobotanique 0345
Paléoécologie 0426
Paléontologie 0418
Paléozoologie 0985
Palynologie 0427

SCIENCES DE LA SANTÉ ET DE L'ENVIRONNEMENT
Économie domestique 0386
Sciences de l'environnement 0768
Sciences de la santé
- Généralités 0566
- Administration des hôpitaux 0769
- Alimentation et nutrition 0570
- Audiologie 0300
- Chimiothérapie 0992
- Dentisterie 0567
- Développement humain 0758
- Enseignement 0350
- Immunologie 0982
- Loisirs 0575
- Médecine du travail et thérapie 0354
- Médecine et chirurgie 0564
- Obstétrique et gynécologie 0380
- Ophtalmologie 0381
- Orthophonie 0460
- Pathologie 0571
- Pharmacie 0572
- Pharmacologie 0419
- Physiothérapie 0382
- Radiologie 0574
- Santé mentale 0347
- Santé publique 0573
- Soins infirmiers 0569
- Toxicologie 0383

SCIENCES PHYSIQUES
Sciences Pures
Chimie
- Généralités 0485
- Biochimie 487
- Chimie agricole 0749
- Chimie analytique 0486
- Chimie minérale 0488
- Chimie nucléaire 0738
- Chimie organique 0490
- Chimie pharmaceutique 0491
- Physique 0494
- Polymères 0495
- Radiation 0754

Mathématiques 0405
Physique
- Généralités 0605
- Acoustique 0986
- Astronomie et astrophysique 0606
- Électronique et électricité 0607
- Fluides et plasma 0759
- Météorologie 0608
- Optique 0752
- Particules (Physique nucléaire) 0798
- Physique atomique 0748
- Physique de l'état solide 0611
- Physique moléculaire 0609
- Physique nucléaire 0610
- Radiation 0756

Statistiques 0463

Sciences Appliqués Et Technologie
Informatique 0984
Ingénierie
- Généralités 0537
- Agricole 0539
- Automobile 0540
- Biomédicale 0541
- Chaleur et thermodynamique 0348
- Conditionnement (Emballage) 0549
- Génie aérospatial 0538
- Génie chimique 0542
- Génie civil 0543
- Génie électronique et électrique 0544
- Génie industriel 0546
- Génie mécanique 0548
- Génie nucléaire 0552
- Ingénierie des systèmes 0790
- Mécanique navale 0547
- Métallurgie 0743
- Science des matériaux 0794
- Technique du pétrole 0765
- Technique minière 0551
- Techniques sanitaires et municipales 0554
- Technologie hydraulique 0545

Mécanique appliquée 0346
Géotechnologie 0428
Matières plastiques (Technologie) 0795
Recherche opérationnelle 0796
Textiles et tissus (Technologie) 0794

PSYCHOLOGIE
Généralités 0621
Personnalité 0625
Psychobiologie 0349
Psychologie clinique 0622
Psychologie du comportement 0384
Psychologie du développement 0620
Psychologie expérimentale 0623
Psychologie industrielle 0624
Psychologie physiologique 0989
Psychologie sociale 0451
Psychométrie 0632

UNIVERSITÉ DE MONTRÉAL

ÉCOLE POLYTECHNIQUE DE MONTRÉAL

Cette thèse intitulée:

NATURAL AND MIXED CONVECTION IN A HORIZONTAL CIRCULAR CYLINDER

Présentée par: ZHAO Min

en vue de l'obtention du diplôme de: Philosophiae Doctor

a été dûment acceptée par le jury d'examen constitué de:

M. PRUD'HOMME Michel, Ph.D., Président

M. ROBILLARD Luc, Ph.D., membre et directeur de recherche

M. TEYSSEDOU Alberto, Ph.D., membre

M. TANGBORN Andrew, Ph.D., membre

Dedicated to my wife, my daughter and my parents

ACKNOWLEDGEMENTS

First of all, I would like to express my greatest appreciation to professor *Luc Robillard*, my Ph.D. program supervisor, for his encouragement and guidance in all phases of my graduate studies in the Department of Mechanical Engineering, Ecole Polytechnique, University of Montreal in past five years. I consider it a great pleasure to study and work under his supervision and consultant, and gained a lot from so much discussion between us on research subjects. I believe that his profound interpretation to the phenomena of nature and ingenuity in doing scientific research will considerably influence my entire life of career.

Right now is also a good chance to say thanks to many professors, staff, fellow graduate students and friends in the department for their help in various form. In particular, my sincere thanks go to professor T. Hung Nguyen for his precious advice and personal help in my first year of Ph.D. program. Furthermore I would like to mention the continuous support I received from Mr. Alain Roubidou, an excellent computer technician in the department, in effectively using daily-changing software and hardware of computer.

Finally, acknowledgement is due to NSERC & FCAR for its financial support to this research activity as well as the Department of Mechanical Engineering at Ecole Polytechnique that provides a dynamic and scientific atmosphere in addition to strong and advanced computer facilities.

RÉSUMÉ

Le problème de la convection et de la stabilité dans un cylindre est d'un intérêt théorique et pratique dans les phénomènes de transport en milieux poreux et fluides, tant en sciences fondamentales qu'en ingénierie.

La présente thèse expose les travaux de recherche sur le transfert de chaleur et l'écoulement des fluides en milieux poreux ou fluide, confiné dans un cylindre horizontal en rotation avec une vitesse angulaire rapide, faible et nulle. Les principales parties développées dans cette dissertation sont:

- but et position du présent problème physique
- modèle mathématique du transfert de chaleur à travers un cylindre
- développement des méthodes numériques
- convection mixte dans un cylindre en rotation lente
- convection naturelle dans un cylindre en rotation rapide
- instabilité dans un cylindre non rotatif

L'écoulement dans le cylindre est supposé bidimensionnel dans le plan $(r,\ \theta)$ et des conditions périodiques sont prises en considération dans la direction θ. Puisque les études originales en question dans cette thèse ne peuvent satisfaire la symétrie par rapport au diamètre vertical, symétrie que l'on oblient quand la gravité terrestre seule est considérée, le cylindre entier doit être maillé comme domaine physique. Les trois cas suivants sont étudiés:

D'abord, nous abordons le comportement de la convection naturelle et de la convection mixte dans un cylindre horizontal en rotation, contenant un milieu poreux

ou fluide et soumis à la condition pariétale isotherme et à un puits thermique uniformément distribué. Ce genre de problème est équivalent au cas où, aucun puit ou source n'étant présent, la température à la frontière est croissante dans le temps à un taux constant. Un régime de rotation faible est envisagé. Nous nous sommes proposés d'examiner exclusivement l'interaction entre la rotation autour d'un axe horizontal et la force gravitationnelle. Quoique les milieux fluide et poreux sont décrits à l'aide des équations de mouvement différentes et possèdent des propriétés thermiques et dynamiques différentes (par exemple, en milieu fluide, la résistance au mouvement est engendrée par la paroi solide tandis qu'en milieu poreux, cette résistance est produite en tout point par la matrice solide), ces milieux répondent à la même équation adimensionnelle d'énergie et possèdent la même configuration géométrique. Un comportement qualitativement similaire sous les mêmes conditions est donc prévisible. L'interaction entre les rouleaux convectifs obtenus pour la situation standard de la convection naturelle et les effets de la vitesse de rotation est étudiée numériquement et analytiquement. Pour la convection d'amplitude finie, les résultats numériques basés sur la méthode des différences finies couvrent une large gamme des nombres de Rayleigh et de Péclet. En outre, une méthode de perturbations régulières est utilisée pour étudier la rotation et valider les résultats numériques, ces derniers s'accordant bien avec cette solution analytique. Les deux méthodes de résolution sont appliquées tant au milieu poreux isotrope qu'au milieu fluide.

Pour le cas, d'un milieu poreux isotrope, les deux méthodes de résolution révèlent toutes deux qu'une grande partie du fluide saturant ne participe pas à la rotation à faible vitesse. Donc, la fonction de courant au centre peut largement différer de zéro. Cependant, avec l'augmentation de la vitesse angulaire, un régime de rotation solide se développe, régime pour lequel le transfert de chaleur par convection est éventuellement réduit à zéro. De même, pour un milieu fluide, un écoulement net

relatif à la paroi du cylindre est obtenu à faible vitesse de rotation (régime de cisaillement) et une rotation solide apparaît à des vitesses angulaires élevées (régime de rotation de solide) pour lesquelles les effets rotationnels sur la convection réduisent presque le transfert de chaleur au niveau de la conduction pure. La différence entre les deux milieux réside dans le fait que l'écoulement net en milieu fluide enregistre une chute soudaine drastique à des nombres élevés de Rayleigh, accompagnée d'un comportement oscillatoire, lequel est occasionné par le terme inertiel du milieu fluide, tandis que la transition au régime de rotation solide apparait graduellement en milieu poreux sans qu'aucun comportement oscillatoire (transitoire) ne soit detecté.

Ensuite, nous avons étudié la convection de Bénard dans un cylindre en rotation rapide, dans lequel est confiné un milieu poreux isotrope / anisotrope saturé par un fluide; le cylindre est soumis à une condition pariétale isotherme et à un puits thermique uniformément distribué. Nous considérons la situation où la rotation est rapide et où seule la force centrifuge intervient, la gravité terrestre étant supposée négligeable. Dans ces conditions, le gradient de densité en conduction est dirigé vers le centre géométrique du cylindre et la force centrifuge agit sur le fluide saturant dans la direction opposée. Un tel équilibre de forces est potentiellement instable et des cellules convectives sont susceptibles d'apparaître au-delà d'un nombre de Rayleigh critique. Pour le cas isotrope, une étute anaytique de la stabilité linéaire a permis de prédire le nombre de Rayleigh critique pour l'apparition de la convection et les résultats sont comparés avec ceux obtenus numériquement. De plus, les résultats obtenus pour la convection d'amplitude finie sont consistants avec ceux concernant l'apparition de la convection. La présente invertigation définit donc l'existence d'un seuil $Ra_c = 348$ au-delà duquel la convection apparaît et où il est possible d'avoir des solutions multiples pour des nombres de Rayleigh dépassant largement cette valeur critique. Une structure d'écoulement à quatre cellules est observée à l'apparition de la convection. Par contre, une solution stable à des nombres élevés de Ra contient

un plus grand nombre de cellules. L'anisotropie en perméabilité a un grand effet sur Ra_c, avec la possibilité de seuils au-dessous de 348. En outre, la premiere configuration de l'écoulement relatif au milieu poreux anisotrope qui apparaît au-delà du seuil critique contient même six cellules, plutôt que quatre, si le rapport des perméabilités est suffisamment éloigné de l'unité. Enfin, à la différence du cas isotrope où aucune condition physique ne peut imposer une quelconque position angulaire à la configuration de l'écoulement, ce dernier en situation anisotrope prend toujours une position angulaire qui assure la symétrie par rapport aux axes principaux.

Finalement, nous avons étudié les instabilités de Bénard dans un cylindre non rotatif, contenant un milieu poreux isotrope / anisotrope et soumis à une distribution sinusoïdale de la température sur sa frontière, et ce en présence de la gravité terrestre. Une telle distribution de température est équivalente à une stratification thermique linéaire de l'environnement dans une direction donnée. L'application de la température maximale au bas du cylindre ($\theta_0 = 0$, chauffage par le bas) constitue un cas particulier. La stratification thermique imposée sur la paroi circulaire est alors dirigée verticalement et par conséquent, la direction du gradient de densité est opposée à celle du champ gravitationnel, donnant lieu à un équilibre de forces potentiellement instable en conduction pure. Pour le cas où le milieu poreux est isotrope et chauffé pas le bas, la valeur critique du nombre de Rayleigh pour l'apparition des cellules de Bénard est approximativement égale à 23.3. Les deux types suivants de configuration de l'écoulement sont observés: une configuration de l'écoulement constituée de deux cellules convectives, symetriques rapport au diamètre vertical et une autre configuration de l'écoulement, centro-symétrique, contenant trois cellules. Aussi, les résultats numériques pour la convection d'amplitude finie à $\theta_0 = 0$ démontrent que les configurations d'écoulement à deux ou trois cellules de convection sont stables. Des résultats numériques sont aussi obtenus à différents nombres de Rayleigh pour une position arbitraire de la température maximale sur la frontière.

L'écoulement résultant est unicellulaire, à moins que la température maximum ne se situe au voisinage de la région instable ($\theta_0 = 0$). Un excellent accord est observé entre les résultats donnés par l'analyse de la stabilité linéaire, les résultats obtenus par la méthode de perturbation régulière et ceux obtenus par les simulations numériques.

Pour le cas anisotrope, la discussion est limitée seulement à la condition de chauffage par le bas. Le rapport des perméabilités R et l'angle de axes principaux θ_k ont tous deux une grande influence sur les valeurs critiques du nombre de Rayleigh et les modèle d'écoulement discutés précédemment. La valeur critique minimale de Ra est atteinte lorsque la matrice poreuse est orientée de manière que l'axe principal ayant la perméabitité la plus élevée corresponde à la direction verticale ($R < 1, \theta_k = \pi/2$). De l'analyse de la stabilité linéaire, nous avons trouvé que le nombre de Rayleigh critique Ra_c correspondant à $R = 0.125$ et $\theta_k = 90^0$ est d'environ 20, valeur inférieure au seuil correspondant à la situation isotrope. La structure d'écoulement au seuil de la convection telle que prédite par l'analyse de la stabilité linéaire comporte 3 cellules ou 2 cellules, selon la valeur θ_k. A la différence du milieu poreux isotrope, le nombre de Rayleigh critique Ra_c n'a pas une valeur fixe mais est une fonction de θ_k et de R. La convection d'amplitude finie est investiguée numériquement. Les résultats de l'analyse de stabilité linéaire s'accordent bien avec ceux donnés par l'approche numérique.

ABSTRACT

The problem of convection and stability in a circular cylinder has a focal interest following theoretical as well as practical relevance of transport phenomena in porous and fluid media to fundamental science and engineering applications.

This dissertation presents the research work in the subject of heat transfer and fluid flow in fluid / porous medium confined in a horizontal circular cylinder rotating in a fast, low and zero angular speed. The main contents of the dissertation include:

- motivation and background of the present study
- mathematical model for heat transfer in a cylinder
- numerical simulation development
- mixed convection in a low rotation cylinder
- natural convection in a fast rotation cylinder
- instability in a non-rotating cylinder

The flow in the cylinder is assumed to be two-dimensional in a $(r,\ \theta)$ plane, and periodicity conditions in θ-direction are taken into consideration. Since the particular studies involved in this work preclude any symmetry with respect to the vertical diameter where terrestrial gravity is involved, the whole cylinder as computational domain is fully considered in the present work. The three following cases are investigated.

The behavior of natural and mixed convection in a low rotation horizontal cylinder filled with an isotropic porous / fluid medium with isothermal boundary condition and uniformly distributed heat sink is first studied. This kind of problem

is equivalent to the case without heat sink or source and with a boundary temperature increasing at a steady rate with time. Weak rotation regime only is undertaken, for which the force field is terrestrial gravity only. It is expected to examine closely the interaction between rotation about a horizontal axis and the gravity force. Even though the fluid and porous media are described by different momentum equations and have different thermal and dynamic properties (eg., the resistance to motion for the fluid medium originates from the solid boundary whereas that for a porous medium takes place everywhere of whole matrix, the inertia term is involved for fluid medium and neglected for porous medium), they still have the same dimensionless energy equations and are confined within the same geometry. Therefore, a qualitatively similar behaviour under same conditions is expected. The interaction between convective rolls as obtained from standard free convection case and the effects of rotation speed are studied numerically and analytically. For the finite amplitude convection, the numerical results based on finite difference scheme cover a broad range of Rayleigh and Peclet numbers. In addition, a regular perturbation method is used to study the incipient rotation and validate the numerical approach. Results from both approaches coincide. Those approaches are applied both to the isotropic porous medium and to the fluid medium.

For the isotropic porous medium case, both approaches reveal that a large part of the saturated fluid does not participate to rotation at low rotation speed. Thus the stream function at the center may differ largely from zero. However, with increasing angular velocity, the fluid is gradually entrained and a solid body rotation regime develops for which the convective heat transfer is eventually reduced to zero. Similarly, for the fluid medium case, a net flow relative to the cylinder boundary is found at low rotation speed (shear flow regime) and a solid body rotation occur at larger angular velocities (solid body rotation regime) in which the rotational effects on convection are found to reduce the heat transfer almost to the pure conduc-

tion level. The difference between both media is that the net flow in fluid medium encounters a drastic drop at high Rayleigh number due to the oscillating behavior caused by the inertial term in fluid medium, whereas the transition to solid body rotation regime occurs gradually for the porous medium without oscillating (unsteady) behavior.

Then Bénard convection in a fast rotation isotropic / anisotropic fluid saturated porous cylinder with isothermal condition on the boundary and uniformly distributed heat sink is studied. In the situation of fast rotation, only the centrifugal force is involved, the terrestrial gravity being assumed negligible. With those conditions, the direction of the pure conduction density gradient is toward the geometric center of cylinder and the centrifugal force field is acting on fluid in the opposite direction. Such a force balance is potentially unstable and convective cells are expected to occur beyond a critical Rayleigh number. For the isotropic case, a linear stability analysis solved analytically was used to predict the critical Rayleigh number for incipient convection and the results are compared with those from a linear stability analysis solved numerically. Moreover, results from finite amplitude convection are consistent with those concerning incipient convection. The results of the present investigation reveal that there exists a threshold $Ra_c = 348$ beyond which convection takes place and multiple solutions are possible for Rayleigh numbers well above this critical value. Only a 4-cell structure flow occurs at the incipient convection and a stable solution at high Ra numbers will contain more cells. Anisotropy of permeability is found to have a strong effect on Ra_c, with the possibility of thresholds below 348. Moreover the first flow configuration for anisotropic porous medium to appear may even contain six cells instead of four cells if the permeability ratio is far enough from unity. Also, to the difference of the isotropic case where there is no physical requirement on angular position of the flow pattern, the non-isotropic flow pattern takes an angular position that ensures symmetry with respect to the

principal axes.

Final investigation is on Bénard instabilities in a non-rotating isotropic / anisotropic porous cylinder having sinusoidally distributed temperature on the boundary in the presence of terrestrial gravity. Such a distribution in temperature is equivalent to a linear thermal stratification of the surroundings in a given direction. A particular case is that the maximum temperature is at the bottom ($\theta_0 = 0$, bottom heating). The thermal stratification imposed on the circular boundary is then in the vertical direction and consequently the direction of density gradient is opposite to the terrestrial gravity, giving rise to a potentially unstable force balance in pure conduction. For the isotropic porous medium with the bottom heating, the critical value of Rayleigh number for Bénard cells to appear is found to be approximately 23.3, with two types of flow configurations: a flow configuration involving two convective cells, symmetric with respect to the vertical diameter, and a centrosymmetric flow configuration containing three cells. Also numerical results for finite amplitude convection at $\theta_0 = 0$ show that both 2-cell and 3-cell are stable configurations. Numerical solutions are also obtained at different Rayleigh numbers for an arbitrary position of the maximum temperature on the boundary. The flow is then unicellular unless the maximum temperature lies somewhere in the neighborhood of the unstable location ($\theta_0 = 0$). Results from linear stability analysis, regular perturbation and numerical simulation are found to be in good agreement.

For the anisotropic case, the discussion is limited to bottom heating only. Both the ratio of permeability R and the angle of the principal axes θ_k have a strong influence on the critical values of Rayleigh number and the initial flow patterns. The minimum critical Ra is achieved when the porous matrix is arranged such that the principal axis with higher permeability is in the vertical direction ($R < 1$, $\theta_k = \pi/2$). It is found from the linear stability analysis that Ra_c corresponding to $R = 0.125$, $\theta_k = 90^0$ is about 20, a value lower than the threshold for the isotropic case. No

double eigenvalues are obtained. The initial flow pattern predicted by the linear stability analysis has either a 3-cell structure or a 2-cell structure according to the value of θ_k. To the difference of the isotropic porous medium, the critical Rayleigh number Ra_c does not have a fixed value but is function of θ_k and R. Finite amplitude convection is investigated numerically and results from linear stability analysis and numerical approach agree well.

CONDENSÉ EN FRANÇAIS

1. INTRODUCTION (Chapitre 1)

L'objet principal de cette thèse consiste à étudier le comportement de l'écoulement et du transfert de chaleur dans le cas d'un fluide ou d'un milieu poreux de forme cylindrique qui peut être en rotation autour d'un axe et de déterminer les effets relatifs de la convection naturelle et de la rotation.

La convection naturelle et mixte dans une enceinte cylindrique circulaire et le transfert de chaleur qui s'y manifeste ont fait l'objet d'un grand nombre d'investigations jusqu'à maintenant à cause de l'importance de ce problème, tout du point de vue fondamental que pratique. Beaucoup de ces investigations couvrent les domaines des mathématiques appliquées, de la physique de base, de la géophysique de même que des domaines d'application technologique comme ceux de la croissance cristalline, de l'industrie alimentaire, des systèmes de refroidissement d'appareils électroniques, des systèmes de ventilation et de climatisation pour bàtiments sans compter le domaine des sciences géophysiques et des prévisions metéorologiques. En plus, ajoutons que les écoulements observés sont comparables à ceux que l'on retrouve dans des modélisations relevent de l'astrophysique.

Dans le présent travail, nous examinons analytiquement et numériquement la convection engendrée par un champ de force dans un milieu poreux isotrope ou anisotrope ou dans un milieu fluide contenu dans un cylindre tournant autour de son axe (axe horizontal, dans le cas de la gravité terrestre). Nous étudions aussi l'instabilité de type Bénard dans la cas d'un milieu poreux isotrope et anisotrope de forme cylindrique en rotation rapide ou sans rotation, lorsque le gradient de masse volumique est opposé à la force massique. Evidemment, en situation anisotrope, l'instabilité devient plus complexe à cause la variation de perméabilité avec la di-

rection.

Les problèmes de convection mentionnés précédemment impliquent l'étude du cylindre tout entier comme domaine d'écoulement. Celà, par contraste avec la plupart des études précédentes sur le sujet où l'hypothèse d'une symétrie par rapport au diamètre vertical pouvait être invoquée pour réduire le domaine à un demi-cylindre. Dans le cas du cylindre tout entier, lorsque des différences finies sont utilisées avec coordonnées cylindriques, le centre du cylindre devient une singularité mathématique qui doit être traitée convenablement de façon à ce que la région centrale devienne transparente à l'écoulement, peu importe sa direction. Bien que les conditions aux limites et les milieux considérés varient d'un cas à l'autre, les différents sujets traités dans cette thèse ont une géometrie commune, le cylindre circulaire dans son entier; les différents sujets sont 1^0 la convection mixte avec rotation lente impliquant un milieu poreux isotrope ou un milieu fluide, 2^0 la rotation rapide d'un milieu poreux isotrope ou anisotrope, 3^0 la convection sans rotation dans un milieu poreux isotrope ou anisotrope avec une distribution sinusoïdale de température comme condition limite thermique. La bibliographie pour chacun de ces sujets est traitée séparément.

Convection mixte d'un cylindre en rotation lente

La convection naturelle dans des systèmes en rotation est impliquée dans de nombreux procédés industriels où le transfert de chaleur est un facteur important. En conséquence, on a accordé beaucoup d'attention à ce problème dans les années récentes. La rotation autour d'un axe vertical a été largement étudiée. Cependant la rotation autour d'un axe horizontal, l'a été beaucoup moins.

Selon les résultats des édudes passées sur la rotation lente autour d'un axe horizontal, dans le cas d'une géométrie annulaire, une masse importante de fluide demeure attachée au vecteur gravité terrestre et ni prend pas part à la rotation solide. La convection libre affecte le transfert de chaleur uniquement aux rotations

très lentes et le fait d'augmenter la vitesse angulaire du systeme décroît le transfert de chaleur jusqu'à la conduction pure.

Convection naturelle et rotation rapide

Quelques travaux antérieurs expérimentaux et théoriques ont traité de la convection naturelle dans un cylindre en rotation rapide. L'effet de la gravité terrestre était présent. Cependant les résultats de ces travaux donnent la tendance asymptotique en rotation très rapide pour laquelle la gravité radiale devient predominante. Les solutions dépendent grandement des conditions thermiques imposées aux parois et le transfert de chaleur est augmenté considérablement par la rotation. Un second nombre de Rayleigh basé sur la gravité radiale est introduit en plus du nombre de Rayleigh basé sur la gravité terrestre. Quand la gravité terrestre est négligée, des écoulements permanents se produisent, relativement à un système de coordonnées en rotation avec le cylindre. Il existe un nombre de Rayleigh critique au-dessus duquel un écoulement constitué de deux cellules convectives s'installe. Pour des nombres de Rayleigh beaucoup plus élevés que ce nombre de Rayleigh critique, la structure de l'écoulement peut être nulticellulaire.

Convection naturelle dans un cylindre sans rotation

Dans ce cas, une distribution de température à la frontière sous la forme $T_w = \cos(\theta - \theta_0)$, où θ_0 est l'angle de phase, est imposée. Cette distribution est équivalente à celle imposée par un environnement stratifié thermiquement entourant le cylindre. Il y a une valeur de θ_0 pour laquelle le grandient de température est vers le haut (chauffage par le bas) et pour laquelle le système devient potentiellement instable. Pour le cylindre rempli d'un fluide, l'amorce du mouvement se produit alors pour une valeur critique de Rayleigh égale à 576. La structure de l'écoulement pour toutes conditions consiste en une seule cellule de convection.

Les travaux anterieurs sur le transfert de chaleur convectif d'un milieu poreux ont porté sur le milieu poreux isotrope et relativement peu études ont été consacrées au milieu anisotrope. Il en existe néanmoins impliquant l'anisotropie dans le domaine de la géologie. Notons toutefois que la plupart des travaux précédents sur le milieu anisotrope ont été limités aux géométries comme la cavité réctangulaire ou les couches horizontales. On y mentionne que l'inclination des axes principaux influence fortement la structure de l'écoulement et le transfert de chaleur.

2. MODELE MATHÉMATIQUE (Chapitre 2)

Nous rappelons que la géométrie considérée est un cylindre circulaire (avec axe horizontal dans le cas de la gravité terrestre) ayant une longueur théoriquement infinie. L'écoulement est supposé bidimensionnel dans le plan vertical (r', θ'). Les équations gouvernantes du problème considéré peuvent être exprimées dans l'un ou l'autre de deux systèmes de coordonnées, l'un fixe par rapport au cylindre en rotation et l'autre fixe par rapport à la gravité terrestre $\mathbf{g}'$. Les équations gouvernantes basées sur l'un ou l'autre des deux systèmes de coordonnées peuvent être utilisées indifféremment dans l'approche numérique. Quand la vitesse angulaire est faible, le premier ensemble d'équations donne lieu à une solution dependante du temps alors que l'autre ensemble produit une solution permanente. Les résultats des deux approches sont identiques lorsque transformés adéquatement.

Bien que les équations de mouvement pour le milieu fluide et le milieu poreux saturé impliquent deux champs de force, la gravité terrestre et la gravité radiale, nous ne voulons pas traiter les cas où les deux forces interviennent simultanément, mais nous voulons limiter notre investigation aux cas asymptotiques pour lesquels l'une ou l'autre peut être négligée. Il est en effet préférable de comprendre à fond ces cas asymptopiques avant d'aborder les cas intermédiaires. Par surcroit, les cas intermédiaires sont dépendant du temps alors que les cas asymtopiques sont perma-

nents.

Il est avantageux d'aborder numériquement le problème d'un cylindre en rotation lente par un système de coordonnées fixe par rapport à la paroi. On obtient alors un champ d'écoulement relatif $\mathbf{V}'$. Cet écoulement est produit par la convection et il correspond au champ d'écoulement tel qu'il se présente pour un observateur solidaire de la frontière en rotation.

Les équations gouvernantes du milieu fluide sont les équations de continuité, de mouvement et d'énergie, alors que celles du milieu poreux anisotrope sont les équations de continuité, la loi de Darcy généralisée et les équations d'énergie.

Pour le cas d'un milieu fluide, les conditions aux limites de non-glissement sur la paroi avec température de paroi uniforme et puits thermique uniformément distribué, sont considérées. Dans le cas du milieu poreux, la condition de non-glissement sur la paroi n'existe pas et nous considérons deux types de conditions limites thermiques: une température uniforme avec un puits thermique constant et une température non-uniforme sans puit thermique correspondant à une stratification.

3. APPROCHE MUMÉRIQUE (Chapitre 3)

Une approche numérique basée sur la méthode des différences finies est utilisée pour résoudre la convection d'amplitude finie. Toutes les dérivées spatiales sont discrétisées en utilisant un schéma centré de second ordre. Un maillage uniforme de 18×36 est utilisé pour discrétiser l'espace cylindrique. Les équations d'énergie et de transport de vorticité sont résolues par la méthode implicite aux directions alternées (A.D.I.). L'équation de Poisson et l'équation de fonction de courant sont résolues par la méthode de surrelaxation (S.O.R.).

Dans le cas de la géométrie considérée dans cette étude (cylindre), une difficulté dans la résolution numérique provient de la singularité (non-physique) au centre

($r = 0$) pour des coordonnées cylindriques. Pour contourner la difficulté, un maillage cartésien est utilisé au centre du cylindre. L'application de cette technique dans le code numérique permet au centre d'être transparent au mouvement, quelle que soit la direction.

La direction implicite θ comporte une condition limite de périodicité pour chaque variable physique f et les matrices résultantes ne sont pas tridiagonales. Une solution directe consiste à utiliser le principe de partition, lequel a pour effet à ramener les matrices de départ à des forme tridiagonales.

La précision des calculs numériques et la validité du code numérique ont été vérifiées en comparant nos résultats avec certains résultats publiés dans la littérature. Une bonne accord est observé entre les résultats numériques, ceux obtenus par la méthode de perturbation et la méthode de stabilité linéaire pour les deux milieux, poreux et fluide.

4. CONVECTION MIXTE DANS UN CYLINDRE EN ROTATION LENTE (Chapitre 4)

On étudie la convection naturelle et mixte dans un cylindre en rotation rempli d'un milieu poreux isotrope / milieu fluide. Des conditions limites isothermes avec un puits thermique uniformément distribué sont appliquées. Seule la rotation lente est considérée, pour laquelle le champ de gravité terrestre est le seul présent. Les régimes d'écoulement résultant de la convection naturelle et de la rotation sont obtenus par une approche numérique et par la méthode de perturbation. Les résultats du programme numérique d'amplitude finie sont donnés en fonction des nombres de Rayleigh et de Péclet. Une méthode de perturbation est utilisée comme alternative pour des valeurs basses des nombres de Rayleigh et de Péclet. Ces deux méthodes servent pour les deux milieux: poreux isotrope et fluide. Pour le cas d'un milieu poreux isotrope, les résultats revèlent qu'une masse appréciable du fluide ne

participe pas à la rotation. Ce comportement donne lieu à un écoulement autour du centre c'est-à-dire que la valeur de la fonction de courant au centre devient différente de zéro. Cependant, pour des rotations relativement importantes, la masse fluide presque toute entière se comporte comme un solide en rotation et le transfert de chaleur est réduit à zéro. De la même façon, pour la cas d'un milieu fluide, un écoulement net, relativement à la paroi du cylindre (régime de cisaillement), suvient à très basse vitesse de rotation; à des vitesse angulaires plus grandes, une rotation solide du fluide se produit (régime de rotation solide) pour lequel le transfert du chaleur est réduit à celui de la conduction pure. La différence de comportement entre le milieu poreux saturé et le milieu fluide est la suivante: l'écoulement net, dans le cas du milieu fluide, subit une chute drastique à nombre de Rayleigh elevé. Cette chute s'accompagne d'un mouvement non permanent oscillant, vraisemblablement causé par l'inertie. Pour le milieu poreux saturé, la transition vers le régime de rotation solide avec diminution de l'écoulement net vers zéro se fait de façon graduelle quel que soit le nombre de Rayleigh et sans qu'il y ait de comportement oscillatoire. Ce genre de comportement qui avait déjà été décrit pour le cas d'un espace annulaire est observé pour la première fois dans le cas d'un cylindre circulaire et la relation théorique entre l'écoulement net et le nombre de Péclet rotationnel est obtenue pour la première fois dans le cas du milieu poreux saturé. Le nombre de Nusselt, le cisaillement à la paroi et la fonction de courant au centre sont maintenant reliés quantitativement à la vitesse angulaire exprimée de façon adimensionnelle par le nombre de Péclet. Dans le cas d'une rotation qui s'amorce, la valeur de la fonction de courant au centre a été établie en partie de façon analytique et en partie de façon numérique et exprimée en fonction du nombre de Rayleigh; cette fonction de courant au centre définit la masse de fluide liée à la gravité terrestre.

5. CONVECTION NATURELLE DANS UN CYLINDRE EN ROTATION RAPIDE (Chapitre 5)

On considère dans ce chapitre la convection de Bénard à des grandes vitesse de rotation pour des parois isothermes et pour un puits de chaleur uniformément réparti dans le domaine. La cavité contient un milieu poreux isotrope ou anisotrope. Quand la vitesse de rotation est très élevée, la gravité radiale devien très grande et l'on suppose que la gravité terrestre est régligeable. En régime de conduction pure, la direction du gradient de masse volumique est vers l'intérieur du cylindre et celui de la gravité radiale vers l'éxtéreur. L'équilibre est donc potentiellement instable et la convection naturelle peut se déclencher au-dessus d'une certaine valeur de Rayleigh (nombre de Rayleigh critique). Pour le cas d'un milieu isotrope, l'analyse de la stabilité linéaire permet de prédire le nombre de Rayleigh critique caractérisant le début de la convection. Les résultats obtenus avec la méthode analytique de stabilité linéaire sont confrontés à ceux obtenus numériquement. De plus, la consistance des résultats obtenus avec le programme numérique d'amplitude finie avec les résultats prédits par l'analyse de la stabilité est vérifiée. Les resultats montrent qu'il existe un nombre de Rayleigh critique $Ra_c = 384$ au-dessus duquel la convection naturelle peut se déclencher et des solutions multiples se produire pour des valeurs de Rayleigh supérieures à la valeur critique. Le début de la convection est caractérisé par quatre cellules de convection mais à des nombres de Rayleigh importants, la structure de l'écoulement est composée de plusieur cellules. L'anisotropie de la perméabilité affecte la valeur critique du nombre de Raylrigh. Les résultats ont montré que la valeur critique, dans le cas d'une perméabilité anisotrope, peut être inférieure à celle prédite pour un milieu isotrope. De plus, pour un milieu poreux anisotrope ayant un rapport de perméabilité trés élevé, les résultats montrent que la structure de l'écoulement juste au-dessus du seuil critique pent être composée de 6 cellules au lieu de 4 comme dans le cas isotrope. Pour le cas anisotrope, les racines doubles définissant les seuils des différentes configurations d'écoulement deviennent distinctes. Enfin, les résultats montrent que la configuration de l'écoulement prend une position angulaire bien déterminée par rapport aux axes principaux. Ce

comportement est différent du cas isotrope pour lequel la position angulaire de la configuration peut être quelconque.

6. CONVECTION NATURELLE DANS UN CYLINDRE SANS ROTATION (Chapitre 6)

L'instabilité de Bénard est étudiée pour un cylindre fixe, non-poreux isotrope / anisotrope dont la distribution de la température est sinusoïdale sur la frontière, en présence du champ gravitationnel terrestre. Une telle distribution de température est équivalente à une stratification thermique linéaire de l'environnement dans une direction donnée. Un cas particulier est celui où la température maximum se trouve au bas ($\theta_0 = 0$, chauffage par le bas). La stratification thermique imposée sur la frontière circulaire est alors dans la direction verticale et par conséquent la direction du gradient de masse volumique est opposée à la gravité terrestre en tout point du domaine, donnant lieu à un équilibre des forces potentiellement instable en conduction pure. Pour le milieu poreux isotrope avec chauffage par le bas, la valeur critique du nombre de Rayleigh pour lequel un mouvement convectif apparaît est approximativement 23.3. A cette valeur, deux types de configurations d'écoulement sont possibles: une configuration contenant deux cellules convectives, symmétriques relativement à un diamètre vertical, et une configuration centro-symmetrique contenant trois cellules. De plus, les résultats numériques pour des convections d'amplitude finie à $\theta_0 = 0$ démontrent que les configurations à deux et à trois cellules sont stables pour une plage donnée de Ra. Des solutions numériques ont aussi été obtenues à divers nombres de Rayleigh pour une position arbitraire de la température maximum sur la frontière. L'écoulement est alors unicellulaire à moins que les températures maxima se situent au voisinage de la position instable ($\theta_0 = 0$). Les résultats de l'analyse de stabilité sont consistants avec la simulation numérique. Pour le cas anisotrope, les resultats sont limités au cas du chauffage par le bas. Le rapport de permeabilité R et l'angle des axes principaux θ_k exercent une forte influence sur les

valeurs critiques du nombre de Rayleigh. Le valeur du nombre de Rayleigh critique est obtenue quand l'axe principal correspondant à la perméabilité maximum est vertical ($R < 1, \theta_k = \pi/2$). Ainsi, selon l'analyse de stabilité, le nombre de Rayleigh critique correspondant à $R = 0.125, \theta_k = 90$ est environ 20, une valeur inférieure au seuil du cas isotrope. La forme de l'écoulement initial prédit par l'analyse de stabilité comporte soit deux, soit trois cellules de convection, selon la valeur de θ_k. A la différence du milieu poreux isotrope, le nombre de Rayleigh critique Ra_c n'a pas une valeur fixe mais est fonction de θ_k et de R.

7. CONCLUSIONS ET PERSPECTIVES (Chapitre 7)

Dans le cadre du présent travail quelques cas types de convection dans un cylindre circulaire d'importance fondamentale et pratique ont été étudiés. Pour le cas d'un cylindre avec rotation lente, l'interaction entre la convection naturelle et la rotation a été déterminée analytiquement de sorte que le lien entre la rotation et l'écoulement net autour du centre est établie sur une base théorique solide et l'effet de la rotation sur le transfert de chaleur est expliqué. Dans le cas d'un milieu poreux saturé anisotrope nous avons démontré que la valeur du nombre de Rayleigh critique est modifiée; nous avons aussi déterminé que les configurations d'écoulement en situation de gravité radiale s'orientent par rapport aux axes principaux de façon à produire des configurations d'écoulement symétriques.

TABLE OF CONTENTS

Chapter 5

Chapter 6

LIST OF TABLES

LIST OF FIGURES

LIST OF SYMBOLS

$\mathbf{g}'$	gravitational acceleration vector, m/s^2
$\hat{\mathbf{g}}$	unit vector along gravity
K	permeability of the porous medium, m^2
K_1, K_2	extremum permeabilities of the porous medium, m^2
k	thermal conductivity of the fluid or saturated porous medium, $W/(m \cdot K)$
Nu	overall Nusselt number
Pe	rotational Peclet number for fluid: $\Omega' r_0'^2/\alpha$
Pe^*	rotational Peclet number for saturated porous medium: $\sigma\Omega' r_0'^2/\alpha$
Pr	Prandtl number, ν/α
p'	pressure, N/m^2
R	permeability ratio: K_2/K_1
Ra	Rayleigh number based on gravity fluid: $g'\beta\Delta T' r_0'^3/\nu\alpha$ porous: $g'\beta\Delta T' r_0'\sqrt{K_1 K_2}/\nu\alpha$
Ra_Ω	Rayleigh number based on centrifugal force fluid: $\beta\Delta T' r_0'^4 \Omega'^2/\nu\alpha$ porous: $\beta\Delta T' r_0'^2\sqrt{K_1 K_2}\Omega'^2/\nu\alpha$
Re	rotational Reynolds number fluid: $\Omega' r_0'^2/\nu$ porous: $\sigma\Omega' r_0'^2/\nu$
$\hat{\mathbf{r}}$	unit vector in radial direction
r	dimensionless radial coordinate
r_0'	diameter of cylinder, m
S'	uniform heat sink by unit volume, W/m^3

T'	temperature, K
t	dimensionless time
$\Delta T'$	temperature scale
$\mathbf{V}$	dimensionless velocity vector
u, v	dimensionless velocity components in the radial and azimuthal directions respectively
$\mathbf{X}$	origin of cylindrical coordinate system $(r,\ \theta)$
$\hat{\mathbf{z}}$	unit vector normal to $(r,\ \theta)$ plane

Greek Symbols

α	thermal diffusivity fluid: m^2/s porous: $k/(\rho c)_f, m^2/s$
β	thermal expansion coefficient, K^{-1}
Γ	hydrodynamic circulation, $\oint \mathbf{V} \cdot \mathbf{dl}$
ϵ	porosity
$\mathbf{\Theta}$	dimensionless vector defining the discretized temperature field
$\hat{\theta}$	unit vector in θ direction
θ	angular coordinate
θ_0	heating phase angle
θ_k	angular position of the principal axis corresponding to K_2
λ	eigen value
μ	dynamic viscosity of fluid, $kg/(s \cdot m)$
ν	kinematic viscosity of fluid, m^2/s
ρ'	fluid density, kg/m^3

$(\rho c)_f$	heat capacity of the fluid, $J/(m^3K)$
$(\rho c)_p$	heat capacity of the saturated porous medium, $J/(m^3K)$
$(\rho c)_s$	heat capacity of the solid, $J/(m^3K)$
σ	heat capacity ratio, $(\rho c)_p/(\rho c)_f$
τ	dimensionless torque
ϕ	angle between gravity vector $\mathbf{g}'(t)$ and position vector $\mathbf{r}'$
$\mathbf{\Psi}$	dimensionless vector defining the discretized stream function field
ψ	dimensionless stream function
Ω'	angular velocity, s^{-1}
ω	dimensionless vorticity
∇	gradient operator
$\nabla\cdot$	divergence operator
∇^2	Laplacian operator

Superscripts

$'$	refers to dimensional variables
$\bar{}$	refers to non-rotating coordinate system $(\bar{r},\ \bar{\theta})$
$\hat{}$	refers to unit vector
$\tilde{}$	refers to perturbated values

Subscripts

av	refers to values averaged over the domain
c	refers to values at the geometric center of cylinder

ext	refers to extreme values
w	refers to values on the boundary of cylinder

LIST OF APPENDICES

Chapter 1

INTRODUCTION

1.1 BACKGROUND

Natural and mixed convective heat transfer within a cylinder boundary has been the subject of a great deal of investigations so far because of its considerable importance both from fundamental and practical points of view. Numerous researches reported cover such fields as applied mathematics, basic physics, geophysics [1], fluid mechanics as well as technological applications ranging from crystals growth [2], food industries [3, 4, 5, 6], electronic cooling systems [7, 8, 9], chemical engineering process [10, 11], rotating machinery [12], heating, ventilating and air conditioning engineering of buildings [13, 14, 15], and shifting to the prediction of meteorological conditions. Moreover, some of the observed flows resemble those in model problems in astrophysical/planetary fluid dynamics [16, 17, 18]. In particular, the use of magnetic field has been proposed as a means of reducing the natural convection in the process of crystal growth. It will be evidenced in this study that the effect of anisotropy is analogous, under certain circumstances where the Maxwell and momentum equations are uncoupled, to the effect of a magnetic field on the flow behavior.

It is well known that a density gradient not parallel to a body force field will produce motion no matter how small the gradient may be, since the pressure cannot balance the variations in the body force so produced. The most common examples occur in fluids placed in a gravitational field which are heated differentially in the horizontal direction. If the system to be studied undergoes rotation, however, the centrifugal acceleration may play a role analogous to that of gravity in producing

motion.

In this study the convection driven by gravitational force in an anisotropic porous / isotropic porous / fluid horizontal cylinder rotating about its axis is numerically and analytically examined. The investigation also covers the Bénard instability in an anisotropic / isotropic porous cylinder with fast rotation and without rotation where the direction of density gradient is opposite to that of the body force field. The geometry of the problem is illustrated in Fig. 1.1. It is obvious that convection in an anisotropic porous medium cylinder becomes more complicated because of varying permeability with respect to the orientation.

Since the particular studies involved in this work preclude any symmetry with respect to the vertical diameter the whole cylinder is considered as flow domain. This is in contrast to most previous studies where a symmetry with respect to the vertical diameter was taken into account. In particular, if finite difference techniques are used in cylindrical coordinates the center represents an artificial or mathematical singularity which must be handled properly so that the center region becomes transparent to flow in all directions. Despite of the varying boundary conditions imposed and fluid media considered in this study, a common cylindrical geometry holds the following cases together, namely, mixed convection in a low rotation isotropic porous / fluid cylinder, natural convection in a fast rotation isotropic / anisotropic porous cylinder and natural convection in a non-rotating isotropic / anisotropic porous cylinder subject to a sinusoidal temperature distribution on its boundary. The background about each part is stated separately in this chapter.

1.1.1 Mixed Convection in a Low Rotation Cylinder

Since natural convection in rotating systems is involved in numerous industrial processes as a means of transporting thermal energy, it has received increased attention in recent years. The rotation about a vertical axis has been intensively

studied [19, 20, 21, 16, 22] because this kind of configuration is frequently encountered in engineering problems. Comparatively little work has been done on rotation about an horizontal axis in which natural convection is combined with rotation. Some early experimental investigations of heat transfer between horizontal concentric rotating cylinders were reported [23, 24, 25] in which heat transfer rates were measured over a wide range of Reynolds (Taylor) numbers. None of them concerned the effects of the Rayleigh number on the flow motion and heat transfer, and the data reported are for cases where the densimetric Froude number (which expresses the relative magnitude of buoyancy versus rotation effects) $\gg 1$.

Free convection between two horizontal isothermal cylinders, with the stationary outer cylinder and the inner cylinder rotating about its axis at constant angular velocity, was considered by Lee [26] and Fusegi et al. [27]. The analysis was restricted in both cases to the cross-sectional plane and did not allow for the three-dimensional effects. Lee has studied the combined effects of natural convection and rotation for a fluid contained between eccentric cylinders at different temperatures and focused mainly on the results obtained for the low Froude numbers. Whereas Fusegi et al. did not consider the eccentric case but treated the problem for both high and low value of Froude number.

Yang et al. [2] investigated the natural convection of fluids inside a single horizontal rotating cylinder with both ends maintained at different temperatures, that is, with an applied axial temperature gradient. For that case the pure conduction heat transfer is present in the horizontal direction and three-dimensional flows were obtained numerically allowing for both axial rotation and normal gravity. Rotation was observed to inhibit natural convection and endwall heat transfer. They formulated the problem in both inertial and non-inertial frames and found a steady-state flow regime in the inertial frame. According to their results, free convection affects the heat transfer only at low rotational speeds and increasing the rotational speed

develops almost a rigid body motion for which the heat transfer reduces to their pure conduction level.

Robillard and Torrance [28] recently investigated the effects of rotation on an annular saturated porous layer. A net circulating flow around the annulus relative to the solid matrix was detected and the convective heat transfer was found to decrease monotonically to zero with increasing rotation speed. Subsequently, Ladeinde and Torrance [29] treated the case of a rotating fluid-filled horizontal cylinder with constant volumetric heating and fixed wall temperature for which the heat transfer and convective motion involve radial and azimuthal directions exclusively by using a finite element solution procedure. Their investigation covers a wide range of rotation speeds. A second Rayleigh number based on radial acceleration in addition to the usual gravity-based Rayleigh number was introduced. It was found that when radial acceleration dominates over gravity (strong rotation), steady-state flows are obtained in the rotating coordinate system. There is a critical Rayleigh number needed to establish the initial two-cell state and the subsequent flow patterns are multicellular. For weak rotation, the flow is bicellular and steady in the inertial coordinate system. When radial acceleration and gravity are comparable, complex time-dependent solutions result in both systems and the largest flow and heat transfer rates are found. For both weak and strong rotation, there is also an optimum Reynolds number based on the rotation speed that gives the maximum effect of gravity. It was once again confirmed that for weak rotation, if the Reynolds number becomes larger than the optimum value, the flow field approaches solid-body rotation in the inertial frame and the temperature field approaches the pure conduction state.

More recently, Prud'homme et al. [30] studied natural convection in an annular fluid layer confined between two horizontal cylindrical boundaries rotating at the same angular velocity. The weak rotation regime only is considered for which

centrifugal force is neglected. The results indicate that when the angular velocity is small a significant mass of fluid far from the boundaries remains tied up to the gravity vector at first and thus, does not take part in the solid-body rotation. This creates a net circulating flow around the annulus in the rotating system, the intensity of which is shown analytically to be proportional to Ra^2Re for incipient convection. At high Rayleigh numbers, a bifurcation exists between the circulating and solid-body rotation flow regimes, in contrast with the smooth transition observed at lower Rayleigh numbers. Hysteresis effects are observed over a certain range of Reynolds numbers, provided that the Rayleigh number is high enough.

In this study the behavior of natural and mixed convection in a low rotation horizontal cylinder filled with an isotropic porous / fluid medium with isothermal boundary condition and an uniformly distributed heat sink is investigated. As described by Vasseur and Robillard [31], this kind of problem is equivalent to the case without heat sink or source and with boundary temperature increasing at a steady rate with time. Weak rotation regimes only are considered. The flow in the cylinder is assumed to be two-dimensional in a vertical, (r, θ) plane. It is expected to examine closely the interaction between rotation about a horizontal axis and the gravity force. Even though the fluid and porous media are described by different momentum equations and have different thermal and dynamic properties (eg., for the fluid medium, the resistance to motion originates from the solid boundary whereas that for a porous medium takes place everywhere of whole matrix), they still have the same dimensionless energy equations and are confined within the same geometry. Therefore, a qualitatively similar behavior under same conditions are expected. The interaction between convective rolls resulting from classical Bénard instability and the effects of rotation speed are studied numerically. For the finite amplitude convection, the numerical results based on finite difference scheme cover a broad range of Rayleigh number and Peclet number. In addtion, a regular perturbation method

is adopted to study the incipient convection and validate the numerical approach. Results from both approaches coincide. For the isotropic porous medium case, both approaches reveal that a large part of the saturated fluid does not participate to rotation at low rotation speed. Thus the stream function at the center as expressed in a rotating coordinate system may differ largely from zero. However, with increasing angular velocity, the fluid is gradually entrained and a solid body rotation regime develops for which the convective heat transfer is eventually reduced to zero. Similarly, for fluid medium case, a net flow relative to cylinder boundary is found at low rotation speed (shear flow regime) and a solid body rotation occur at high angular velocities (solid body rotation regime) in which the rotational effects on convection are found to reduce the heat transfer towards the pure conduction level.

1.1.2 Natural Convection in a Fast Rotation Cylinder

Regarding the low rotation cylinder, most of studies concentrated on the mixed convection confined within a low rotation cylinder in which the gravity force and centrifugal force are comparable.

Some of previous works treated the centrifugally driven convection in a fast rotating fluid-filled cylinder in which the gravity is considered negligible. Homsy and Hudson [32] studied natural convection in a cylinder of fluid rotating about a vertical axis and heated from above. Their work contains information about the asymptotic tendency reached at high rotation speed where the centrifugal force becomes predominant. Solutions were found to depend mainly upon the thermal conditions assumed at the side walls and the heat transfer was considerably augmented by rotation. Ladeinde and Torrance [29] studied the case of a rotating fluid-filled horizontal cylinder with constant volumetric heating and fixed wall temperature. The limiting case that heat transfer and convective motion induced exclusively by the radial acceleration is of interest to their studies. As mentioned before, a second Rayleigh

number based on radial acceleration in addition to the usual gravity-based Rayleigh number was introduced. It was found that when radial acceleration dominates over gravity (strong rotation), steady-state flows are obtained in the rotating coordinate system. There is a critical Rayleigh number above which a two-cell state is initiated. At higher Rayleigh number, subsequent flow patterns may be multicellular.

In the context of fast rotation the present study is limited to the isotropic / anisotropic porous layer. The saturated porous medium is confined in a cylinder subject to a centrifugal force field exclusively. An isothermal condition is imposed on the circular boundary and a heat sink is uniformly distributed within whole region considered. With this condition, the direction of density gradient of the fluid is toward the geometric center of cylinder and the centrifugal force is acting on the fluid in the opposite direction. This configuration is potentially unstable and motion occurs when the Rayleigh number based on the centrifugal force is beyond a critical value, which is obtained analytically and numerically in this study. It is predicted that multiple stable solutions differing by their number of cells exist at Rayleigh numbers well above the critical value.

1.1.3 Natural Convection in a Non-Rotating Cylinder

The study of Bénard instability in enclosed spaces (under the influence of terrestrial gravity) can be traced back to about one century ago. In 1900, Bénard [33] noted that a fluid contained between infinite horizontal plates would break up into small convective cells if the lower plane were at a temperature sufficiently higher than the upper one. Bénard reasoned that the viscous forces present at the boundary planes would prevent the onset of motion unless the density gradient was steep enough. The convective instability in enclosed spaces has been a subject of many theoretical and experimental investigations for many years. Most of the past works dealt with rectangular cavities.

There exists though some literature on convective heat transfer problems within a flow domain of circular shape. Quack [34] has solved the problem of natural convection in a horizontal cylinder filled with a fluid and cooled at a constant rate. The same problem was also considered experimentally by Deaver and Eckert [35] and numerically by Takeuchi and Cheng [36]. The numerical study took advantage of the symmetry with respect to the vertical diameter that was found in the experimental results of Deaver and Eckert [35]. The parallel problem of a fluid-saturated porous medium bounded by an infinitely long horizontal cylinder was treated analytically by Nguyen and Nguyen [37] and solutions obtained were found to agree closely with finite difference results even at very high values of the Rayleigh number.

The Bénard instability in a fluid-filled cylinder was considered analytically by Weinbaum [38]. A temperature distribution of the form $T_w = \cos(\theta - \theta_0)$, where θ_0 is the heating phase angle, was imposed on the boundary. This is equivalent to place the circular enclosure in thermally stratified surroundings. There is a particular value of θ_0 for which the temperature gradient is upward (bottom heating) and the system becomes potentially unstable. Weinbaum established the onset of motion at a critical Rayleigh of 576. A single cell flow pattern was found for all conditions.

Moreover, early works on convective heat transfer through porous medium mainly focused on homogeneous isotropic porous medium and relatively few studies were devoted to anisotropic medium, although the latter are sometimes encountered in industrial and geological processes. In addition, most of previous studies on anisotropic media were confined to such geometries as rectangular cavities or horizontal layers, among which are the articles of Burns and Tien [39], Nilsen and Storeslatten [40], Tyvand and Storesletten [41] and Zhang [42]. It has been found that the anisotropy in permeability and the inclination of the principal axes influence the flow patterns and the heat transfer rates significantly.

In this study, the behavior of a Darcy isotropic/anisotropic porous medium within a horizontal cylinder having a sinusoidally distributed temperature on the boundary with bottom heating is investigated analytically and numerically. The anisotropy involved concerns exclusively the permeability. The boundary is subject to a thermal stratification in the vertical direction. Since the pure conduction temperature gradient is in the upward direction, motionless equilibrium is possible in this circumstance. However this configuration is potentially unstable and motion will occur when the Darcy Rayleigh number Ra is beyond a critical value. A linear stability analysis is performed to investigate the criterion and possible flow patterns for the onset of convection. It is found that the flow pattern at the onset of convection is either a 2-cell or a 3-cell structure, depending on the inclination of the principal axes of the porous matrix and anisotropy ratio R for the anisotropic case, and on the initial flow configuration for isotropic case. It is shown that both the permeability ratio and inclination of the principal axes have a strong influence on the critical value of Ra and the flow pattern at the onset of convection. Additional results are obtained for finite amplitude convection, from a numerical approach. A numerical code is developed to study the finite amplitude convection beyond the critical Ralyeigh number. Results are analyzed in terms of the ratio of permeability and the orientation angle of the principal axes.

1.2 OUTLINE OF THE THESIS

In the present study the steady state natural and mixed convection in a horizontal cylinder is examined in more detail by means of numerical and analytical methods. There is a lot of possible combinations in boundary conditions, nature of the fluid medium, forces exerted on it and motion state of cylinder to be investigated. it is clearly not possible to analyze each one in detail within the limits of the present study. Instead, the present study is focussed on some typical cases described below. It is nevertheless useful to classify the various configurations according to the

motion state of cylinder, namely, low rotation, fast rotation and non-rotating. Consistently, the work corresponding to different motion states of cylinder are presented in Chapters 4, 5 and 6 respectively.

Chapter 2 presents mathematical models based on the governing equations with appropriate boundary conditions, which expresses mass, momentum and energy conservation in the fluid and porous medium layer, respectively. Chapter 3 contains the numerical scheme used to solve the governing equations given in Chapter 2.

In Chapter 4 the problem of mixed convection in a low rotation isotropic porous/fluid cylinder with isothermal boundary condition and an uniform distributed heat sink is considered. It is expected to observe the effects of rotation on natural convection in a horizontal cylinder.

Bénard convection in a fast rotation isotropic / anisotropic porous cylinder with an isothermal condition on the boundary and a uniformly distributed heat sink is studied in Chapter 5. In the situation of fast rotation, only centrifugal force is involved, the terrestrial gravity being assumed negligible. Under those conditions the direction of the pure conduction density gradient is toward the geometric center of cylinder while the centrifugal force field is acting on fluid in the opposite direction. This configuration is potentially unstable and Bénard cells are expected to occur beyond a critical Rayleigh number. The effects of anisotropy in permeability and orientation of the principal axis on fluid motion and heat transfer are going to be researched.

Finally the Bénard instabilities in a non-rotating isotropic / anisotropic porous cylinder having a sinusoidally distributed temperature on the boundary is investigated in Chapter 6. A particular case is studied for which the maximum temperature was at the bottom (bottom heating). Such a boundary condition is equivalent to a thermal stratification imposed to the circular boundary in the vertical direction in

which case the direction of density gradient is opposite to terrestrial gravity.

The conclusions and recommendations are outlined in Chapter 7. The reference literature, symbols used in this work are attached to the thesis. Furthermore, Appendices A, B, C and D give more details about Boussinesq approximation and the mixed convection, governing equations in non-rotating coordinate system, matrix partition procedure and coefficients in perturbation solution, respectively.

In summary, the main objective of this thesis is to study the behavior of fluid motion and heat transfer in a horizontal cylinder and to observe the effects of relative strength of natural convection and rotation on the characteristics of thermal transport of the cylinder.

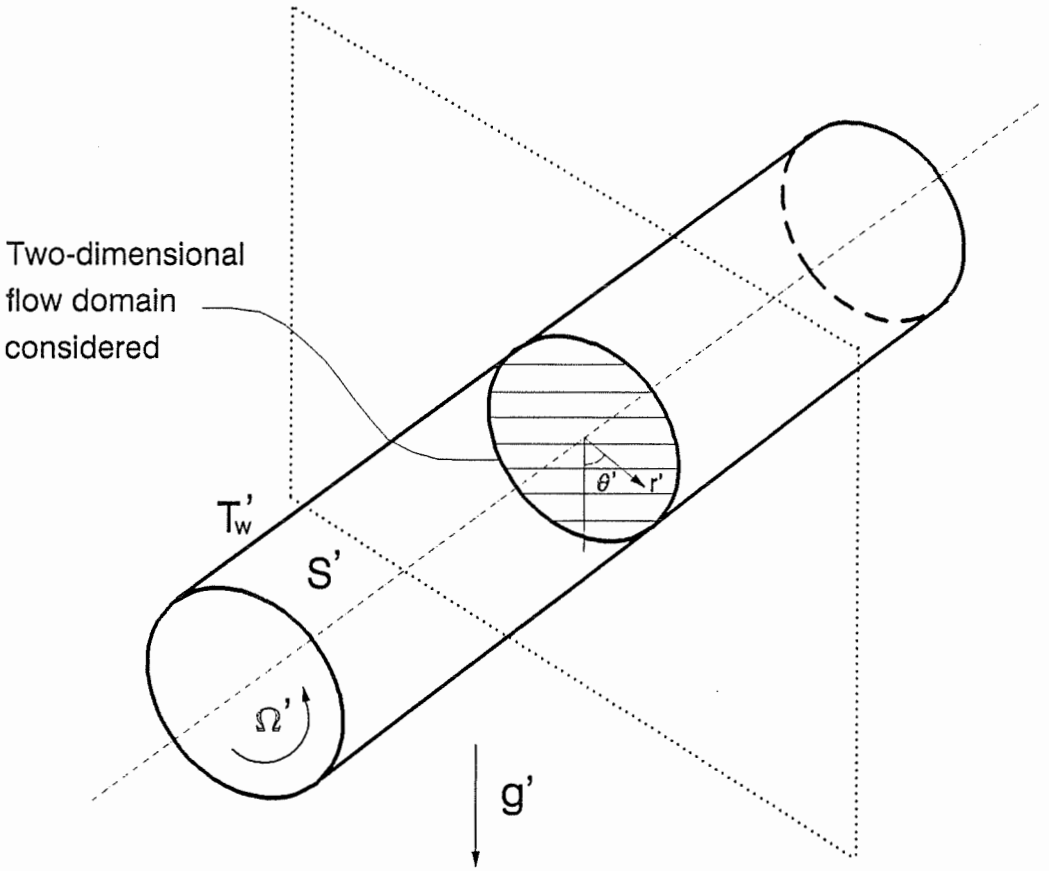

Figure 1.1: Rotating cylinder filled with a fluid or a fluid saturated porous medium

Chapter 2

MATHEMATICAL MODEL

The geometry considered is a circular cylinder with an horizontal axis and theoretically infinite length. In most practical cases the extent of the cylinder is so large that the three-dimensional effects are assumed to takes place in a small zone of cylinder near the ends. Concerning the potential three dimensional effects, the reader is referred to the study of Caltagirone [43] in which the annular geometry was considered and three dimensional effects were expected to occur at Rayleigh numbers somewhere between 100 and 200, these three dimensional effects originating from the upper unstable layer between the two boundaries. In the present study, no such layer exists and the flow is reasonably assumed to be two-dimensional in the (r', θ') plane of Fig. 1.1. The governing equations for the present problem may be expressed in either a rotating or a non-rotating coordinate system. In this text the rotating coordinate system refers to one fixed with respect to rotating boundary (fluid medium) or to rotating boundary and porous matrix (saturated porous medium), and non-rotating coordinate system refers to one fixed with respect to the ground. In the rotating coordinate system, the force fields involved are terrestrial gravity and radial gravity (centrifugal force field), and then natural convection takes place. In the non-rotating coordinate system, the force field is terrestrial gravity only and mixed convection occurs. These two coordinate systems are shown in Fig. 2.1 *a* and *b* (also in Fig. 2.2 *a* and *b*), respectively. A set of equations based on either coordinate system may be used with equal success in the numerical approach. At low rotation rates, one set leads to a time-dependent solution whereas the other one provides steady state solutions. Results from both approaches are identical when properly transformed.

Although the momentum equations for fluid and saturated porous media are given with the two force fields (terrestrial gravity and radial gravity) together, the present study will not treat cases where both force fields are involved simultaneously, but the investigation will be limited to asymptotic cases for which one or the other can be neglected. The reason is that those asymptotic cases need to be thoroughly understood before attempting to investigate intermediate cases. Also those intermediate cases are time dependent whereas the asymptotic ones are steady.

2.1 GOVERNING EQUATIONS FOR FLUID-FILLED CYLINDER

2.1.1 Rotating Coordinate System

The problem is better approached numerically in the rotating coordinate system rotating along with the cylinder shown in Fig. 2.1*a*. Consider a coordinate system (r', θ') attached to a horizontal cylinder rotating at a steady angular velocity Ω'. A positive value of Ω' corresponds to a counterclockwise rotation of the cylinder. For the geometry of Fig. 2.1*a*, the gravity vector $\mathbf{g}'(t)$, when viewed from the coordinate frame (r', θ'), moves clockwise at a same angular speed Ω'. The analysis is carried out in terms of relative flow field $\mathbf{V}'$ induced by the sole natural convection effects, that is, what would appear to an observer fixed with respect to the rotating boundary.

The Navier-Stokes equation in the rotating coordinate system for a fluid of constant thermal properties [44, 45] are

$$\rho' \frac{D\mathbf{V}'}{Dt'} = -\nabla p' + \rho' \{\mathbf{g}'(t) - \mathbf{\Omega}' \times (\mathbf{\Omega}' \times \mathbf{r}') - 2\mathbf{\Omega}' \times \mathbf{V}'\} + \mu \nabla^2 \mathbf{V}' \qquad (2.1)$$

In this equation, the third and fourth terms on the right-hand side represent the centrifugal force and Coriolis force, respectively, and the Laplacian operator can be

written as

$$\nabla^2 f = \frac{1}{r}\frac{\partial}{\partial r}(r\frac{\partial f}{\partial r}) + \frac{1}{r^2}\frac{\partial^2 f}{\partial \theta^2} \tag{2.2}$$

Defining ρ' in terms of the temperature difference $\rho' = \rho'_0 - \rho'_0\beta(T' - T'_0)$, the pressure gradient may be split as follows [29]

$$\nabla p' = \nabla p'_d + \rho'_0\{\mathbf{g}'(t) - \mathbf{\Omega}' \times (\mathbf{\Omega}' \times \mathbf{r}') - 2\mathbf{\Omega}' \times \mathbf{V}'\} \tag{2.3}$$

since $2\rho'_0(\mathbf{\Omega}' \times \mathbf{V}')$ is conservative. The first part of right hand side in above equation is the dynamic pressure and second one the hydrostatic pressure field based on ρ'_0. Replacing in Eq. (2.1) the pressure by its expression above, the momentum equation becomes

$$\{\rho'_0 - \rho'_0\beta(T' - T'_0)\}\frac{D\mathbf{V}'}{Dt'} = -\nabla p'_d - \rho'_0\beta(T' - T'_0)\{\mathbf{g}'(t) - \mathbf{\Omega}' \times (\mathbf{\Omega}' \times \mathbf{r}')$$

$$-2\mathbf{\Omega}' \times \mathbf{V}'\} + \mu\nabla^2\mathbf{V}' \tag{2.4}$$

Now the Boussinesq approximation ($\Delta\rho' \ll \rho'$) is going to be applied. The following steps will show why the density difference can be neglected everywhere in Eq. (2.4), except in the source term based on terrestrial and radial gravity, when free convection is being considered. It has to be kept in mind, though, that this might not be the case for mixed convection problems. Since $|\rho'_0\beta(T' - T'_0)| \ll \rho'_0$, there exists $|\beta(T' - T'_0)| \sim \epsilon$, ϵ being in this context a small quantity ($\epsilon \ll 1$). Dividing (2.4) by ρ'_0 gives

$$(1-\epsilon)\frac{D\mathbf{V}'}{Dt'} = -\frac{\nabla p'_d}{\rho'_0} - \epsilon\{\mathbf{g}'(t) - \mathbf{\Omega} \times (\mathbf{\Omega}' \times \mathbf{r}') - 2\mathbf{\Omega}' \times \mathbf{V}'\} + \nu\nabla^2\mathbf{V}' \tag{2.5}$$

$\mathbf{V}'$ being caused exclusively by the difference in density of fluid, is also of the order ϵ. Equation (2.5) may be rearranged as

$$(1-\epsilon)\frac{D\epsilon'}{Dt'} = -\frac{\nabla p'_d}{\rho'_0} - \epsilon\{\mathbf{g}'(t) - \mathbf{\Omega}' \times (\mathbf{\Omega}' \times \mathbf{r}') - 2\mathbf{\Omega}' \times \epsilon'\} + \nu\nabla^2\epsilon' \tag{2.6}$$

and therefore the order of magnitude analysis of (2.6) gives

$$\epsilon - \epsilon^2 \sim \epsilon - \epsilon\{\mathbf{g}'(t) - \mathbf{\Omega}' \times (\mathbf{\Omega}' \times \mathbf{r}')\} + \epsilon^2 + \epsilon \tag{2.7}$$

Neglecting the terms with the order of ϵ^2 in (2.7), the continuity, momentum and energy equations in the rotating frame for a fluid of constant thermal properties are written as

$$\nabla \cdot \mathbf{V}' = 0 \tag{2.8}$$

$$\frac{D\mathbf{V}'}{Dt'} = -\frac{\nabla p'_d}{\rho'_0} + \nu\nabla^2\mathbf{V}' - \beta(T' - T'_0)\{\mathbf{g}'(t) - \mathbf{\Omega}' \times (\mathbf{\Omega}' \times \mathbf{r}')\} \tag{2.9}$$

$$\frac{DT'}{Dt'} = \alpha\nabla^2 T' - S' \tag{2.10}$$

where S' is a sink term (negative heat source).

Introducing the following dimensionless variables

$r = r'/r'_0$

$t = t'\alpha/r'^2_0$

$(u, v) = (u', v')r'_0/\alpha$

$\Omega = \Omega' r'^2_0/\alpha$

$p = p'_d\, r'^2_0/\rho'_0\alpha^2$

$T = (T' - T'_0)/\Delta T'$

$\Delta T' = S' r'^2_0/k$

The problem can be cast in dimensionless form as

Continuity Equation

$$\nabla \cdot \mathbf{V} = 0 \tag{2.11}$$

Momentum Equation

$$\frac{D\mathbf{V}}{Dt} = -\nabla p + Pr\nabla^2\mathbf{V} - PrT\{Ra\hat{\mathbf{g}}(t) + Ra_\Omega\, r\hat{\mathbf{r}}\} \tag{2.12}$$

Energy Equation

$$\frac{DT}{Dt} = \nabla^2 T - 1 \tag{2.13}$$

The non-dimensional groups appearing in the Eq. (2.12) are the gravitational force-based Rayleigh number $Ra = g'\beta\Delta T' r_0'^3/\nu\alpha$, the centrifugal force-based Rayleigh number $Ra_\Omega = \beta\Delta T' r_0'^4\Omega'^2/\nu\alpha$, and the Prandtl number $Pr = \nu/\alpha$. $\hat{\mathbf{g}}(t) = \hat{\mathbf{r}}\cos\phi(t) - \hat{\theta}\sin\phi(t)$ is the unit vector in terrestrial gravity direction, $\hat{\mathbf{r}}$ and $\hat{\theta}$ are unit vectors in radial and azimuthal directions, respectively. $\phi(t)$ is the angle between unit vector $\hat{\mathbf{g}}(t)$ and $\hat{\mathbf{r}}$, which may be expressed as

$$\phi(t) = RePr\, t + \theta = Pe\, t + \theta \tag{2.14}$$

in which $Re = \Omega' r_0'^2/\nu$ is the rotational Reynolds number and $Pe = Re\, Pr$, the rotational Peclet number.

The pressure gradient can be eliminated by taking the curl of Eq. (2.12), which yields the vorticity-transport equation

$$\frac{D\omega}{Dt} = Pr\nabla^2\omega - Pr\nabla \times \{RaT\hat{\mathbf{g}}(t) + Ra_\Omega T\, r\hat{\mathbf{r}}\} \cdot \hat{\mathbf{z}} \tag{2.15}$$

with the dimensionless relative vorticity

$$\nabla \times \mathbf{V} = \omega = \frac{1}{r}\frac{\partial rv}{\partial r} - \frac{1}{r}\frac{\partial u}{\partial \theta} \tag{2.16}$$

and with the definition of the material derivative for a scalar in a cylindrical coordinate

$$\frac{Df}{Dt} = \frac{\partial f}{\partial t} + u\frac{\partial f}{\partial r} + \frac{v}{r}\frac{\partial f}{\partial \theta} = \frac{\partial f}{\partial t} + \frac{1}{r}\frac{\partial}{\partial r}(ruf) + \frac{1}{r}\frac{\partial}{\partial \theta}(vf)$$

The velocity components and vorticity itself may be expressed in terms of the relative stream function ψ as

$$u = \frac{1}{r}\frac{\partial \psi}{\partial \theta}, \qquad v = -\frac{\partial \psi}{\partial r} \tag{2.17}$$

$$\nabla^2 \psi = -\omega \tag{2.18}$$

Here equation (2.18) is a Poisson equation. Thus the continuity equation

$$\frac{1}{r}\frac{\partial ru}{\partial r} + \frac{1}{r}\frac{\partial v}{\partial \theta} = 0 \tag{2.19}$$

is automatically satisfied, and the final form of the vorticity-transport equation (2.15) is given below together with the energy equation

$$\frac{D\omega}{Dt} = Pr\nabla^2\omega + PrRa\{\frac{\partial T}{\partial r}\sin\phi + \frac{\cos\phi}{r}\frac{\partial T}{\partial \theta}\} + PrRa_\Omega\frac{\partial T}{\partial \theta} \tag{2.20}$$

$$\frac{\partial T}{\partial t} + u\frac{\partial T}{\partial r} + \frac{v}{r}\frac{\partial T}{\partial \theta} = \frac{1}{r}\frac{\partial}{\partial r}(r\frac{\partial T}{\partial r}) + \frac{1}{r^2}\frac{\partial^2 T}{\partial \theta^2} - 1 \tag{2.21}$$

For low rotational speeds, periodic solutions can be obtained in which the flow and temperature fields rotate at the angular velocity of the gravity vector.

2.1.2 Non-Rotating Coordinate System

An alternative set of equations may be obtained in a coordinate system ($\bar{r}$, $\bar{\theta}$) attached to the ground as shown in Fig. 2.1*b*. Relative velocities, vorticity and

stream function in the non-inertial frame are simply related to their inertial counterparts by

$$\begin{cases} \bar{r} = r \\ \bar{\theta} = \theta + Pe\,t \\ \bar{p} = p \\ \bar{T} = T \\ \dfrac{\partial}{\partial \bar{r}} = \dfrac{\partial}{\partial r} \\ \dfrac{\partial}{\partial \bar{\theta}} = \dfrac{\partial}{\partial \theta} \\ \bar{\mathbf{V}} = \mathbf{V} + Pe\hat{\mathbf{z}} \times r\hat{\mathbf{r}} \\ \bar{\omega} = \omega + 2Pe \\ \nabla^2\bar{\psi} = \nabla^2\psi - 2Pe \\ \bar{\psi} = \psi + \dfrac{Pe}{2}(1 - r^2) \\ \left.\dfrac{\partial T}{\partial t}\right|_{r,\bar{\theta}} = \left.\dfrac{\partial T}{\partial t}\right|_{r,\theta} - Pe\dfrac{\partial T}{\partial \bar{\theta}} \end{cases} \tag{2.22}$$

the last relationship transforming the time derivative of the temperature.

It has to be noted that in this coordinate system, the problem becomes of the mixed convection type. Without density effects, the motion of the boundary produces a solid body rotation of the fluid mass. The velocity corresponding to the solid body rotation is not in general of the order ϵ and would give rise to a term equivalent to the centrifugal force field of equation (2.9). Appendix A provides the demonstration.

For weak rotational speeds, steady state solutions are obtained in the non-

rotating coordinate system.

2.2 GOVERNING EQUATIONS FOR ANISOTROPIC POROUS CYLINDER

2.2.1 Rotating Coordinate System

The isotropic porous medium is a particular case of an anisotropic porous medium. To apply the governing equations to both isotropic and anisotropic porous media, a generalized form of the governing equations is given below. The momentum equation for the flow in a rotating isotropic porous medium may be derived from the Navier-Stokes equation for a continuum fluid [46] in a rotating coordinate system as

$$\frac{\partial \mathbf{V}_f'}{\partial t'} + (\mathbf{V}_f' \cdot \nabla)\mathbf{V}_f' = -\frac{1}{\rho'}\nabla p' + \nu \nabla^2 \mathbf{V}_f' + \mathbf{g}'(t) - \boldsymbol{\Omega}' \times (\boldsymbol{\Omega}' \times \mathbf{r}') - 2\boldsymbol{\Omega}' \times \mathbf{V}_f' \tag{2.23}$$

In this equation, the last two terms on the right-hand side represent the centrifugal force and Coriolis force, respectively. $\mathbf{V}_f'$ is the fluid velocity vector. The geometry is expressed in Fig. 2.2*a*.

By volumetric averaging Eq. (2.23) and by neglecting the local and convective acceleration terms on the left-hand side [47, 48], the following momentum equation for flow in a porous medium results:

$$\frac{\mu}{K}\mathbf{V}' - \frac{\mu}{\epsilon}\nabla^2 \mathbf{V}' = -\nabla p' + \rho' \mathbf{g}'(t) - \rho' \boldsymbol{\Omega}' \times (\boldsymbol{\Omega}' \times \mathbf{r}') - 2\frac{\rho'}{\epsilon}\boldsymbol{\Omega}' \times \mathbf{V}' \tag{2.24}$$

where $\mathbf{V}'$ is the filtration velocity, K, the permeability and ϵ, the porosity of solid matrix. The first and second terms on the left-hand side of (2.24) are the Darcy and Brinkman terms, respectively. The former expresses the viscous resistance of the solid matrix and the latter accounts for the viscous effects of the boundaries. In the rotating coordinate frame, the body force terms include the time-dependent

external gravity field, $\mathbf{g}'(t)$, the centrifugal force field, and the Coriolis term, the volumetric averaging being straightforward for the last term because Ω' is uniform throughout the medium.

The ratio of the Brinkman term to the Darcy term leads to the Darcy number

$$Da = K/r_0'^2$$

where r_0 is a characteristic length. The ratio of the Darcy term to the Coriolis term produces a porous medium Ekman number

$$Ek = \nu/K\Omega'$$

Further, the ratio of the third and second terms on the right-hand side of (2.24) represents the centrifugal/gravity force ratio in the form of a Froude number

$$Fr = \Omega'^2 r_0'/g$$

From a practical point of view, the present investigation is limited to Darcy numbers smaller than 10^{-6}. Consequently, the Brinkman term is expected to have a negligible effect on the results [49], and will not be considered. Equation (2.24) becomes

$$\frac{\mu}{K}\mathbf{V}' = -\nabla p' + \rho'\mathbf{g}'(t) - \rho'\mathbf{\Omega}' \times (\mathbf{\Omega}' \times \mathbf{r}') - 2\frac{\rho'}{\epsilon}\mathbf{\Omega}' \times \mathbf{V}' \qquad (2.25)$$

In some cases of the present study it will be assumed that the angular speed $\mathbf{\Omega}'$ is small enough so that rotational effects can be neglected with respect to the viscous resistance and the gravity field (i.e., large Ek and small Fr are assumed). This is justified for certain food processing problems. For example, for a porous medium consisting of spheres of 2 mm diameter, saturated with water, it approximately results $K = 4 \times 10^{-9} m^2$ and $\nu = 1 \times 10^{-6} m^2 s^{-1}$. If the cylinder has a diameter of about 6 cm or less, and the rotation rate is restricted to 4 rad s^{-1} or less, the

associated Ek and Fr ranges are $Ek > 60$ and $Fr < 0.1$. Neglecting rotational effects, Eq. (2.25) becomes the well-known Darcy equation

$$\frac{\mu}{K}\mathbf{V}' = -\nabla p' + \rho'\mathbf{g}'(t) \tag{2.26}$$

However if the large rotation speeds, for which the centrifugal force field can not be neglected or ever becomes predominant, are introduced to the present study, then Ek may be small and Fr large. Nevertheless, as mentioned in [29], the present study is dealing with two-dimensional cases in the (r, θ) plane for which the Coriolis term has no effect on the flow field. The Coriolis term modifies the pressure field so that the reduced pressure can be redefined to eliminate that term, as it was done for the fluid medium [5].

Thus, using expression (2.3) for the pressure gradient and applying the Boussinesq approximation, Eq. (2.25) becomes

$$\mathbf{V}' = -\frac{K}{\mu}\{\nabla p'_d + \rho'_0\beta(T' - T'_0)[\mathbf{g}'(t) + \Omega'^2\mathbf{r}']\} \tag{2.27}$$

For the case of an anisotropic porous medium, the scalar permeability K in Eq. (2.27) is replaced by a second order permeability tensor K_{ij}. The anisotropy considered has its principal axes oriented in the same direction at every part of the flow domain. Since the geometry involved is of circular shape and cylindrical coordinates are used, the components of the permeability tensor are function of the position in the generalized Darcy equations. The relationship (2.27) may be transformed into

$$R_{ij}\mathbf{V}' = -\frac{\sqrt{K_1 K_2}}{\mu}\{\nabla p'_d + \rho'_0\beta(T' - T'_0)[\mathbf{g}'(t) + \Omega'^2\mathbf{r}']\} \tag{2.28}$$

where Darcy resistivity tensor R_{ij} is expressed as

$$R_{ij} = \frac{\sqrt{K_1 K_2}}{K_{ij}} = \begin{pmatrix} R_{rr} & R_{r\theta} \\ R_{\theta r} & R_{\theta\theta} \end{pmatrix}$$

$$= \frac{1}{\sqrt{R}} \begin{pmatrix} \cos^2(\theta-\theta_k) + R\sin^2(\theta-\theta_k) & \sin(\theta-\theta_k)\cos(\theta-\theta_k)(R-1) \\ \sin(\theta-\theta_k)\cos(\theta-\theta_k)(R-1) & \sin^2(\theta-\theta_k) + R\cos^2(\theta-\theta_k) \end{pmatrix}$$

$$= \frac{1}{\sqrt{R}} \left\{ \begin{bmatrix} 1 & 0 \\ 0 & 1 \end{bmatrix} + (R-1) \begin{bmatrix} \sin^2(\theta-\theta_k) & \sin(\theta-\theta_k)\cos(\theta-\theta_k) \\ \sin(\theta-\theta_k)\cos(\theta-\theta_k) & \cos^2(\theta-\theta_k) \end{bmatrix} \right\}$$

It is noticed that the symmetrical second tensor $R_{i,j}$ can be split to two parts. The first part stands for the standard case of isotropic permeability, and second takes care of modification of the equation due to the anisotropy. This second part is equivalent to the term obtained where a magnetic flux is present and conditions are such that the fluid motion does not affect this flux. R is the ratio of K_2/K_1 and θ_k represents the angular position of the principal axis corresponding to K_2, K_2 and K_1 being extremum permeabilities.

Other governing equations are the continuity and energy equations

$$\nabla \cdot \mathbf{V}' = 0 \tag{2.29}$$

$$(\rho c)_p \frac{\partial T'}{\partial t'} + (\rho c)_f (u' \frac{\partial T'}{\partial r'} + \frac{v'}{r'} \frac{\partial T'}{\partial \theta}) = k \, [\, \frac{1}{r'} \frac{\partial}{\partial r'} (r' \frac{\partial T'}{\partial r'}) + \frac{1}{r'^2} \frac{\partial^2 T'}{\partial \theta^2} \,] - S' \tag{2.30}$$

$(\rho c)_f$ and $(\rho c)_p$ are the volumetric heat capacities of the fluid and saturated porous medium respectively. k is the thermal conductivity of the saturated porous medium. For anisotropic conductivity, the scalar k should be replaced by a second order conductivity tensor. In general, anisotropy in permeability is accompanied by anisotropy in conductivity. However, the effects of anisotropic conductivity are small compared to these of the permeability [50], and the present investigation will be limited to the anisotropy in permeability only. By introducing appropriate dimensionless variables

$$r = r'/r'_0$$

$$t = t'\alpha/\sigma r'^2_0$$

$$(u, v) = (u', v')r'_0/\alpha$$

$$\Omega = \Omega' r'^2_0/\alpha\sigma$$

$$p = p'_d \sqrt{K_1 K_2}/\alpha\mu$$

$$T = (T' - T'_0)/\Delta T'$$

$$\Delta T' = S' r'^2_0/k$$

where $\alpha = k/(\rho c)_f$ is the thermal diffusivity and $\sigma = (\rho c)_p/(\rho c)_f$, the heat capacity ratio.

It is worth noticing that the velocity scale defined above is not equivalent to the length scale divided by the time scale. The dimensional approach used here is standard and absorbs the heat capacity ratio, σ, in the time scale.

The problem in dimensionless form can be stated as follows

Continuity Equation

$$\nabla \cdot \mathbf{V} = 0 \tag{2.31}$$

Momentum Equation

$$R_{ij}\mathbf{V} = -\nabla p - T\,[\,Ra\hat{\mathbf{g}}(t) + Ra_\Omega\, r\hat{\mathbf{r}}\,] \tag{2.32}$$

Energy Equation

$$\frac{DT}{Dt} = \nabla^2 T - 1 \tag{2.33}$$

In equation (2.32), $Ra_\Omega = \beta \Delta T' r_0'^2 \sqrt{K_1 K_2}\Omega'^2/\nu\alpha$ is the Rayleigh number based on centrifugal force, and $Ra = g'\beta r_0' \Delta T' \sqrt{K_1 K_2}/\nu\alpha$, the Rayleigh number based on gravity force. The Rayleigh number Ra defined in this way is more appropriate to describe the results since the two extremum permeabilities, K_1 and K_2, are of the same importance. Consequently, it is possible to isolate in a better way the effects of the permeability ratio, R, from other effects normally attributed to a change in Rayleigh number.

The component forms of Eq. (2.32) that are useful in following chapters are given as

$$\begin{cases} u\,R_{rr} + v\,R_{r\theta} = -Ra\,T\,\cos\phi - Ra_\Omega\,T\,r - \dfrac{\partial p}{\partial r} \\ u\,R_{\theta r} + v\,R_{\theta\theta} = Ra\,T\,\sin\phi - \dfrac{\partial p}{r\partial\theta} \end{cases} \qquad (2.34a, b)$$

where

$$\phi = \theta + Pe^*\,t \qquad (2.35)$$

This equation differs from Eq. (2.14) because the form of Peclet number used here ($Pe^* = \sigma\Omega' r_0'^2/\alpha$) is specific to the porous medium; it arises from the fact that the time scale used here is different from that of the fluid.

To eliminate the pressure gradient, one has to take the curl of Eq. (2.32). When the derivative is taken with respect to θ in the (r, θ) coordinate system, it should be taken into account that each element of R_{ij} is a function of θ. This operation eliminates the pressure gradient and yields the following stream function equation

$$R_{rr}\frac{\partial^2\psi}{r^2\partial\theta^2} - 2R_{r\theta}\frac{\partial^2\psi}{r\partial r\partial\theta} + R_{\theta\theta}\frac{1}{r}\frac{\partial}{\partial r}(r\frac{\partial\psi}{\partial r}) + \frac{1-R}{r}[-\frac{\partial\psi}{r\partial\theta}\sin 2(\theta-\theta_k) + \frac{\partial\psi}{\partial r}\cos 2(\theta-\theta_k)] = -Ra(\frac{\partial T}{\partial r}\sin\phi + \frac{\partial T}{r\partial\theta}\cos\phi) - Ra_\Omega\frac{\partial T}{\partial\theta} \qquad (2.36)$$

where ϕ is a function of time and given by Eq. (2.35). The stream function, ψ, is

related to the velocity components u, v according to

$$u = \frac{1}{r}\frac{\partial \psi}{\partial \theta}, \qquad v = -\frac{\partial \psi}{\partial r} \tag{2.37}$$

Thus the continuity equation

$$\frac{1}{r}\frac{\partial ru}{\partial r} + \frac{1}{r}\frac{\partial v}{\partial \theta} = 0 \tag{2.38}$$

is automatically satisfied, and the energy equation can be written in full, and expressed in terms of the stream function

$$\frac{\partial T}{\partial t} + \frac{1}{r}\frac{\partial \psi}{\partial \theta}\frac{\partial T}{\partial r} - \frac{\partial \psi}{\partial r}\frac{1}{r}\frac{\partial T}{\partial \theta} = \frac{1}{r}\frac{\partial}{\partial r}(r\frac{\partial T}{\partial r}) + \frac{1}{r^2}\frac{\partial^2 T}{\partial \theta^2} - 1 \tag{2.39}$$

For an isotropic porous medium, the matrix R_{ij} becomes the unit matrix, I_{ij}

$$R_{ij} = I_{ij} = \begin{pmatrix} 1 & 0 \\ 0 & 1 \end{pmatrix}$$

and Eq. (2.36) is simplified to

$$\frac{1}{r}\frac{\partial}{\partial r}(r\frac{\partial \psi}{\partial r}) + \frac{\partial^2 \psi}{r^2 \partial \theta^2} = -Ra(\frac{\partial T}{\partial r}\sin\phi + \frac{\partial T}{r\partial \theta}\cos\phi) - Ra_\Omega \frac{\partial T}{\partial \theta} \tag{2.40}$$

2.2.2 Non-Rotating Coordinate System

As described in section of 2.1.2, the governing equations in the rotating coordinate system can be easily transformed into the non-rotating coordinate system, shown in Fig. 2.2*b*.

It is seen from Eqs. (2.35) and (2.36) that the rotation of the gravity vector generates a time periodic recurrence of the solution equal to $2\pi/Pe^*$. The equations

for the case where the time dependence is eliminated may be obtained by the use of the following relationships

$$\begin{cases} \bar{r} = r \\ \bar{\theta} = \theta + Pe^* t \\ \bar{p} = p \\ \bar{T} = T \\ \dfrac{\partial}{\partial \bar{r}} = \dfrac{\partial}{\partial r} \\ \dfrac{\partial}{\partial \bar{\theta}} = \dfrac{\partial}{\partial \theta} \\ \bar{\mathbf{V}} = \mathbf{V} + Pe^* \hat{\mathbf{z}} \times r\hat{\mathbf{r}} \\ \bar{\psi} = \psi + \dfrac{Pe^*}{2}(1 - r^2) \\ \nabla^2 \bar{\psi} = \nabla^2 \psi - 2Pe^* \\ \left.\dfrac{\partial T}{\partial t}\right|_{r,\bar{\theta}} = \left.\dfrac{\partial T}{\partial t}\right|_{r,\theta} - Pe^* \dfrac{\partial T}{\partial \bar{\theta}} \end{cases} \tag{2.41}$$

where the last relationship is used to transform the time derivative of the temperature.

The forms of the Eqs. (2.39), (2.40) and (2.37) in this coordinate system are

$$\frac{1}{\bar{r}}\frac{\partial}{\partial \bar{r}}(\bar{r}\frac{\partial \bar{T}}{\partial \bar{r}}) + \frac{1}{\bar{r}^2}\frac{\partial^2 \bar{T}}{\partial \bar{\theta}^2} = \frac{\partial \bar{T}}{\partial \bar{t}} + \frac{1}{\bar{r}}(\frac{\partial \bar{\psi}}{\partial \bar{\theta}}\frac{\partial \bar{T}}{\partial \bar{r}} - \frac{\partial \bar{\psi}}{\partial \bar{r}}\frac{\partial \bar{T}}{\partial \bar{\theta}}) + 1 \tag{2.42}$$

$$\frac{1}{\bar{r}}\frac{\partial}{\partial \bar{r}}(\bar{r}\frac{\partial \bar{\psi}}{\partial \bar{r}}) + \frac{1}{\bar{r}^2}\frac{\partial^2 \bar{\psi}}{\partial \bar{\theta}^2} = -2Pe^* - Ra(\sin\bar{\theta}\frac{\partial \bar{T}}{\partial \bar{r}} + \frac{\cos\bar{\theta}}{\bar{r}}\frac{\partial \bar{T}}{\partial \bar{\theta}}) - Ra_\Omega \frac{\partial \bar{T}}{\partial \bar{\theta}} \tag{2.43}$$

$$\bar{u} = \frac{1}{\bar{r}}\frac{\partial \bar{\psi}}{\partial \bar{\theta}} \qquad\qquad \bar{v} = -\frac{\partial \bar{\psi}}{\partial \bar{r}} \tag{2.44}$$

In this system of equations, σ does not appear explicitly. It has to be noted that when one wants to recover a dimensional velocity from $\bar{v}$, the product $\bar{v}(\alpha/r_0')$ does not correspond to the sum of the (dimensional) filtration velocity and the (dimensional) azimuthal velocity of the rigid matrix. Appendix B provides another way to obtain this set of equations.

2.3 BOUNDARY CONDITIONS

The above governing equations must be completed by appropriate boundary conditions. In other words, a problem is not defined until the boundary conditions have been properly specified. Specific boundary conditions will be applied to each particular problem.

2.3.1 Hydrodynamic Boundary Conditions

Hydrodynamic boundary conditions for the fluid medium are different from those for the porous medium. In addition, those conditions have different expressions in the rotating and non-rotating coordinate systems. Conditions in the rotating coordinate system only are given below.

A. Fluid Medium: The no-slip condition and impermeability at the solid boundary yields

$$\begin{cases} r = 1: & u = v = \psi = 0 \\ r = 0: & u,\ v,\ \psi < \infty \end{cases} \tag{2.45}$$

Note that the condition at $r = 0$ is a mathematical, not a physical boundary condition.

B. Porous Medium: The no-slip condition does not exist for a Darcy porous medium

but the impermeability of the boundary must be satisfied

$$\begin{cases} r = 1: & u = \psi = 0, \ \ v < \infty \\ r = 0: & u, \ \ v, \ \ \psi < \infty \end{cases} \tag{2.46}$$

2.3.2 Thermal Boundary Conditions

Two kinds of thermal boundary conditions for both fluid and porous media are considered, namely

A. An uniform temperature on the circular boundary, i.e., $T' \mid_{r'=r'_0} = T'_0$, can be written in the following dimensionless form

$$\begin{cases} r = 1: & T = 0 \\ r = 0: & T < \infty \end{cases} \tag{2.47}$$

This boundary condition on T is used together with a non-zero constant heat sink S' uniformly distributed within the whole cylinder.

B. A non-uniform temperature corresponding to a thermal stratification is imposed on the circular boundary, namely $T' \mid_{r'=r'_0} = T'_0 + \Delta T' \cos(\theta - \theta_0)$. Its dimensionless expression reads

$$\begin{cases} r = 1: & T = \cos(\theta - \theta_0) \\ r = 0: & T < \infty \end{cases} \tag{2.48}$$

It should be noticed that in the boundary temperature condition **B** the reference temperature T'_0 does not stand for a real temperature on boundary but only an average value of the boundary temperature distribution, and the characteristic temperature $\Delta T'$ corresponds to the amplitude of the cosine temperature imposed

on the boundary. Moreover, no sink term is involved ($S' = 0$) and the energy equations corresponding to Eqs. (2.21) and (2.39) are taken without the third term at their right hand sides.

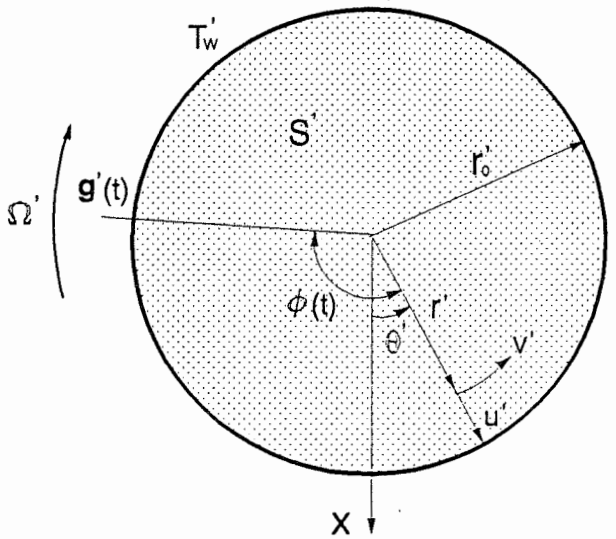

(a) Rotating coordinate system

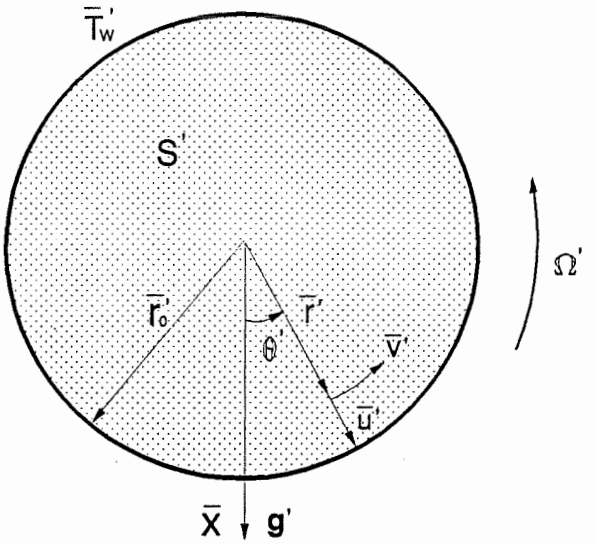

(b) Non-rotating coordinate system

Figure 2.1: Geometry and coordinate system for fluid medium

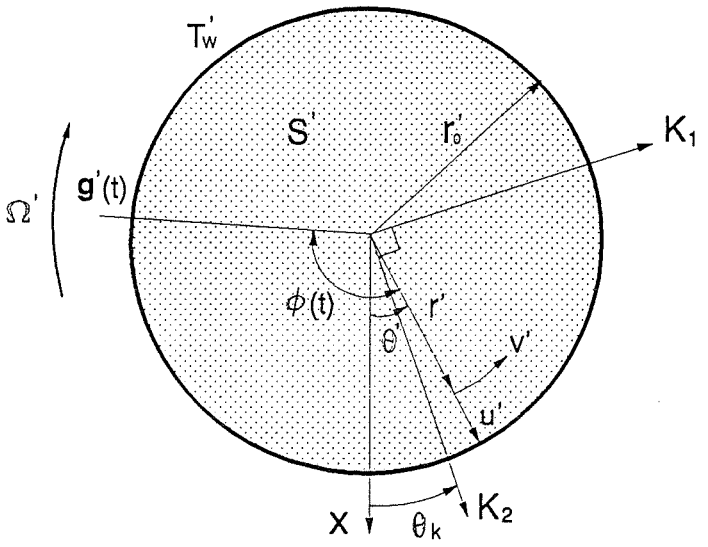

(*a*) Rotating coordinate system

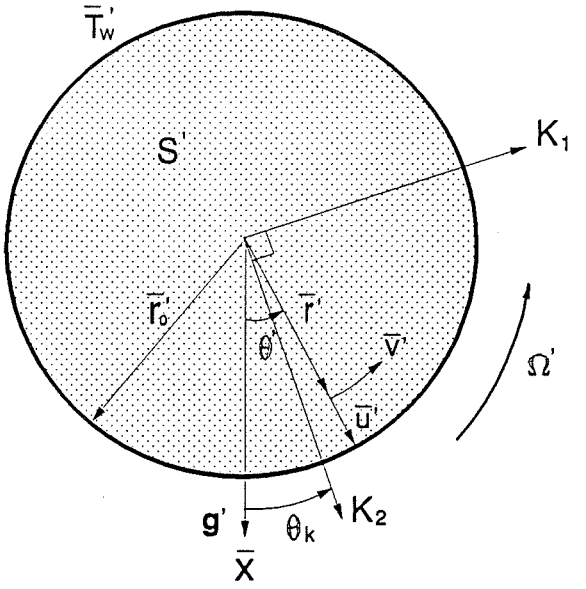

(*b*) Non-rotating coordinate system

Figure 2.2: Geometry and coordinate system for anisotropic porous medium

Chapter 3

NUMERICAL APPROACH

The general equations governing the conservation of mass, momentum and energy in the present problem have been described in the previous chapter. An important task we are facing now is to devise numerical techniques for solving these equations subjected to appropriate boundary conditions. As stated in the previous chapter, the treatment will be limited to two-dimensional incompressible flow, the vorticity-stream function formulation is used instead of equations based on primitive variables.

Aside from numerical techniques, of course, heat transfer and fluid flow processes can also be predicted by experimental investigation or analytical approaches. Analytical methods are largely pencil-and-paper procedures that attempt to provide solutions to problems through the use of simplified assumptions. Many of such assumptions are necessary to make the problems tractable, but they severely limit the applicability of the approach.

Experimental investigation can provide information regarding a particular problem of interest. However, the limitation on hardware required for the model and the complexity in simulating adequately the prototype, make it an difficult task to obtain reliable results. Nevertheless, the information obtained from experiments is extremely valuable in validating the numerical and analytical solutions of the governing equations. Thus, experimental data are used along with computational and analytical solutions of the equations.

The availability of the digital computer has stimulated the rapid growth of the "numerical" or "computational" approach to solve complex problems in heat

transfer. With the advent of electronic digital computers, the introduction of newer numerical techniques are being proposed almost on a daily basis.

There are various numerical techniques to discretize and solve the equations that we encountered within this project, among which the finite difference approach is the most straightforward. This chapter will provide an overview of the role and nature of the numerical techniques in terms of finite difference approach, followed by a detailed description of a well-tested numerical procedure that can handle the specific problem considered in this work as well as a wide variety of engineering problems.

3.1 FINITE DIFFERENCE METHODS

3.1.1 Finite Difference Formulation

In the finite-difference approach, the flow domain is "discretized" so that the dependent variables are considered only at discrete points. The typical two-dimensional grid system is shown in Fig. 3.1, where (i, j) is the grid point in cylindrical coordinate and the superscript n indicates the marching coordinate. Derivatives are approximated by differences resulting in an algebraic representation of the partial differential equation (PDE). The nature of the resulting system of algebraic equations depends on the character of the problem posed by the original PDE (or system of PDEs).

Usually, the second-order central difference approximation is a frequently used scheme for solving the governing equations described in the chapter 2. However, in the convection dominated flow (high Péclet, Reynolds, or Rayleigh numbers), using the second-order central difference approximation to discretize the convective terms in the governing equations may produce wiggly solution. The upwind scheme and

its modified schemes can eliminate these problems. Table 3.1 summarizes central difference and different upwind schemes for a general finite difference representation of an arbitrary scalar function having the following form

$$\left.\frac{\partial uf}{\partial x}\right|_i = A^u f_{i-2} + B^u f_{i-1} + C^u f_i + D^u f_{i+1} + E^u f_{i+2} \tag{3.1}$$

where A^u, B^u, C^u, D^u and E^u are functions of u

Table 3.1 Coefficients of the different schemes

Scheme	A^u	B^u	C^u	D^u	E^u
Central difference	0	$-\frac{u}{2\Delta x}$	0	$\frac{u}{2\Delta x}$	0
1st upwind	0	$-\frac{\lvert u\rvert + u}{2\Delta x}$	$\frac{\lvert u\rvert}{\Delta x}$	$-\frac{\lvert u\rvert - u}{2\Delta x}$	0
2nd upwind	$\frac{\lvert u\rvert + u}{4\Delta x}$	$-\frac{\lvert u\rvert + u}{\Delta x}$	$\frac{3\lvert u\rvert}{2\Delta x}$	$-\frac{\lvert u\rvert - u}{\Delta x}$	$\frac{\lvert u\rvert - u}{4\Delta x}$
3rd upwind	$\frac{\lvert u\rvert + u}{12\Delta x}$	$-\frac{\lvert u\rvert + 2u}{3\Delta x}$	$\frac{\lvert u\rvert}{2\Delta x}$	$-\frac{\lvert u\rvert - 2u}{3\Delta x}$	$\frac{\lvert u\rvert - u}{12\Delta x}$

As shown in Table 3.1, the coefficients A^u and E^u of the central difference and the first-order upwind schemes are equal to zero. The remaining coefficients B^u, C^u and D^u of f_{i-1} , f_i and f_{i+1} form a tridiagonal matrix. Using the higher order upwind schemes, the discretized equations are no longer represented by a tridiagonal matrix. Instead, the algebraic equations become a pentadiagonal matrix.

3.1.2 Discretization of the Governing Equations

For numerical computation, the governing differential equations have to be cast in a discretized form. To simplify the demonstration, only the procedure of discreting the governing equations for a fluid medium in the rotating coordinate system is discussed in this chapter. Owing to the moderate convection flow of the present problem, all the convective and diffusive terms in the equations are

discretized by the Taylor-based, second order central difference scheme, while the time derivatives are approximated by forward differences. The energy equation (2.21) can be discretized as

$$\frac{T_{i,j}^{n+1}-T_{i,j}^{n}}{(\Delta t)}+\frac{r_{i+1}u_{i+1,j}^{n}T_{i+1,j}^{n+1}-r_{i-1}u_{i-1,j}^{n}T_{i-1,j}^{n+1}}{2r_i(\Delta r)}+\frac{v_{i,j+1}^{n}T_{i,j+1}^{n+1}-v_{i,j-1}^{n}T_{i,j-1}^{n+1}}{2r_i(\Delta\theta)}$$
$$=\frac{T_{i+1,j}^{n+1}-2T_{i,j}^{n+1}+T_{i-1,j}^{n+1}}{(\Delta r)^2}+\frac{T_{i+1,j}^{n+1}-T_{i-1,j}^{n+1}}{2r_i(\Delta r)}+\frac{T_{i,j+1}^{n+1}-2T_{i,j}^{n+1}+T_{i,j-1}^{n+1}}{r_i^2(\Delta\theta)^2}-$$
$$1+O[(\Delta t)^2,(\Delta r)^2,(r\,\Delta\theta)^2] \tag{3.2}$$

This formulation is implicit, since more than one unknown appears in the finite difference equation, from which it follows that

$$[\frac{r_{i+1}u_{i+1,j}^{n}-1}{2r_i(\Delta r)}-\frac{1}{(\Delta r)^2}]T_{i+1,j}^{n+1}+[\frac{1-r_{i-1}u_{i-1,j}^{n}}{2r_i(\Delta r)}-\frac{1}{(\Delta r)^2}]T_{i-1,j}^{n+1}+$$
$$[\frac{1}{(\Delta t)}+\frac{2}{(\Delta r)^2}+\frac{2}{r_i^2(\Delta\theta)^2}]T_{i,j}^{n+1}+[-\frac{v_{i,j-1}^{n}}{2r_i(\Delta\theta)}-\frac{1}{r_i^2(\Delta\theta)^2}]T_{i,j-1}^{n+1}+$$
$$[\frac{v_{i,j+1}^{n}}{2r_i(\Delta\theta)}-\frac{1}{r_i^2(\Delta\theta)^2}]T_{i,j+1}^{n+1}=\frac{1}{(\Delta t)}T_{i,j}^{n}-1 \tag{3.3}$$

By defining the coefficients of the unknowns as a, b, c, d and e, and the term in right-hand side as f, equation (3.3) may be written as

$$a_{i,j}T_{i+1,j}^{n+1}+b_{i,j}T_{i-1,j}^{n+1}+c_{i,j}T_{i,j}^{n+1}+d_{i,j}T_{i,j-1}^{n+1}+e_{i,j}T_{i,j+1}^{n+1}=f_{i,j} \tag{3.4}$$

It is obvious that the coefficient matrix is pentadiagonal in Eq.(3.4). The solution procedure for a pentadiagonal system of equations is very time-consuming. One way to overcome the shortcomings and inefficiency of the method described above, is to use a splitting method. This method is known as the alternating direction implicit method (A.D.I.), which is proposed by Roache [51]. The algorithm produces two sets of tridiagonal simultaneous equations to be solved in sequence. The finite difference form of the energy equation in the A.D.I. formulation is then

$$\frac{T_{i,j}^{n+\frac{1}{2}}-T_{i,j}^{n}}{(\frac{\Delta t}{2})}+\frac{r_{i+1}u_{i+1,j}^{n}T_{i+1,j}^{n+\frac{1}{2}}-r_{i-1}u_{i-1,j}^{n}T_{i-1,j}^{n+\frac{1}{2}}}{2r_i(\Delta r)}+\frac{v_{i,j+1}^{n}T_{i,j+1}^{n}-v_{i,j-1}^{n}T_{i,j-1}^{n}}{2r_i(\Delta\theta)}$$
$$=\frac{T_{i+1,j}^{n+\frac{1}{2}}-2T_{i,j}^{n+\frac{1}{2}}+T_{i-1,j}^{n+\frac{1}{2}}}{(\Delta r)^2}+\frac{T_{i+1,j}^{n+\frac{1}{2}}-T_{i-1,j}^{n+\frac{1}{2}}}{2r_i(\Delta r)}+\frac{T_{i,j+1}^{n}-2T_{i,j}^{n}+T_{i,j-1}^{n}}{r_i^2(\Delta\theta)^2}-1 \tag{3.5}$$

and

$$\frac{T_{i,j}^{n+1}-T_{i,j}^{n+\frac{1}{2}}}{(\frac{\Delta t}{2})}+\frac{r_{i+1}u_{i+1,j}^{n}T_{i+1,j}^{n+\frac{1}{2}}-r_{i-1}u_{i-1,j}^{n}T_{i-1,j}^{n+\frac{1}{2}}}{2r_i(\Delta r)}+\frac{v_{i,j+1}^{n}T_{i,j+1}^{n+1}-v_{i,j-1}^{n}T_{i,j-1}^{n+1}}{2r_i(\Delta\theta)}$$
$$=\frac{T_{i+1,j}^{n+\frac{1}{2}}-2T_{i,j}^{n+\frac{1}{2}}+T_{i-1,j}^{n+\frac{1}{2}}}{(\Delta r)^2}+\frac{T_{i+1,j}^{n+\frac{1}{2}}-T_{i-1,j}^{n+\frac{1}{2}}}{2r_i(\Delta r)}+\frac{T_{i,j+1}^{n+1}-2T_{i,j}^{n+1}+T_{i,j-1}^{n+1}}{r_i^2(\Delta\theta)^2}-1 \quad (3.6)$$

with the truncation error of order $[(\Delta t)^2,(\Delta r)^2,(r\,\Delta\theta)^2]$ [52]. This scheme is unconditionally stable. Equations (3.5) and (3.6) are written in the tridiagonal form as

$$A_1^T T_{i-1,j}^{n+\frac{1}{2}}+B_1^T T_{i,j}^{n+\frac{1}{2}}+C_1^T T_{i+1,j}^{n+\frac{1}{2}}=D_1^T \quad (3.7)$$

and

$$A_2^T T_{i,j-1}^{n+1}+B_2^T T_{i,j}^{n+1}+C_2^T T_{i,j+1}^{n+1}=D_2^T \quad (3.8)$$

where

$$\begin{aligned}
A_1^T &= -\frac{v_{i,j-1}^{n}}{2r_i(\Delta\theta)}-\frac{1}{r_i^2(\Delta\theta)^2}\\
B_1^T &= \frac{1}{(\Delta t)}+\frac{2}{r_i^2(\Delta\theta)^2}\\
C_1^T &= \frac{v_{i,j+1}^{n}}{2r_i(\Delta\theta)}-\frac{1}{r_i^2(\Delta\theta)^2}\\
D_1^T &= [\frac{r_{i-1}u_{i-1,j}^{n}-1}{2r_i(\Delta r)}+\frac{1}{(\Delta r)^2}]T_{i-1,j}^{n+\frac{1}{2}}+[\frac{1}{(\Delta t)}-\frac{2}{(\Delta r)^2}]T_{i,j}^{n+\frac{1}{2}}\\
&\quad [\frac{1-r_{i+1}u_{i+1,j}^{n}}{2r_i(\Delta r)}+\frac{1}{(\Delta r)^2}]T_{i+1,j}^{n+\frac{1}{2}}-1\\
A_2^T &= \frac{1-r_{i-1}u_{i-1,j}^{n}}{2r_i(\Delta r)}-\frac{1}{(\Delta r)^2}\\
B_2^T &= \frac{1}{(\Delta t)}+\frac{2}{(\Delta r)^2}\\
C_2^T &= \frac{r_{i+1}u_{i+1,j}^{n}-1}{2r_i(\Delta r)}-\frac{1}{(\Delta r)^2}\\
D_2^T &= [\frac{v_{i,j-1}^{n}}{2r_i(\Delta\theta)}+\frac{1}{r_i^2(\Delta\theta)^2}]T_{i,j-1}^{n}+[\frac{1}{(\Delta t)}-\frac{2}{r_i^2(\Delta\theta)^2}]T_{i,j}^{n}+\\
&\quad [-\frac{v_{i,j+1}^{n}}{2r_i(\Delta\theta)}+\frac{1}{r_i^2(\Delta\theta)^2}]T_{i,j+1}^{n}-1
\end{aligned}$$

The solution procedure starts with the solution of the tridiagonal system (3.7). The formulation of Eq. (3.7) is implicit in the θ-direction and explicit in the r-direction; thus the solution at this stage is referred to as the θ sweep. Solving the tridiagonal system of (3.7) provides the necessary data for the right-hand side of Eq. (3.8) to solve the tridiagonal system of (3.8). In this equation, the FDE is implicit in the r-direction and explicit in the θ-direction, and it is referred to as the r sweep. Graphical presentation of the method is shown in Fig. 3.2.

Similarly, the vorticity-transport equation (2.20) can be discretized in the tridiagonal form as

$$A_1^{\omega}\omega_{i-1,j}^{n+\frac{1}{2}} + B_1^{\omega}\omega_{i,j}^{n+\frac{1}{2}} + C_1^{\omega}\omega_{i+1,j}^{n+\frac{1}{2}} = D_1^{\omega} \tag{3.9}$$

and

$$A_2^{\omega}\omega_{i,j-1}^{n+1} + B_2^{\omega}\omega_{i,j}^{n+1} + C_2^{\omega}\omega_{i,j+1}^{n+1} = D_2^{\omega} \tag{3.10}$$

with

$$\begin{aligned}
A_1^{\omega} &= -\frac{v_{i,j-1}^n}{2r_i(\Delta\theta)} - \frac{Pr}{r_i^2(\Delta\theta)^2} \\
B_1^{\omega} &= \frac{1}{(\Delta t)} + \frac{2Pr}{r_i^2(\Delta\theta)^2} \\
C_1^{\omega} &= \frac{v_{i,j+1}^n}{2r_i(\Delta\theta)} - \frac{Pr}{r_i^2(\Delta\theta)^2} \\
D_1^{\omega} &= [\frac{r_{i-1}u_{i-1,j}^n - Pr}{2r_i(\Delta r)} + \frac{Pr}{(\Delta r)^2}]\omega_{i-1,j}^{n+\frac{1}{2}} + [\frac{1}{(\Delta t)} - \frac{2Pr}{(\Delta r)^2}]\omega_{i,j}^{n+\frac{1}{2}} \\
&\quad [\frac{Pr - r_{i+1}u_{i+1,j}^n}{2r_i(\Delta r)} + \frac{Pr}{(\Delta r)^2}]\omega_{i+1,j}^{n+\frac{1}{2}} + \\
&\quad PrRa[\frac{T_{i+1,j}^n - T_{i-1,j}^n}{2\Delta r_i}\sin\phi + \frac{\cos\phi}{r_i}\frac{T_{i,j+1}^n - T_{i,j-1}^n}{2\Delta\theta}] + \\
&\quad PrRa_{\Omega}\frac{T_{i,j+1}^n - T_{i,j-1}^n}{2\Delta\theta} \\
A_2^{\omega} &= \frac{Pr - r_{i-1}u_{i-1,j}^n}{2r_i(\Delta r)} - \frac{Pr}{(\Delta r)^2} \\
B_2^{\omega} &= \frac{1}{(\Delta t)} + \frac{2Pr}{(\Delta r)^2}
\end{aligned}$$

$$
\begin{aligned}
C_2^{\omega} &= \frac{r_{i+1}u^n_{i+1,j} - Pr}{2r_i(\Delta r)} - \frac{Pr}{(\Delta r)^2} \\
D_2^{\omega} &= [\frac{v^n_{i,j-1}}{2r_i(\Delta\theta)} + \frac{Pr}{r_i^2(\Delta\theta)^2}]\omega^n_{i,j-1} + [\frac{1}{(\Delta t)} - \frac{Pr}{r_i^2(\Delta\theta)^2}]\omega^n_{i,j} + \\
&\quad [-\frac{v^n_{i,j+1}}{2r_i(\Delta\theta)} + \frac{Pr}{r_i^2(\Delta\theta)^2}]\omega^n_{i,j+1} + \\
&\quad PrRa[\frac{T^n_{i+1,j} - T^n_{i-1,j}}{2\Delta r_i}\sin\phi + \frac{\cos\phi}{r_i}\frac{T^n_{i,j+1} - T^n_{i,j-1}}{2\Delta\theta}] + \\
&\quad PrRa_{\Omega}\frac{T^n_{i,j+1} - T^n_{i,j-1}}{2\Delta\theta}
\end{aligned}
$$

For the Poisson equation (2.18), the central difference scheme produces the representation of FDE as

$$
\begin{aligned}
-\omega_{i,j} &= \frac{1}{r_i}\frac{\psi_{i+1,j} - \psi_{i-1,j}}{2\Delta r} + \frac{\psi_{i+1,j} - 2\psi_{i,j} + \psi_{i-1,j}}{(\Delta r)^2} + \\
&\quad \frac{1}{r_i^2}\frac{\psi_{i,j+1} - 2\psi_{i,j} + \psi_{i,j-1}}{(\Delta\theta)^2}
\end{aligned} \tag{3.11}
$$

From Eq. (3.11), a general recurrence formula for the line successive over-relaxation (L.S.O.R.) can be obtained by introducing the relaxation parameter β as

$$
\begin{aligned}
\psi^{n+1}_{i,j} &= (1-\beta)\psi^n_{i,j} + \beta\,[\,(\frac{1}{(\Delta r_i)^2} + \frac{1}{2r_i\Delta r_i})\psi^n_{i+1,j} + \\
&\quad (\frac{1}{(\Delta r_i)^2} - \frac{1}{2r_i\Delta r_i})\psi^n_{i-1,j} + \frac{1}{r_i^2(\Delta\theta)^2}(\psi^n_{i,j+1} + \\
&\quad \psi^n_{i,j-1}) + \omega^n_{i,j}\,]\,/(\frac{2}{(\Delta r_i)^2} + \frac{2}{r_i^2(\Delta\theta)^2})
\end{aligned} \tag{3.12}
$$

There is no simple way to determine the optimum value of β. In practice, a trial and error approach is used to compute an optimal value (β_{opt}) for a particular problem.

3.1.3 Boundary Condition Discretization

The A.D.I. method requires boundary conditions in both r and θ.

In the implicit r-direction we implicitly solve each entire diameter from boundary to boundary with special coefficients at center point based on rectangular coordinates. Care must be taken in dealing with the mathematical singularity that occurs at the center of cylinder in the polar coordinate system [53]. Following the approach used by Kee and Mckillop [54], the governing equations at the center point is cast into a Cartesian form and a square control volume with sides of length Δr and centered at $r = 0$ is the basis for re-writing the governing equations in a discretized form. The application of this technique makes the center point transparent to the flow in all directions.

In the implicit θ-direction periodic boundary conditions are imposed to any physical variable f, yielding

$$f(r, \theta, t) = f(r, \theta + 2\pi, t) \tag{3.13}$$

and the resulting matrices of the A.D.I. approach is handled by a matrix partition procedure comparable to the one utilized by Phillips [44]. Details are given in Appendix C.

(a) Velocity

Since the no-slip and impermeable boundary conditions are imposed on the solid wall for fluid medium, the corresponding velocity components are set to zero and the stream function is set to either zero or a constant value.

(b) Vorticity

The discretized formula of boundary conditions for the vorticity in the rotating coordinate system can be obtained by applying Taylor development at the solid wall. It is expressed in terms of second order forms (Woods method) as follows:

$$\psi_M = \psi_{M+1} - \psi_r \Delta r + \frac{\psi_{rr}}{2}(\Delta r)^2 - \frac{\psi_{rrr}}{6}(\Delta r)^3 + \vartheta(\Delta r)^4 \tag{3.14}$$

with the relations between ω and ψ defined in the previous chapter

$$\psi_r = 0 \tag{3.15}$$

$$\psi_{rr} = -\omega_{M+1} \tag{3.16}$$

$$\psi_{rrr} = \frac{\omega_{M+1}}{r_0} - \omega_r \tag{3.17}$$

and the slope of vorticity at the boundary being given by

$$\omega_r = \frac{\omega_{M+1} - \omega_M}{\Delta r}$$

replacing derivatives of ψ by their expressions in (3.14)

$$\frac{\psi_{M+1} - \psi_M}{\Delta r} = -\frac{\omega_{M+1}}{3}\Delta r(1 + \frac{\Delta r}{2r_0}) - \omega_M \frac{\Delta r}{6} + \vartheta(\Delta r)^3$$

Its final form is

$$\omega_{M+1}(1 + \frac{\Delta r}{2r_0}) = 3\frac{\psi_{M+1} - \psi_M}{(\Delta r)^2} - \frac{\omega_M}{2} + \vartheta(\Delta r)^2 \tag{3.18}$$

(c) Temperature

In the present study, the boundary conditions for the energy equation are either an imposed cosine temperature distribution (2.48) or an isothermal condition (2.47) with a constant and uniform heat sink.

3.1.4 Program Procedure

The general numerical solution procedure for the fluid medium, as described by the computational flow chart in Fig. 3.3, consists of the following steps.

1. Generate a grid according to an uniform mesh size.

2. Set initial values of all the variables $u_{i,j}$, $v_{i,j}$, $\omega_{i,j}$, $\psi_{i,j}$ and $T_{i,j}$.

3. Set boundary conditions for velocity, stream function, temperature.

4. Compute the temperature field by solving the energy equation (2.21), alternatively sweeping in θ and r directions. An A.D.I. scheme is employed.
5. Compute the source term consisting of gravity and centrifugal forces in the vorticity-transportation equation (2.20).
6. Compute vorticity on interior grid points by solving the vorticity-transport equation (2.20) and using velocity and updated temperature. The A.D.I. scheme is used again.
7. Solve the Poisson equation (2.18) with S.O.R. to obtain the $\psi_{i,j}$ where updated vorticity $\omega_{i,j}$ is adopted.
8. Calculate the vorticity on the boundary by using the stream function and vorticity at interior points (3.18).
9. Determine velocity components from updated stream function.
10. Numerical computations are carried out until the flow and temperature fields reach the steady-periodic (or steady) state with time increment of 0.0005 for porous medium and 0.00001 for fluid medium. The steady-state is defined based on the following criterion

$$\frac{|\psi|^{n+1}_{max} - |\psi|^{n}_{max}}{|\psi|^{n+1}_{max}} < 10^{-3} \tag{3.19}$$

In addition to this criterion, visual checks are performed of the flow and temperature fields, as represented by streamlines and isotherms respectively, in order to verify that they do not change anymore with time.

The procedure for porous medium differs from the one for fluid medium by replacing the steps 6, 7 and 8 with a single step of computing the stream function equation (2.36) with S.O.R method. The flow chart illustrating the computational

procedure for porous medium is shown in Fig. 3.4.

Solutions for the temperature and flow fields are obtained in this work by the use of an uniform mesh size 18×36 or 36×72. Different time increments were tested to make sure that no effects of the time increments on the results take place.

3.2 COMPARISON TEST

To confirm the accuracy and reliability of the present numerical programs, a series of comparison tests have been carried out and some of results are analyzed in the following paragraphs.

3.2.1 Test for Fluid Medium

The results from the present numerical program for fluid medium was compared with the ones of Takeuchi et al. [36] for non-rotating cylinder. They developed a numerical method for the problem and obtained the solutions for $Pr = 0.7, 1.0, 100$ and a range of modified Grashof numbers $Gr_a = 10^3$ to 10^9. A comparison of results for the Nusselt number from $Ra = 10^4$ to 10^7 is demonstrated in Table 3.2.

Table 3.2 Comparison with the results of Takeuchi et al. [36]

$\dot{Gr}_a$	$\dot{Pr}$	$Ra = \dot{Gr}_a \times \dot{Pr}$	$\dot{Nu}$	$Nu \times 8$
10^3	10	10^4	9.7	9.632
10^4	10	10^5	13.0	12.72
10^5	10	10^6	18.5	18.38
10^6	10	10^7	28.0	27.4725

In this table the values from [36] are maked with a dot on top, and the values of $\dot{Nu}$ were taken approximately from Fig. 9 of [36]. It should be noticed that the

relationships of $Ra = \dot{G}r_a \times \dot{P}r$ and $Nu \times 8 = \dot{N}u$ must be taken into consideration in this comparison.

Fig. 3.5 shows a comparison of the streamline and isotherm patterns for the case with $Ra = 10^7$ ($\dot{P}r = 10$, $\dot{G}r_a = 10^6$). Fig. 3.5*a* was taken from [36] with isotherms on the left and stream functions on the right. Fig. 3.5*b* shows the results from the present study, in which left and right figures are isotherms and stream functions, respectively.

3.2.2 Test for Porous Medium

The accuracy of the present numerical program for porous medium was checked by repeating the computations of Nguyen et al. [37] for non-rotating cylinder, in which they applied an extended perturbation series method. The comparison of results is shown in Table 3.3.

Table 3.3 Comparison with the results of Nguyen et al. [37]

Ra	$\dot{N}u(1)$	$\dot{N}u(2)$	$\dot{N}u(3)$	$Nu \times 8$	Error (%)
100	8.988	8.988	8.974	8.976	0.02
200	10.155	10.138	10.109	10.108	0.01
500	12.847	12.459	12.391	12.393	0.02
1000	15.949	14.803	14.727	14.730	0.02
2000	20.014	17.453	17.672	17.670	0.01
5000	27.133	21.797	22.690	22.666	0.11
10000	34.179	26.749	27.487	27.402	0.31

in which $\dot{N}u(1), \dot{N}u(2)$ and $\dot{N}u(3)$ represented Nusselt numbers from three different methods, i.e., the direct summation of series, Levin's u-transform of series and finite-difference solutions, respectively. Here again the values from [37] are maked with a dot on top, and the relationship of $Nu \times 8 = \dot{N}u$ is also needed in transformation of both results. The results are found to agree with Method (3), which was regarded as the approach with the best results for the problem, within 0.01% to 0.31%.

Fig. 3.6 shows a comparison in streamline and isotherm patterns for the case of $Ra = 5000$. Fig. 3.6*a* gives the results from [37], in which isotherms are placed on the left and stream functions on the right. The results from the present study is given in Fig. 3.6*b* with isotherms on the left and stream functions on the right, respectively. It is seen that the present solutions agree quite well with those of Nguyen et al. [37].

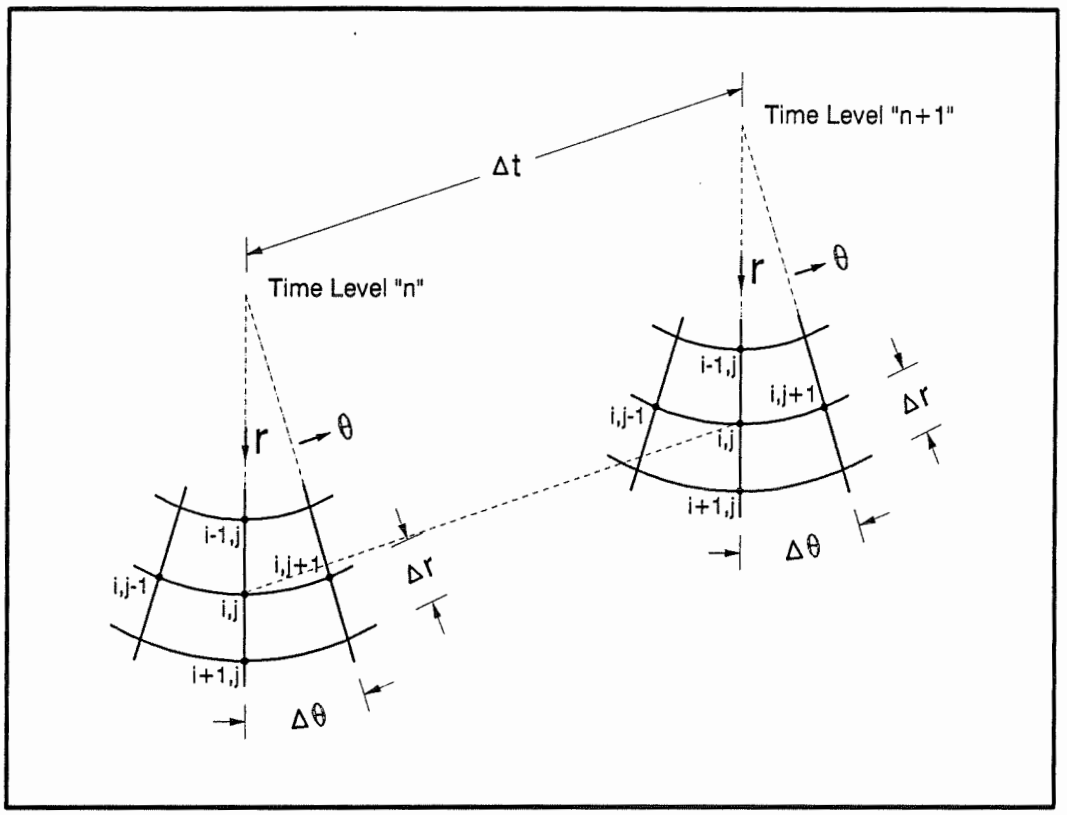

Figure 3.1: Computational grid system

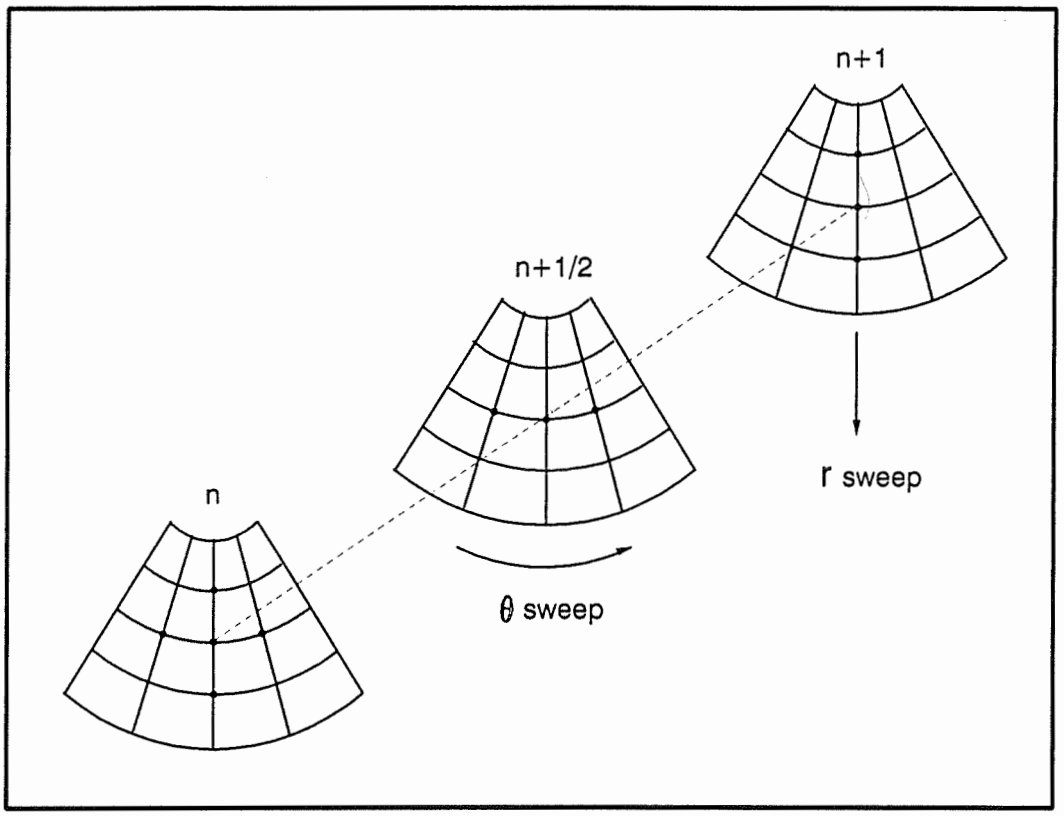

Figure 3.2: Illustration of the grid system for the ADI method

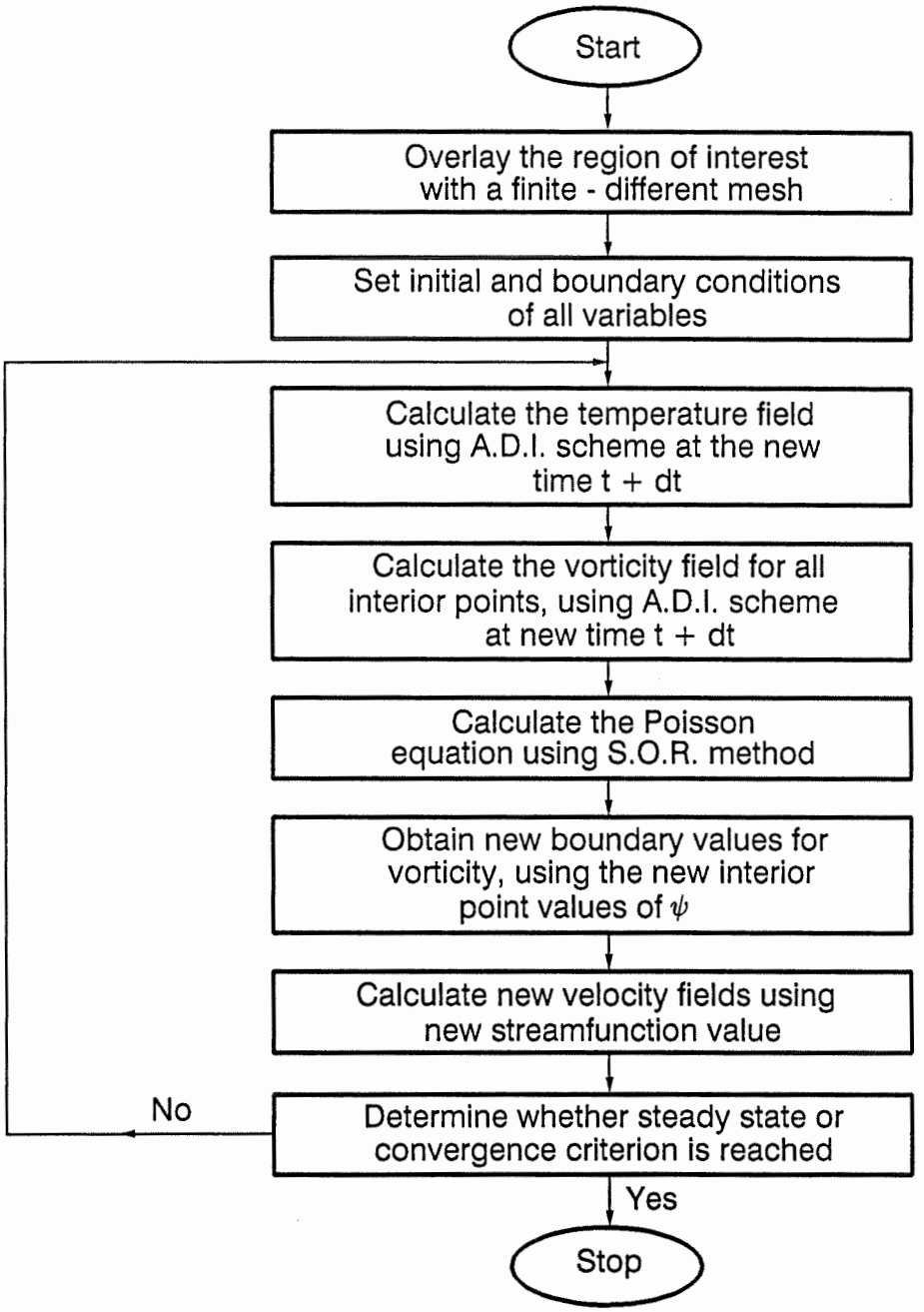

Figure 3.3: Computational flow chart for fluid medium

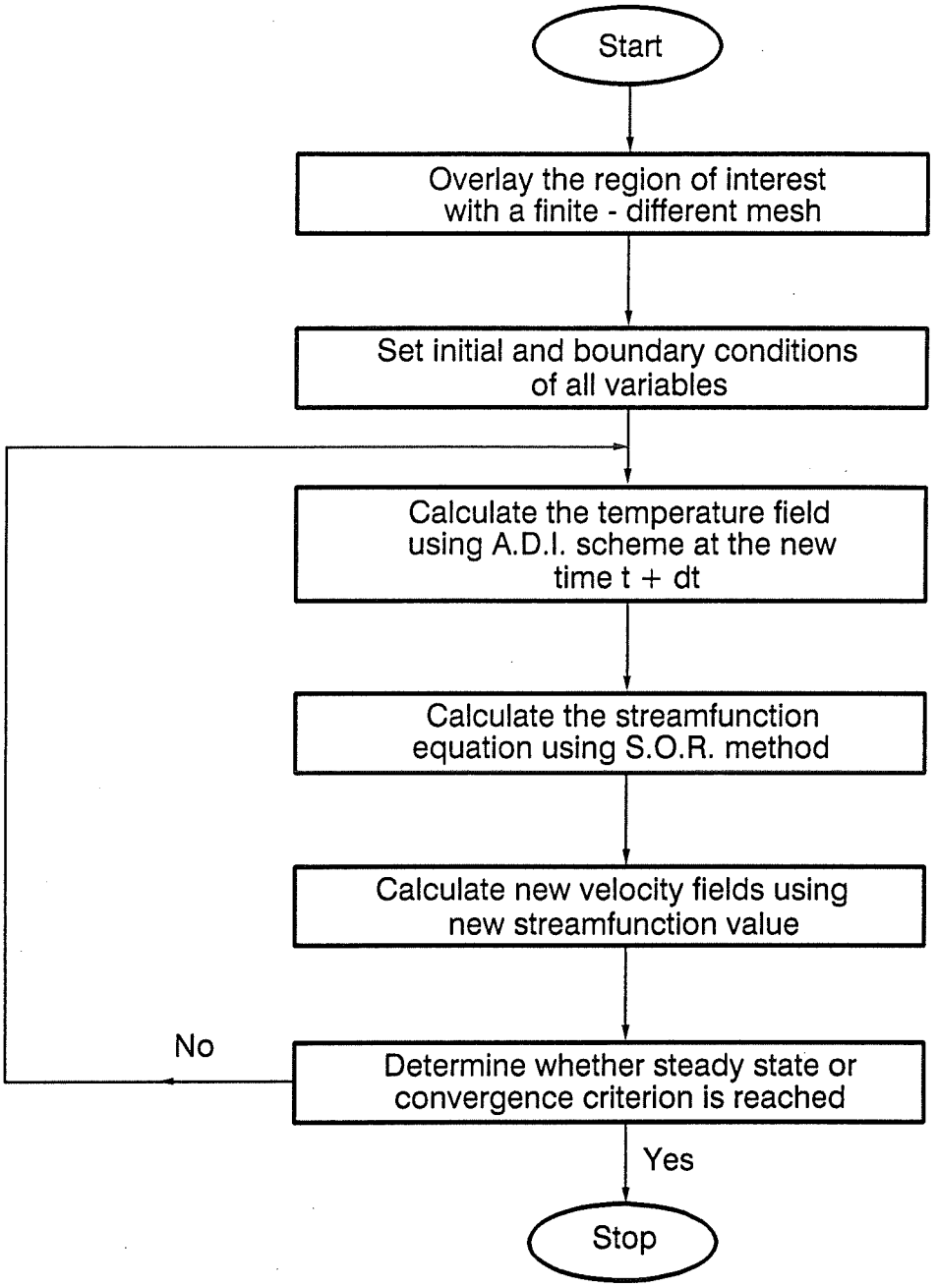

Figure 3.4: Computational flow chart for porous medium

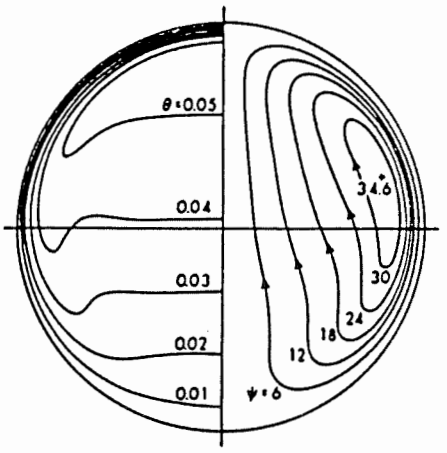

$\dot{P}r = 10$, $\dot{G}r_a = 10^6$, $\psi_{\max} = 34.6$, $\dot{N}u = 28.0$

(a) Takeuchi's result

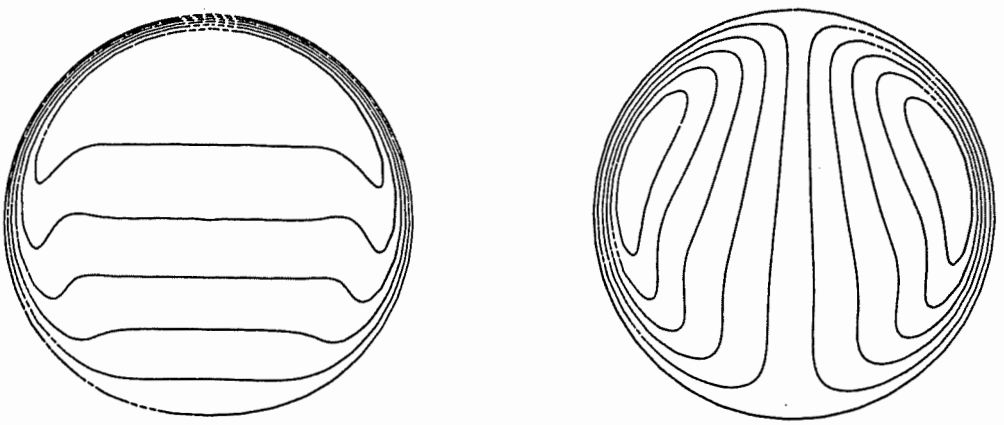

$Ra = 10^7$, $\psi_{\max} = 35.2435$, $Nu = 27.4725$

(b) Present result

Figure 3.5: Comparison with the results of Takeuchi et al. [36]

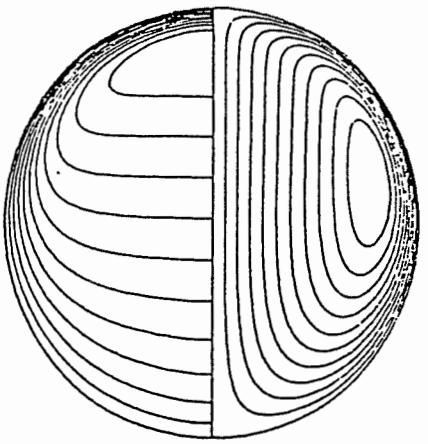

$Pa = 5000$, $\dot{N}u(3) = 22.690$

(a) Nguyen's result

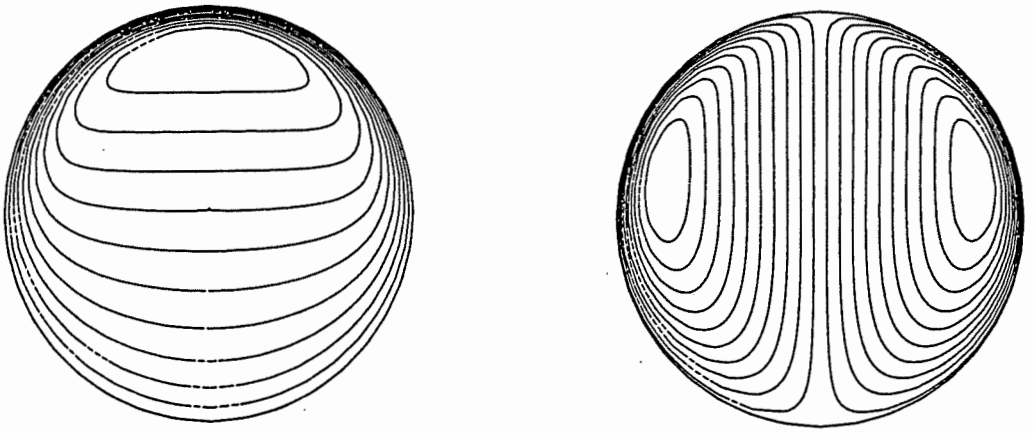

$Ra = 5000$, $Nu = 22.6656$

(b) Present result

Figure 3.6: Comparison with the results of Nguyen et al. [37]

Chapter 4

MIXED CONVECTION IN A LOW ROTATION CYLINDER

In this chapter, the effect of a weak rotation imposed to a horizontal cylinder containing both a fluid medium and a saturated porous medium is studied. Even though the fluid and porous media are described by different momentum equations and have different thermal and dynamic properties (eg., for the fluid medium, the resistance to motion originates from the solid boundary whereas that for a porous medium takes place at every part of the flow domain since the rigid matrix is rotating with the boundary), they still have the same dimensionless energy equations and are confined within the same geometry. Therefore, a qualitatively similar behaviour under same conditions may be expected. The porous and fluid cases are respectively discussed in following two parts of this chapter.

4.1 ISOTROPIC POROUS MEDIUM

The mixed convection within a rotating porous medium enclosed in a circular boundary at an uniform temperature and characterized by a uniformly distributed heat sink has been studied numerically and analytically in this section. Weak rotation regimes only are considered. As described by Vasseur and Robillard [31], this kind of problem is equivalent to the case without heat sink or source and with boundary temperature increasing at a constant rate with time. Thus, it is intended to examine closely the interaction between rotation about a horizontal axis and the gravity force. Here the simple case of an isotropic porous medium, for which a steady flow may be obtained in the non-rotating coordinate system, is investigated. No steady conditions are expected when the porous medium is non-isotropic. In

this chapter both numerical results and perturbation solutions are presented. Results from both approaches coincide. In particular, both approaches reveal that a large part of the saturated fluid does not participate to the rotation at low rotation speed. Thus, the stream function at the center as expressed in a rotating coordinate system may differ largely from zero. However, with increasing angular velocity, the fluid is gradually entrained and a solid body rotation regime develops for which the convective heat transfer is eventually reduced to zero.

4.1.1 Mathematical Formulation

A constant uniform temperature on the circular boundary and a uniform heat sink of intensity S' inside is considered here. The flow in the cylinder is assumed to be two-dimensional in a vertical, $(r,\ \theta)$ plane. The coordinate system $(r,\ \theta)$ is attached to the rotating porous matrix and the boundary as shown in Fig. 2.2a. Thus, the gravity vector, when viewed from the coordinate system $(r,\ \theta)$, moves clockwise at a constant speed Ω'. The uniformly distributed heat sink is represented by S'. The discussion is limited to low permeability, weak angular velocity and isotropic porous medium. Consequently the governing equations are Eqs. (2.38), (2.39) and (2.40). In the last equation the second source term based on the centrifugal force field is dropped.

As already mentioned in Chpater 2, an alternative set of equations in the non-rotating coordinate system $(\bar{r},\ \bar{\theta})$ may be obtained, in which the time dependence is eliminated. The resulting equations are given in section 2.2.2. Once again, for the present problem the source term arising from centrifugal effect is dropped in Eq. (2.43).

4.1.2 Methods of Solution

(a) Perturbation Approach

In addition to the numerical method mentioned in Chapter 3 of this thesis, a perturbation method was developed in order to validate the numerical program at low Ra and Pe and in particular to determine theoretically how Pe increasing from zero affects the symmetry observed when there is no rotation. Neglecting the effect of centrifugal force field, the steady forms ($\partial\bar{T}/\partial\bar{t}$=0) of the equations (2.42) and (2.43) in the coordinate system ($\bar{r}$, $\bar{\theta}$) may be written as follows

$$\frac{1}{\bar{r}}\frac{\partial}{\partial\bar{r}}(\bar{r}\frac{\partial\bar{\psi}}{\partial\bar{r}})+\frac{1}{\bar{r}^2}\frac{\partial^2\bar{\psi}}{\partial\bar{\theta}^2} = -2Pe^*-Ra(\sin\bar{\theta}\frac{\partial\bar{T}}{\partial\bar{r}}+\frac{\cos\bar{\theta}}{\bar{r}}\frac{\partial\bar{T}}{\partial\bar{\theta}}) \tag{4.1}$$

$$\frac{1}{\bar{r}}\frac{\partial}{\partial\bar{r}}(\bar{r}\frac{\partial\bar{T}}{\partial\bar{r}})+\frac{1}{\bar{r}^2}\frac{\partial^2\bar{T}}{\partial\bar{\theta}^2} = \frac{1}{\bar{r}}(\frac{\partial\bar{\psi}}{\partial\bar{\theta}}\frac{\partial\bar{T}}{\partial\bar{r}}-\frac{\partial\bar{\psi}}{\partial\bar{r}}\frac{\partial\bar{T}}{\partial\bar{\theta}})+1 \tag{4.2}$$

with the appropriate boundary conditions

$$\begin{cases} \bar{r}=1: & \bar{T}=\bar{\psi}=\bar{u}=0 \\ \bar{r}=0: & \bar{T},\ \bar{u},\ \bar{v}<\infty \end{cases} \tag{4.3}$$

Eqs. (4.1) to (4.3) define a regular perturbation problem. Expanding the field variables as

$$\bar{\psi}(\bar{r},\bar{\theta}) = \sum_{n=0}^{\infty} Ra^n\,\psi_n \tag{4.4}$$

$$\bar{T}(\bar{r},\bar{\theta}) = \sum_{n=0}^{\infty} Ra^n\,T_n \tag{4.5}$$

and substituting them into the equations (4.1) and (4.2) yields for $n \geq 1$ the sequence

$$\nabla^2 T_n = \frac{1}{\bar{r}}\sum_{i=0}^{n}(\frac{\partial\psi_i}{\partial\bar{\theta}}\frac{\partial T_{n-i}}{\partial\bar{r}}-\frac{\partial\psi_i}{\partial\bar{r}}\frac{\partial T_{n-i}}{\partial\bar{\theta}}) \tag{4.6}$$

$$\nabla^2\psi_n = -(\sin\bar{\theta}\,\frac{\partial T_{n-1}}{\partial\bar{r}}+\frac{\cos\bar{\theta}}{\bar{r}}\frac{\partial T_{n-1}}{\partial\bar{\theta}}) \tag{4.7}$$

where each ψ_n and T_n must satisfy the boundary condition (4.3).

The zeroth-order solution gives the solid-body rotation and the pure conduction state

$$\psi_0 = \frac{Pe^*}{2}(1-\bar{r}^2)$$

$$T_0 = \frac{\bar{r}^2 - 1}{4}$$

The first-order solution is easily obtained for the stream function and reads

$$\psi_1 = a(\bar{r} - \bar{r}^3)\sin\bar{\theta}$$

where $a = 1/16$.

The first-order differential equation for temperature has the form

$$\nabla^2 T_1 = Pe^* \frac{\partial T_1}{\partial \bar{\theta}} + \frac{1}{2}\frac{\partial \psi_1}{\partial \bar{\theta}} \tag{4.8}$$

A second expansion in Pe^* reads

$$T_1 = \sum_{m=0}^{\infty} Pe^{*m} q_m \tag{4.9}$$

Replacing T_1 in (4.8) with the expression (4.9) give the relationships

$$\begin{aligned} \nabla^2 q_0 &= \frac{1}{2}\frac{\partial \psi_1}{\partial \bar{\theta}} \\ \nabla^2 q_m &= Pr \frac{\partial q_{m-1}}{\partial \bar{\theta}} \qquad m > 1 \end{aligned} \tag{25a, b}$$

The solution for q_0 is

$$q_0 = (-\frac{a}{48}\bar{r}^5 + \frac{a}{16}\bar{r}^3 - \frac{a}{24}\bar{r})\cos\bar{\theta} = A_0 \cos\bar{\theta}$$

Higher orders $q_m (m \geq 1)$ can be easily solved on computer from the recurrence formula (25b) which gives

$$q_m = (\frac{d^m}{d\theta^m}\cos\bar{\theta}) \sum_{k=1}^{m+3} b_k^m \bar{r}^{2k-1} = (\frac{d^m}{d\bar{\theta}^m}\cos\bar{\theta}) A_m \qquad m \geq 1$$

with

$$b_k^m = \frac{b_{k-1}^{m-1}}{(2k-1)^2 - 1} \qquad (k \geq 2)$$

and

$$b_1^m = -\sum_{k=2}^{m+3} b_k^m$$

The first-order temperature solution takes the form

$$\begin{aligned} T_1 &= (A_0 - A_2 Pe^{*2} + A_4 Pe^{*4} - \cdots)\cos\bar{\theta} - \\ &\quad (A_1 Pe^{*} - A_3 Pe^{*3} + A_5 Pe^{*5} - \cdots)\sin\bar{\theta} \end{aligned} \tag{4.26}$$

By writing out from Eqs. (4.7) and (4.26) the second order differential expression for ψ_2, the following form is obtained

$$\begin{aligned} \nabla^2\psi_2 &= \frac{1}{2}[(A_1' + A_1\bar{r}^{-1})Pe^{*} - (A_3' + A_3\bar{r}^{-1})Pe^{*3} + \\ &\quad (A_5' + A_5\bar{r}^{-1})Pe^{*5} - \cdots] + \\ &\quad (\cdots)\sin 2\bar{\theta} + (\cdots)\cos 2\bar{\theta} \end{aligned} \tag{4.27}$$

in which the only non-zero terms at $\bar{r} = 0$ are those with no angular dependence. The value of the stream function at the center is of considerable interest since it represents the net flow relative to the rigid matrix circulating around the origin,

$$\psi_c = Ra^2\,\psi_2\Big|_{r=0} = -\int_0^1 v\,dr = \text{const} \qquad \text{for any } \bar{\theta}$$

This net flow is related to the degree of asymmetry of the solution caused by rotation. Thus only the first term on the right hand side of Eq. (4.27) needs to be considered from now on.

The solution of (4.27) has the form

$$\psi_2 = \sum_{k=1}^{\infty}(-1)^{k+1} B_{2k-1} Pe^{*2k-1} + (\cdots)\sin 2\bar{\theta} + (\cdots)\cos 2\bar{\theta}$$

with

$$B_{2k-1} = \sum_{i=0}^{2(k+1)} c_i^{2k-1} r^{2i}$$

and

$$c_i^{2k-1} = \frac{b_i^{2k-1}}{4i} \qquad (i \geq 1)$$
$$c_0^{2k-1} = -\sum_{i=1}^{2(k+1)} b_i^{2k-1}$$

The fact that a value of ψ at the center is sought eliminates all the $\bar{r}$-dependent terms. Thus the final expression for the stream function at the center ($\bar{r} = 0$), up to the second order in Ra and to an arbitrary order in Pe^*, as expressed in the rotating coordinate system, is

$$\psi_c = Ra^2[c_0^1 Pe^* - c_0^3 Pe^{*3} + c_0^5 Pe^{*5} - \cdots] \tag{4.28}$$

where the first three coefficients are $c_0^1 = -1.86496 \times 10^{-5}$, $c_0^2 = -8.65903 \times 10^{-8}$ and $c_0^3 = -4.03259 \times 10^{-10}$. By comparison with a fluid medium presented in section 4.2, a considerably less amount of work is involved here to obtain Eq. (4.28), the stream function Eq. (4.1) being much simpler in the case of a saturated porous medium. Perturbation method is also employed in section 6.1 of this thesis. Only the one leading to the coefficient C for the fluid medium in section 4.2, which involves much more algebra than the others, is given in more detail in Appendix D for reference purpose. Readers interested in coefficients for other parts are invited to write to the author.

Equation (4.28) holds for low Rayleigh numbers and is limited to the range $0 \leq Pe^* <\sim 13$, beyond which it diverges. The heavy line of Fig. 4.1 has been obtained from Eq. (4.28) up to the 35^{th} order. The initial slope for $Pe^* \to 0$, is given by

$$\left.\frac{\partial \psi_c}{\partial Pe^*}\right|_{Pe^*=0} = c_0^1 Ra^2 \tag{4.29}$$

Without convection ($Ra = 0$), the value of the stream function at the center is zero, i.e., the fluid rotates as a solid body with the rigid matrix. With convection, a

part of the fluid mass is tied to the gravity vector, generating a net flow around the center.

(b) Numerical Approach

The perturbation approach is valid to the second order in Ra. Also, the series in Pe has a limited radius of convergence, as seen on Fig. 4.1. Moreover, it provides only the value of ψ at the center. In order to obtain more details about the flow and temperature fields and cover a larger range in Ra and Pe a numerical method based on the finite difference techniques as exposed in Chapter 3 has to be used.

4.1.3 Results and Discussion

The flow and temperature fields for fixed Ra=1000 and Pe^*=0, 110 and 1256 are shown in Fig. 4.2. The center column displays isotherms, the right column displays steady state streamlines in the non-rotating coordinate system and the left column displays streamlines relative to the porous matrix. In the rotating frame (left column), the flows are steady periodic and are locked with the rotating gravity vector. In the non-rotating frame (right column), the flows are steady and the streamlines correspond to the trajectories of fluid particles (those trajectories being based on the filtration velocity). For convenience of observation, the flows in the rotating frame are shown with the gravity vector in the downward position. Without rotation, the free convection produces a flow pattern consisting of two symmetrical and counter-rotating cells, the flow pattern being identical for both coordinate systems, as shown in Fig. 4.2*a*. The stream function at the center ψ_c is equal to zero.

When a rotation rate is introduced ($Pe^* \neq 0$), the above mentioned symmetry does not exist any more. The stream function at the center (ψ_c) takes a value different from zero, as shown in Fig. 4.2*b* (left). Both Figs. 4.1 and 4.3 gives the stream function at the center as a function of Pe^*, for various Ra. In Fig.

4.3, relatively important Ra are involved and the results cover a wide range of Pe^* whereas Fig. 4.1 shows the limiting behavior at low Ra. It is observed in Fig. 4.3 that $|\psi_c|$ increases rapidly and reach a maximum before decreasing toward zero. This behavior holds true for each curve, including $Ra = 1000$ (partly shown on the graph). With Pe^* increasing further, the fluid motion, when viewed from the non-rotating coordinate system, becomes more and more of the solid body rotation type. This is illustrated by the flow pattern on the right in Fig. 4.2*c*. The solid rotation component being removed from the stream function leaves an almost symmetrical flow pattern (shown on the left in the same figure) with ψ_c approaching zero.

Figure 4.1 reproduces numerical results for ψ_c/Ra^2 vs Pe^* at relatively low Ra (Ra=5, 10 and 30). Those results can be compared with the analytical curve obtained from Eq. (4.28) which covers almost entirely the range where ψ_c is increasing to a maximum. This curve is valid for low Rayleigh (second order in Ra). It is observed that the numerical results at Ra=5 and 10 follow quite closely the analytical curve. The maximum value for ψ_c based on those numerical results is reached at $Pe^* \approx 14$. The curve defined by the analytical results and the numerical results at $Ra = 5$ and 10 constitutes a limiting case for low Ra. Higher orders in Ra are no longer negligible for Ra=30 and the numerical results fall below the limiting curve with the maximum shifted to the right.

The initial slope $\partial\psi_c/\partial Pe^*|_{Pe^*\to 0}$ (incipient rotation) is shown in Fig. 4.4 as a function of Ra. Equation (4.29) from the perturbation analysis is given as an inclined dashed line. The numerical results also shown on this graph were obtained by solving for two different and very low $Pe^*(Pe^* < 1)$. They agree with the perturbation analysis for the low range up to $Ra \approx 30$. Beyond this value they separate from the inclined dashed line and tend asymptotically to a limiting maximum slope at very high Ra. The horizontal dashed line in Fig. 4.4 represents the hypothetical slope $|\partial\psi_c/\partial Pe^*|_{Pe^*\to 0} = 0.5$ for which free convection at incipient rotation creates

through the rigid matrix a net flow around the center equivalent to a solid body rotation of the fluid mass with a velocity component $v = -Pe^* \; r|_{Pe^*\to 0}$. It is observed that the numerical results are approaching the limit shown by the inclined dashed line in Fig. 4.3. The fact that the system is approaching that limit at incipient rotation and high Ra shows how strongly the fluid mass resists to the entrainment into solid body rotation along with the rigid matrix. At this very limit and for σ=1, the dimensional filtration (or seepage) velocity component in θ direction would be equal and opposite, as a whole, to $\Omega' r'$, the azimuthal speed imposed to the system. The intrinsic velocity $V' = v'/\epsilon$ (ϵ being the porosity) would be stronger, which means that the fluid particles, as seen from a coordinate system tied to the ground, would even tend to rotate as an average in the direction opposite to the rotation of the rigid matrix. Again, this situation is approached only for $Pe^* \to 0$. As soon as Pe^* increases from zero, the slope $\partial\psi_c/\partial Pe^*$ starts decreasing for all Ra (see Fig. 4.3).

The Darcy resistance of the net circulating flow around the center of the cylinder creates a torque on the rigid matrix. This torque is balanced by the gravitational torque originating from the asymmetric temperature field. A dimensionless torque based on Eq. (2.34*b*) may be defined as

$$\tau = -\int_0^{2\pi}\int_0^1 \frac{\partial\psi}{\partial r}\, r^2\, dr\, d\theta = Ra \int_0^1\int_0^{2\pi} T \sin\theta\, r^2\, dr\, d\theta \qquad (4.30)$$

The torque was computed numerically from the temperature and velocity fields. Results are given in Fig. 4.5. It is observed in the figure that τ follows the trend of ψ_c shown in Fig. 4.3. To some extent, τ is related to ψ_c. If the fluid mass was moving through the rigid matrix in a solid body rotation, i.e., with $v = -2\psi_c\, r$ there would be $\tau = |\pi\psi_c|$. Actually, however, the net circulating flow does not behave as a rigid body, being more intense near the center, owing to the presence of a convective roll of less importance in the flow field, as shown in Fig. 4.2*b* (left). As a consequence,

τ is smaller than $\pi\psi_c$ for all the curves. For instance, $\tau \approx 9.5$ at $Pe^* \approx 45$, for $Ra = 300$. It is found from Fig. 4.3 that the corresponding $\psi_c \approx -4.5$, which gives $|\pi\psi_c| \approx 14.1$.

To characterize the heat transfer rate, a Nusselt number based on T_{av}, the temperature averaged over the domain, may be defined as

$$Nu = \frac{T_{av}|_{\text{pure conduction}}}{T_{av}} \tag{4.31}$$

Fig. 4.6 gives Nu as a function of Pe^* for various Ra. The pure conduction heat transfer corresponds to unity for Nu ($Nu = 1$). It may be observed that Nu decreases from a maximum at $Pe^* = 0$ to unity with Pe^* increasing. This behavior follows from the fact that the fluid particle trajectories (corresponding to the streamlines of Fig. 4.2 on the right) become more and more circular with Pe^* increasing, i.e., the radial amplitude of their motion is reduced and consequently the radial convective hear transfer is lowered.

4.2 FLUID MEDIUM

Natural convection in a fluid medium confined in a horizontal circular cylinder rotating about its axis, with isothermal boundary conditions and uniform internal heat sink, is studied by numerical and perturbation methods. Ladeinde and Torrance [29] treated a similar case where the normal gravity is combined with rotation exclusively by a finite element solution procedure. In order to obtain a deeper understanding of the phsycal behavior in low rotation cylinder, flow patterns and heat transfer rates at incipient convection and for finite amplitude convection are investigated in more detail by using a numerical approach and a regular perturbation method. Here also the concentration is on the weak rotation regimes, for which the centrifugal acceleration is negligible compared to gravity. This latter becomes the main body force of fluid. Governing equations for the two-dimensional flow field are solved in both rotating and non-rotating coordinate systems. Results reveal the

existence of two steady state flow regimes, one with high shear near the boundary, a large part of the fluid mass being tied up to the gravity, and the other being almost equivalent to solid body rotation.

4.2.1 Mathematical Formulation

The geometry for this problem can also be represented in Fig. 2.1*a*. After neglecting the effects of centrifugal force, according to discussion in Chapter 2 of this thesis, the energy equation and vorticity-transport equation in non-inertial coordinate frame are (2.21) and (2.20), the second source term based on the centrifugal force field being dropped from this last equation. The governing parameters for the present problem are the Rayleigh number Ra, the rotational Peclet number $Pe = PrRe$ and Prandtl number, Pr.

4.2.2 Methods of Solution

(a) Perturbation Approach

Similar to the isotropic case in this chapter, one of the features to be considered in a system rotating about a horizontal axis is the effect of incipient rotation combined with free convection, which locks a large mass of the fluid in the cylinder to the gravity vector. How a weak rotation rate affects the symmetry of the two convection cells that are found when no rotation is present can be understood analytically, by means of a perturbation approach.

Eq. (2.20) is the expression in the local (r, θ) coordinates of the non-inertial frame. But periodicity of the solution in the rotating frame requires that all field variables be function of (r, ϕ) only. It is possible therefore to obtain a formulation in terms of $T(r, \phi)$ and $\psi(r, \phi)$ that is better suited for perturbation methods. Using Eqs. (2.14) and (2.18), Eqs (2.20) and (2.21) are transformed into

$$\nabla^4\psi = Re\frac{\partial\nabla^2\psi}{\partial\phi} + \frac{1}{rPr}\{\frac{\partial\psi}{\partial\phi}\frac{\partial\nabla^2\psi}{\partial r} - \frac{\partial\psi}{\partial r}\frac{\partial\nabla^2\psi}{\partial\phi}\} + Ra\{\frac{\partial T}{\partial r}\sin\phi + \frac{\cos\phi}{r}\frac{\partial T}{\partial\phi}\} \quad (4.32)$$

$$\nabla^2 T = RePr\frac{\partial T}{\partial\phi} + \frac{1}{r}\{\frac{\partial\psi}{\partial\phi}\frac{\partial T}{\partial r} - \frac{\partial\psi}{\partial r}\frac{\partial T}{\partial\phi}\} + 1 \quad (4.33)$$

Those last two equations have to be solved with the boundary conditions (2.45) and (2.47).

Equations of (4.32), (4.33), (2.45) and (2.47) define a regular perturbation problem. Expanding the field variables as

$$\psi(r,\theta) = \sum_{n=0}^{\infty} Ra^n\,\psi_n \quad (4.34)$$

$$T(r,\theta) = \sum_{n=0}^{\infty} Ra^n\,T_n \quad (4.35)$$

and substituting them into the equations (4.32) and (4.33) yields for $n \geq 1$ the sequence

$$\nabla^2 T_n = RePr\frac{\partial T_n}{\partial\phi} + \frac{1}{r}\sum_{i=0}^{n}(\frac{\partial\psi_i}{\partial\phi}\frac{\partial T_{n-i}}{\partial r} - \frac{\partial\psi_i}{\partial r}\frac{\partial T_{n-i}}{\partial\phi}) \quad (4.36)$$

$$\nabla^4\psi_n = Re\frac{\partial\nabla^2\psi_n}{\partial\phi}\frac{1}{rPr}\sum_{i=0}^{n}\{\frac{\partial\psi_i}{\partial\phi}\frac{\partial\nabla^2\psi_{n-i}}{\partial r} - \frac{\partial\psi_i}{\partial r}\frac{\partial\nabla^2\psi_{n-i}}{\partial\phi})\} + \sin\phi\frac{\partial T_{n-1}}{\partial r} + \frac{\cos\phi}{r}\frac{\partial T_{n-1}}{\partial\theta} \quad (4.37)$$

where each ψ_n and T_n must satisfy the boundary conditions (2.45) and (2.47).

The zeroth-order solution gives the pure conduction state, that is,

$$\psi_0 = 0$$
$$T_0 = \frac{1}{4}(r^2 - 1)$$

The first-order equations read

$$\nabla^4\psi_1 = Re\frac{\partial\nabla^2\psi_1}{\partial\phi} + \frac{r}{2}\sin\phi \quad (4.38)$$

$$\nabla^2 T_1 = RePr\frac{\partial T_1}{\partial \phi} + \frac{1}{2}\frac{\partial \psi_1}{\partial \phi} \tag{4.39}$$

Since only the initial effects of rotation is of interest in this method, it is more convenient (and considerably simpler) to follow the development done for the porous medium, i.e., to proceed with a second expansion of the form $\psi_1 = f_0 + Ref_1 + \ldots$ in (4.38) and $T_1 = g_0 + Reg_1 + \ldots$ in (4.39) rather than trying to solve the set of equations for arbitrary Reynolds numbers. The second expansion gives

$$\nabla^4 f_0 = \frac{r}{2}\sin\phi \tag{4.40}$$

$$\nabla^4 f_1 = \frac{\partial \nabla^2 f_0}{\partial \phi} \tag{4.41}$$

$$\nabla^2 g_0 = \frac{1}{2}\frac{\partial f_0}{\partial \phi} \tag{4.42}$$

$$\nabla^2 g_1 = Pr\frac{\partial g_0}{\partial \phi} + \frac{1}{2}\frac{\partial f_1}{\partial \phi} \tag{4.43}$$

Solutions can be achieved by separation of variables as before, giving f_0, f_1, g_0, g_1 as linear combinations of terms of the form r^a (a being an arbitrary integer) multiplied by either $\sin\phi$ or $\cos\phi$. Writing out (4.37) in full for $n = 2$, an expansion $\psi_2 = h_0 + Reh_1 + \ldots$, done along the same lines, shows that at any order in Re, all the terms in h_0 will also exhibit a similar angular dependence and, again, vanish at $r = 0$. On the other hand, h_1 contains terms which are independent of ϕ and therefore do not necessarily vanish at $r = 0$, giving

$$\psi_c = CReRa^2 + \ldots \tag{4.44}$$

From this approach, the second order approximation for the stream function at the center is found to be

$$\psi_c = -5.0215 \times 10^{-8}\, Re\, Ra^2 \tag{4.45}$$

for $Pr = 1$. The coefficient C is a function of Pr. For example, $C = -5.7254 \times 10^{-8}$ for $Pr = 0.7$ and $C = -3.6137 \times 10^{-8}$ for $Pr = 7.0$. Detailed algebra leading to the numerical value of C is given in Appendix D for reference purpose.

(b) Numerical Approach

A numerical program has been developed to obtain detailed flow and temperature fields at finite values of Pe and larger Ra exceeding the second order development of the perturbation approach, The details of finite difference techniques on which the numerical program is based can be found in chapter 3.

4.2.3 Results and Discussion

In the following discussion and figures, ψ_c refers the value of the stream function at the center, relative to the coordinate system (r, θ). Here also, the effect of a weak rotation rate (low Pe) on free convection is to destroy the original symmetry with respect to the vertical diameter and to reinforce the cell with flow circulating in the same direction of the imposed rotation. As a consequence, ψ_c takes a value different from zero. Fig. 4.7, based on numerical results, gives ψ_c as a function of Pe for different Ra. It is observed on Fig. 4.7 that ψ_c increases first to reach a maximum value. It then decreases more or less drastically depending on Ra. At low Ra ($Ra \approx 3 \times 10^4$), the curve is smooth; with increasing Ra, the transition from the maximum ψ_c to low values becomes more abrupt. For $Ra = 1 \times 10^5$ and above, the transition is characterized by an oscillating regime represented by a dashed line. Elsewhere, the flow and temperature fields are steady. The parts of the curves for which ψ_c is increasing with Pe correspond to a flow regime with high shear near the boundary (shear flow regime). The dimensionless shear stress integrated over the circular boundary gives the dimensionless torque:

$$\tau = Pr \int_0^{2\pi} \left. \frac{\partial v}{\partial r} \right|_{r=1} d\theta \tag{4.46}$$

This dimensionless torque in Fig. 4.8 is given as a function of Pe. At high Pe, it is observed in Fig. 4.7 and 4.8 that ψ_c and τ have dropped to nearly zero and that the flow regime is again steady for curves $Ra = 10^5$ and 3×10^5. This behavior was also found at higher Pe for the curve $Ra = 10^6$ (not shown). Thus the shear

regime has ceased and for reasons to be explained later in more detail, this new flow regime corresponds to a "solid body rotation regime".

Figure 4.9 represents flow and temperature fields at various Pe for the same value of Rayleigh ($Re = 10^5$). The temperature field at center is given by isotherms; the flow fields relative to (r, θ) and $(\bar{r}, \bar{\theta})$ coordinates are given at left and right respectively. All flow fields in the non-rotating coordinate system (right) are steady. Figure 4.9*a* is given for reference purpose. Figure 4.9*b* corresponds to the shear regime. It is observed that the path of the fluid particles given by the steady state flow field at right column are non-circular within the core. Convective motion is therefore efficient in transporting radially the heat and the temperature field shown at center by isotherms is quite distorted by comparison to the pure conduction temperature field characterized by circular isotherms. For this shear regime the Nusselt number is much larger than unity, as observed in Fig. 4.10. Fig. 4.9*c* corresponds to a solid body rotation regime (steady state). The flow field at right indicates that the paths of the fluid particles are nearly circular throughout the whole domain. The radial amplitude of the motion is weak and consequently, the convective heat transfer is much reduced, almost to the pure conduction value (Nu=1) in Fig. 4.10, the corresponding isotherms shown in Fig. 4.9*c* being nearly circular and concentric.

It is observed in Fig. 4.7 that the initial slope of ψ_c ($\partial\psi_c/\partial Pe|_{Pe\to 0}$) increases with Ra. For $Ra \to 0$, a solid body rotation is obtained at steady state. Thus $\psi_c = 0$ for all Pe. On the other hand without viscosity effects (inviscid limit) the fluid initially at rest would not be entrained by the boundary and would remain at rest with respect to the gravity vector. Thus, ψ_c would take the value shown by the dashed curve in Fig. 4.7. This curve is an asymptotic limit for the initial slope ($\partial\psi_c/\partial Pe|_{Pe\to 0}$), which can be easily computed. The value found is $\partial\psi_c/\partial Pe|_{Pe\to 0}$ (inviscid) = 0.5. Fig. 4.11 compares numerical and analytical results for the initial slope $\partial\psi_c/\partial Pe|_{Pe\to 0}$ as a function of the Rayleigh numbers. The inclined dashed

line corresponds to Eq. (4.45). The inviscid limit is represented by the horizontal line. It is seen on this figure that the numerical results agree with the perturbation solution for low Ra and approach asymptotically the inviscid limit with increasing Ra. Thus, for incipient rotation, at high Ra most of the fluid mass is tied to the gravity and does not participate to the circular motion.

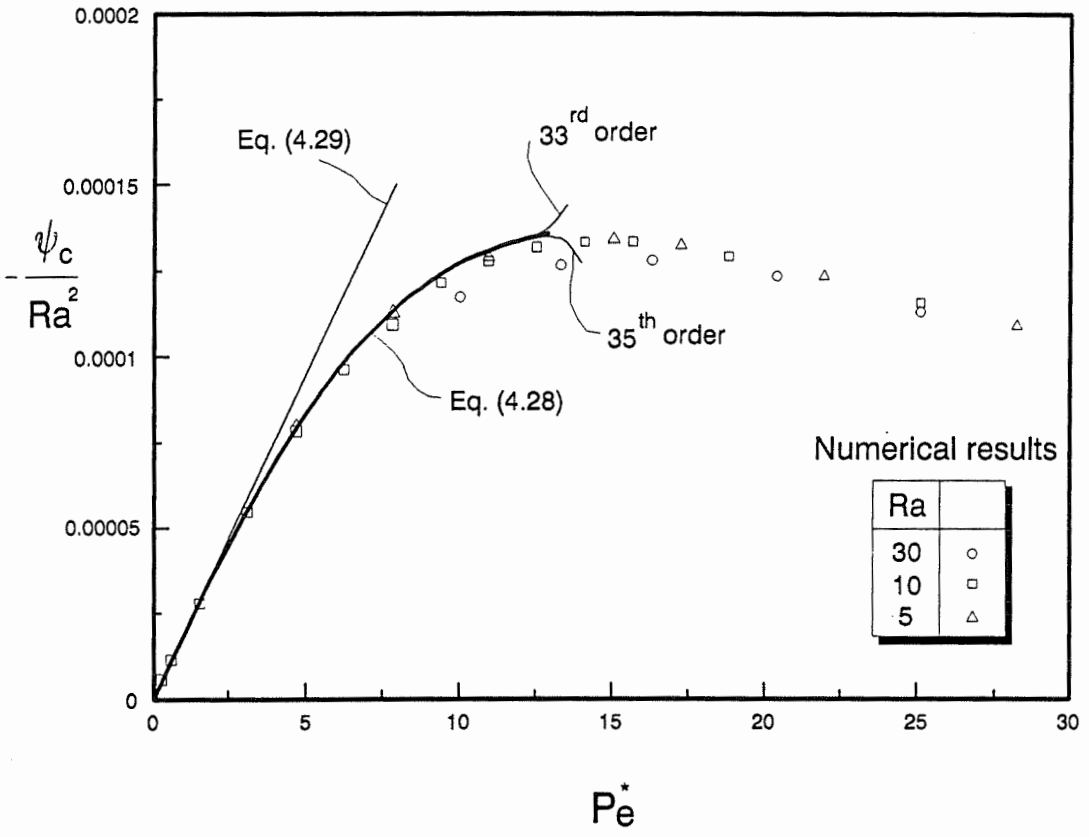

Figure 4.1: $-\psi_c/Ra^2$, function of Pe^* (low Ra)

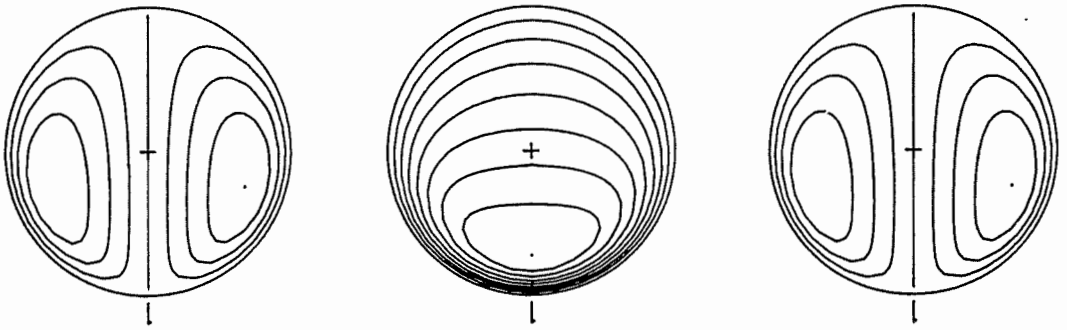

(a) $Pe^* = 0$, $|\psi|_{\max} = 8.32$, $\psi_c = 0$

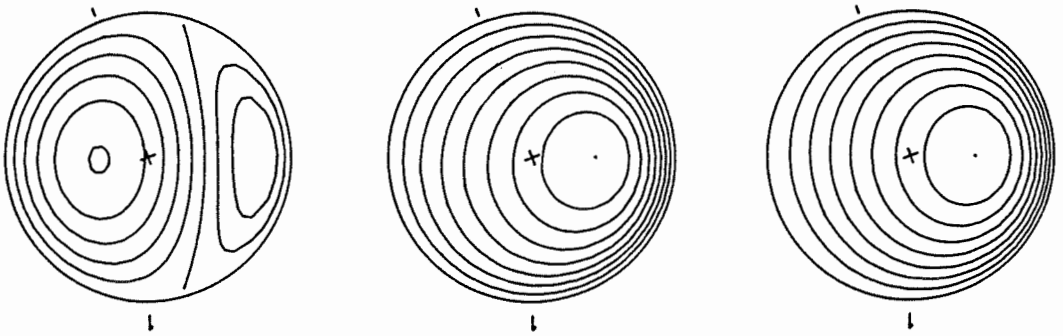

(b) $Pe^* = 110$, $|\psi|_{\max} = 22.44$, $\psi_c = 17.10$

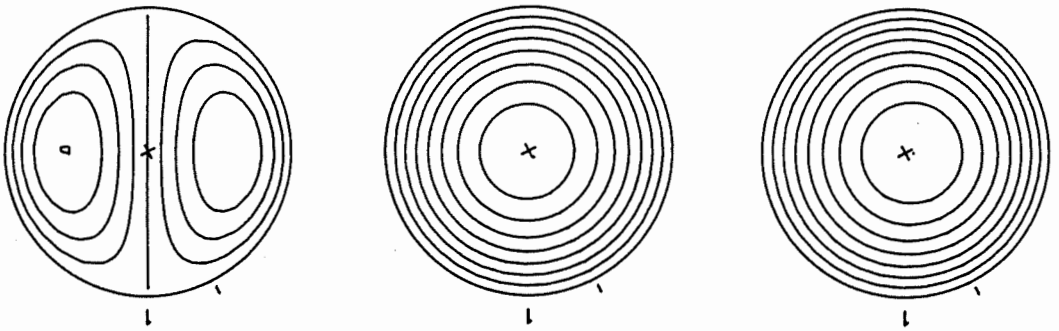

(c) $Pe^* = 1256$, $|\psi|_{\max} = 23.90$, $\psi_c = 0.30$

Figure 4.2: Flow and temperature fields (Ra=1000)

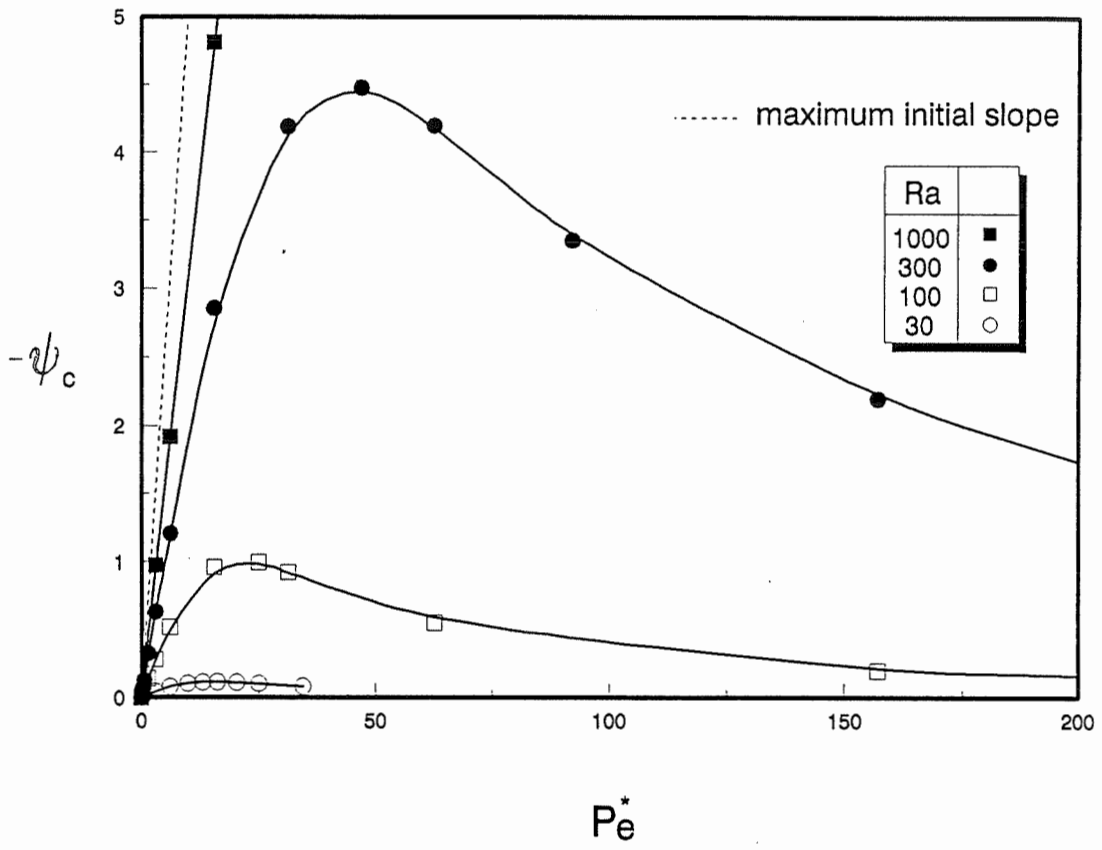

Figure 4.3: $-\psi_c$, function of Pe^* (large Ra)

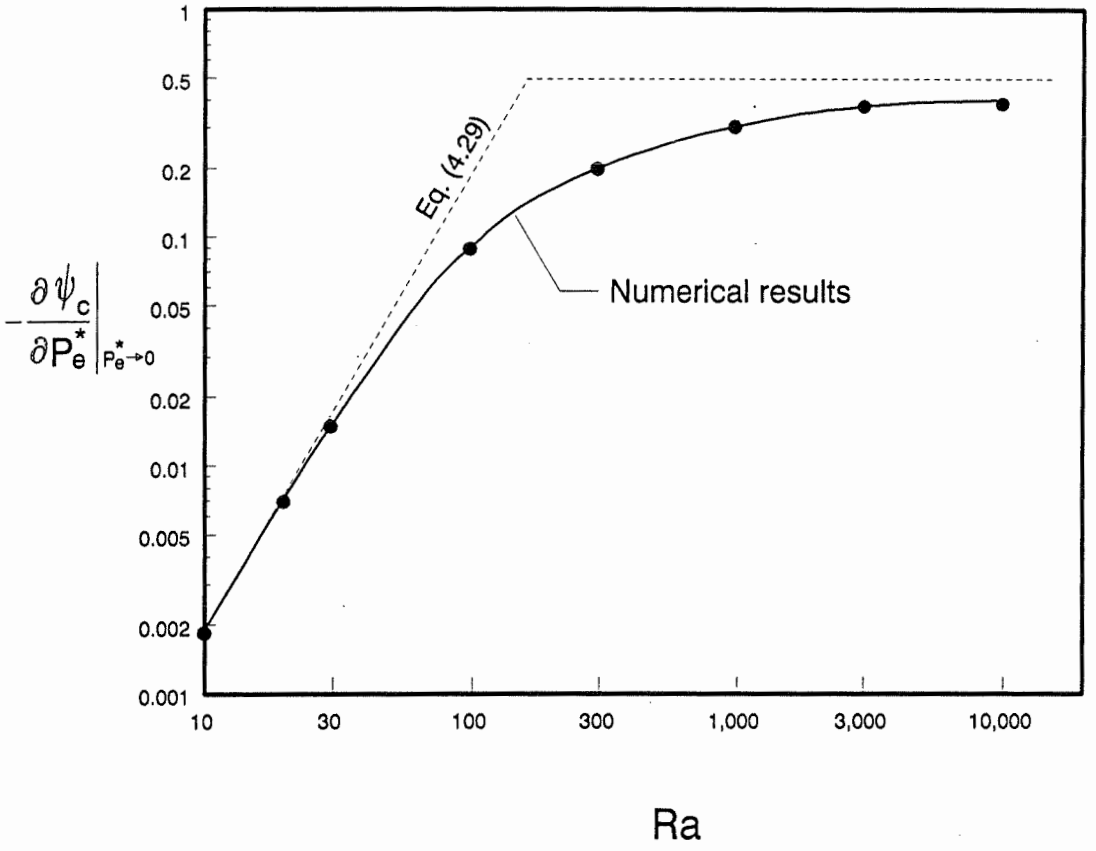

Figure 4.4: Slope of the net circulating flow at incipient rotation

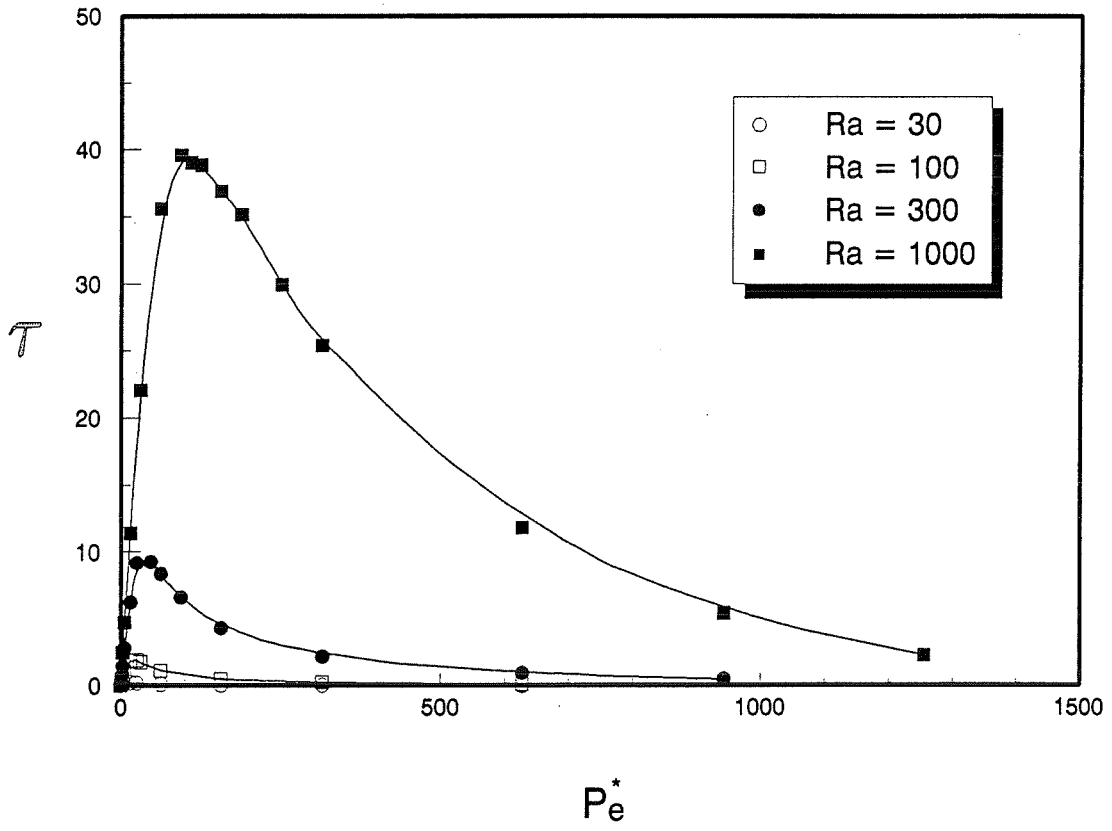

Figure 4.5: τ, function of Pe^*

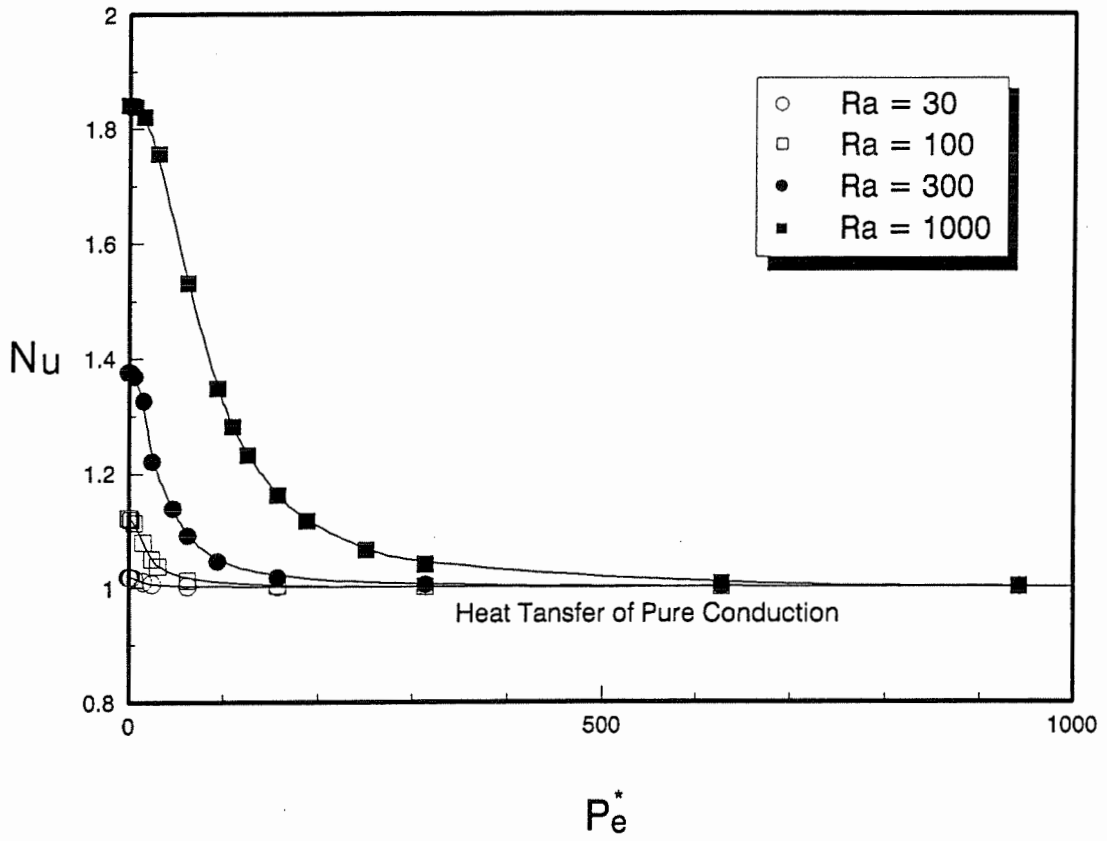

Figure 4.6: Nu, function of Pe^*

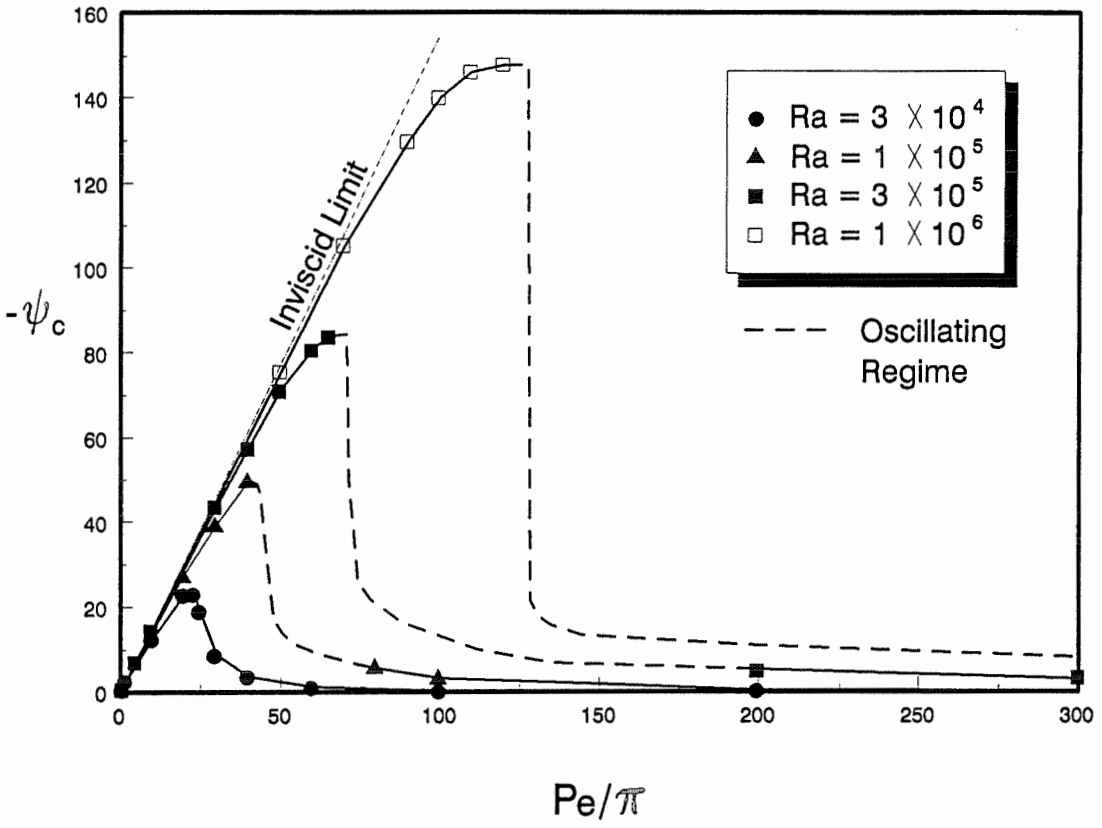

Figure 4.7: Stream function at center, function of Pe

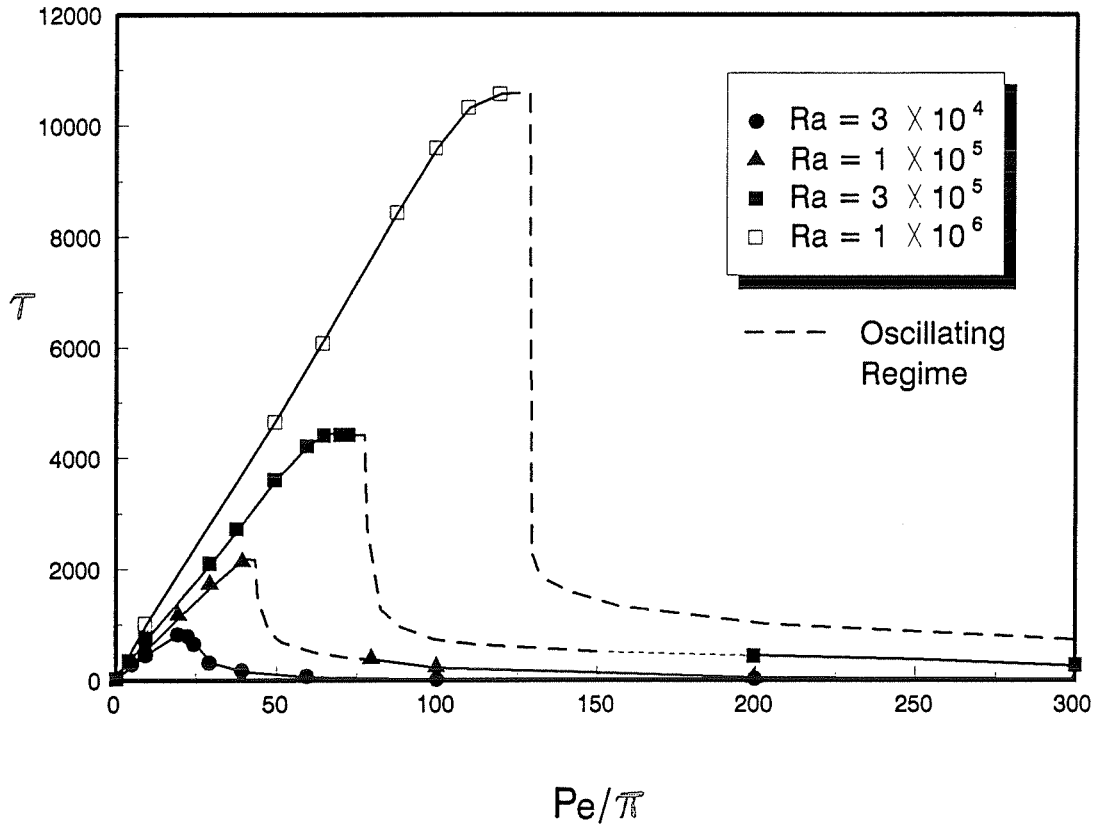

Figure 4.8: Dimensionless shear stress, function of Pe

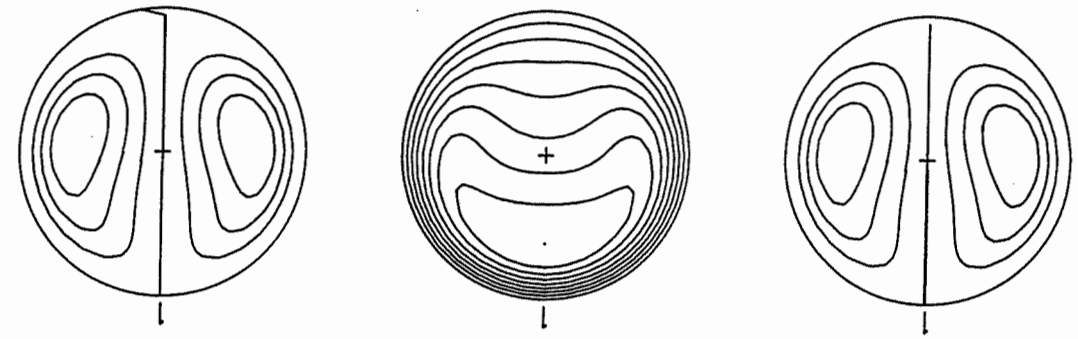

(*a*) Non-rotating, $Pe = 0$

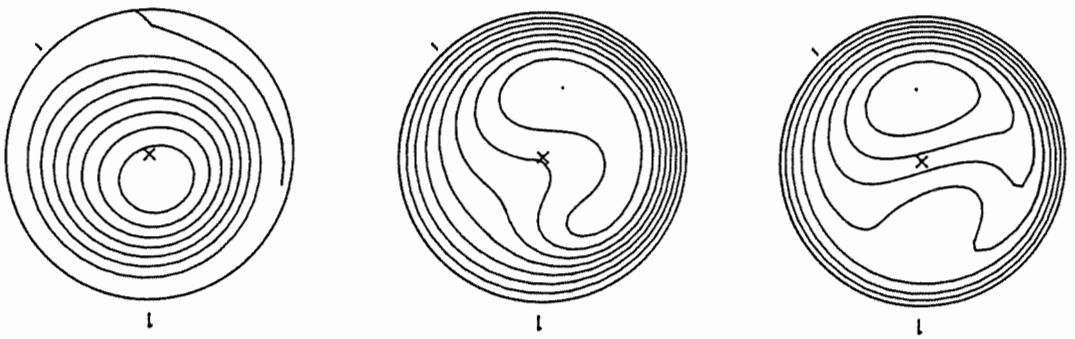

(*b*) Shear flow regime, $Pe = 45\pi$

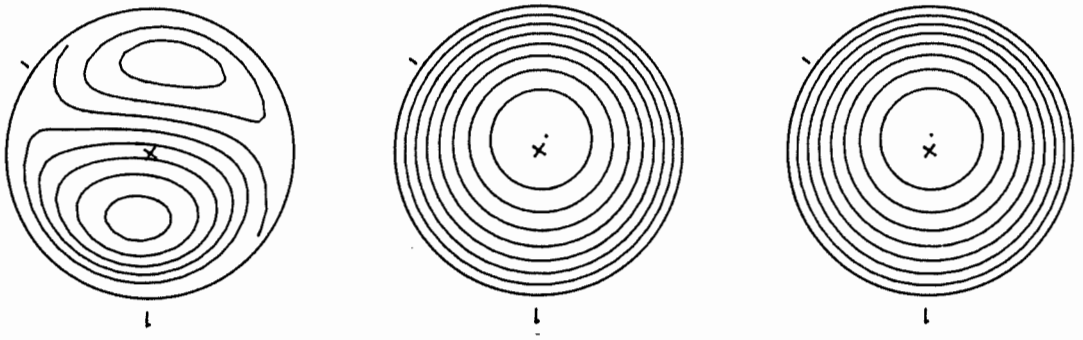

(*c*) Solid rotation regime, $Pe = 80\pi$

Figure 4.9: Flow and temperature fields ($Ra = 10^5$)

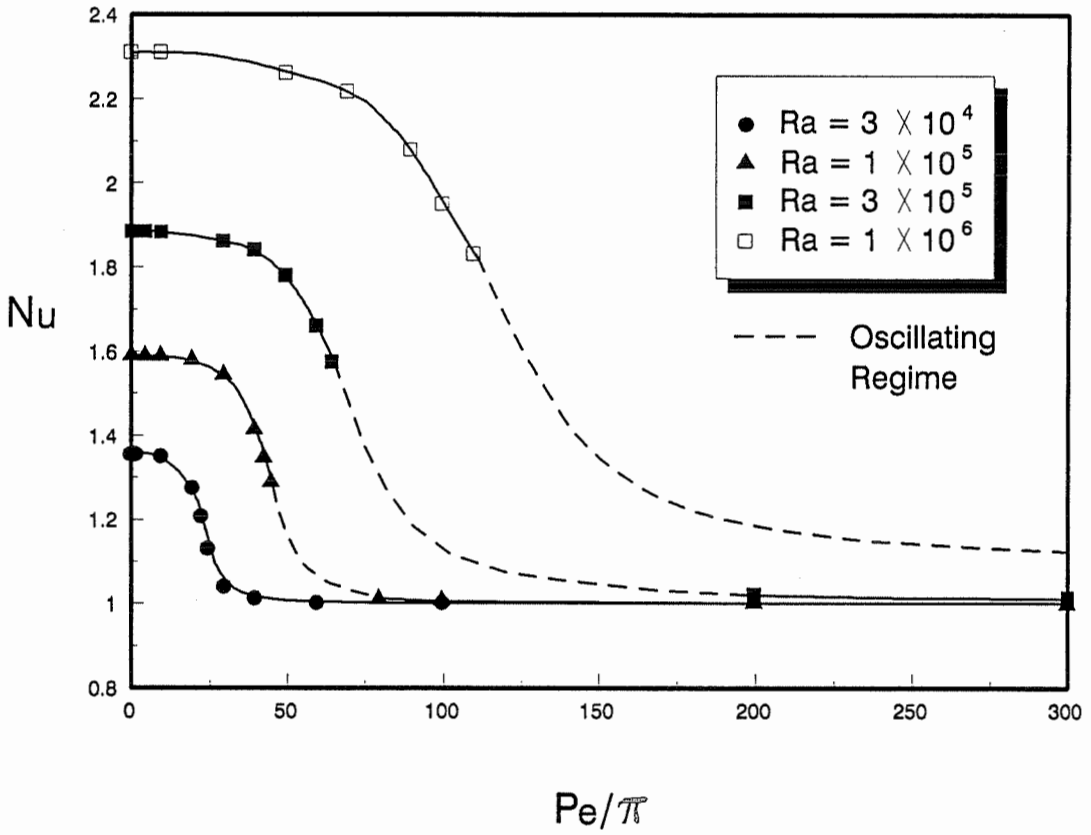

Figure 4.10: Nusselt number, function of Pe

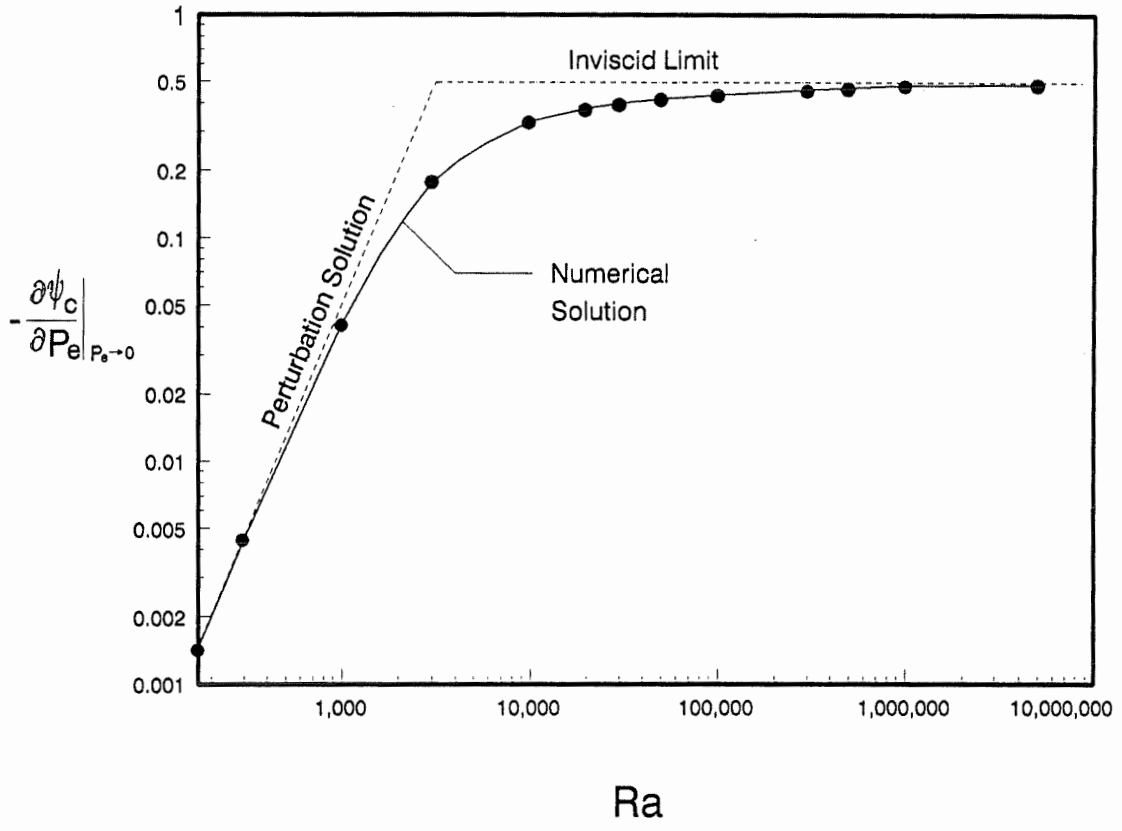

Figure 4.11: $-\partial\psi_c/\partial Pe|_{Pe\to 0}$, function of Ra, $(Pr = 1)$

Chapter 5

NATURAL CONVECTION IN A FAST ROTATION CYLINDER

This chapter is devoted to the case of a fast rotating cylinder for which the terrestrial gravity is considered negligible by comparison to the centrifugal force. A uniform temperature is imposed on the circular boundary and a heat sink is uniformly distributed within the flow domain. Under such conditions, the direction of the pure conduction density gradient is toward the geometric center whereas the centrifugal force acting on the fluid is on the opposite direction. This configuration is potentially unstable and Bénard type cells are expected to occur beyond a given threshold.

The case of a fast rotating cylinder filled with a fluid has already been studied by Ladeinde and Torrance [29]. Results from their stability analysis indicate that at incipient convection, the flow field consists of two symmetric cells. Their study included also numerical results for finite amplitude convection.

The present chapter concerns exclusively the saturated porous medium and is divided into two parts. The first part deals with the isotropic case and the last part, with the anisotropic case.

The investigation is done analytically and numerically and results from both approaches are compared.

5.1 ISOTROPIC POROUS MEDIUM

5.1.1 Mathematical Formulation

Governing equations (2.38), (2.40) and (2.39) in rotating coordinate system are considered together with boundary conditions of Eqs. (2.46) and (2.47). In Eq. (2.40) the source term arising from terrestrial gravity is dropped.

Convection can be initiated only when the Rayleigh number Ra (from now on for this chapter the subscript "Ω" is dropped) is higher than the critical value, i.e., when the buoyancy force is strong enough to overcome the viscous force in the system. To determine this criterion for the onset of convection, a linear stability analysis (both analytical and numerical) and a numerical simulation will be performed.

5.1.2 Methods of Solution

(a) Linear Stability Analysis (Analytical Approach)

The purpose of this section is to determine analytically the threshold beyond which motion will occur. The following development is straightforward.

The energy (2.39) and stream function equation (2.40) for this problem are

$$\frac{1}{r}\frac{\partial}{\partial r}(r\frac{\partial \psi}{\partial r}) + \frac{\partial^2 \psi}{r^2 \partial \theta^2} = -Ra\frac{\partial T}{\partial \theta} \tag{5.1}$$

$$\frac{1}{r}\frac{\partial}{\partial r}(r\frac{\partial T}{\partial r}) + \frac{1}{r^2}\frac{\partial^2 T}{\partial \theta^2} = \frac{\partial T}{\partial t} + u\frac{\partial T}{\partial r} + \frac{v}{r}\frac{\partial T}{\partial \theta} + 1 \tag{5.2}$$

The pure conduction temperature and stream function fields are described as

$$\psi_0 = 0 \tag{5.3}$$

$$T_0 = \frac{r^2 - 1}{4} \tag{5.4}$$

and the solution perturbed from the pure conduction state can be written in the form of

$$\psi = \psi_0 + \tilde{\psi} = \tilde{\psi} \tag{5.5}$$

$$T = T_0 + \tilde{T} = \frac{r^2 - 1}{4} + \tilde{T} \tag{5.6}$$

Substituting (5.5) and (5.6) into (5.1) and (5.2) yields

$$(\frac{1}{r}\frac{\partial}{\partial r}r\frac{\partial}{\partial r}+\frac{1}{r^2}\frac{\partial^2}{\partial\theta^2})\tilde{\psi}+Ra\frac{\partial\tilde{T}}{\partial\theta} = 0 \tag{5.7}$$

$$(\frac{1}{r}\frac{\partial}{\partial r}r\frac{\partial}{\partial r}+\frac{1}{r^2}\frac{\partial^2}{\partial\theta^2})\tilde{T}-\frac{1}{2}\frac{\partial\tilde{\psi}}{\partial\theta} = \frac{\partial\tilde{T}}{\partial t} \tag{5.8}$$

with boundary conditions

$$\begin{cases} r=1: & \tilde{\psi}=\tilde{T}=0 \\ r=0: & \tilde{\psi},\tilde{T}<\infty \end{cases} \tag{5.9}$$

Using the variables as

$$\tilde{\psi} = F(r)\,e^{pt+in\theta} \tag{5.10}$$

$$\tilde{T} = G(r)\,e^{pt+in\theta} \tag{5.11}$$

in which n is an integer related to the number of cells contained in the flow field (n=(number of cells)/2). Substituting (5.10) and (5.11) in Eqs. (5.7) and (5.8) yields

$$\frac{1}{r}\frac{\partial}{\partial r}(r\frac{\partial F}{\partial r})-\frac{n^2}{r^2}F=-inRa\,G \tag{5.12}$$

$$\frac{1}{r}\frac{\partial}{\partial r}(r\frac{\partial G}{\partial r})-\frac{n^2}{r^2}G-\frac{in}{2}F=p\,G \tag{5.13}$$

Assuming that the exchange of stability satisfied: (i.e. p is real), that $p=0$ for neutral stability and defining the operator

$$L=\frac{1}{r}\frac{\partial}{\partial r}r\frac{\partial}{\partial r}-\frac{n^2}{r^2} \tag{5.14}$$

Eqs. (5.12) and (5.13) are written as

$$LF+inRa\,G = 0 \tag{5.15}$$

$$LG-i\frac{n}{2}F = 0 \tag{5.16}$$

with boundary conditions

$$F(1) = G(1) = 0 \tag{5.17}$$

F or G may be eliminated from equations (5.15) and (5.16) to yield

$$L^2 G - \frac{n^2}{2} Ra\, G = 0 \tag{5.18}$$

or equivalently

$$L^2 F - \frac{n^2}{2} Ra\, F = 0 \tag{5.19}$$

Let us consider for (5.18) a solution of the form

$$G = G_0\, J_n(\lambda^{\frac{1}{2}} r) \tag{5.20}$$

where J_n is the Bessel function of the first kind. Applying the operation L to (5.20) gives the following sequence

$$LG = -\lambda G \tag{5.21}$$

$$LG^2 = \lambda^2 G \tag{5.22}$$

$$LG^3 = \lambda^3 G \tag{5.23}$$

$$\vdots$$

$J_n(\lambda^{\frac{1}{2}})$ may be set to zero for particular values of λ so that the boundary conditions (5.17) may be satisfied. Replacing G by its expression (5.21) in the equation (5.18) gives

$$\lambda^2 - \frac{n^2}{2} Ra = 0 \tag{5.24}$$

or

$$Ra = 2\,\frac{\lambda^2}{n^2} \tag{5.25}$$

The lowest value of λ taken from [55] for a given n is given in the following table, which satisfies (5.17) and the corresponding Ra_c

Table 5.1. Critical Rayleigh number obtained from analytical approach

n	$\lambda^{\frac{1}{2}}$	λ	Ra	Number of Cells
1	3.8317	14.6819	431.12	2
2	5.1356	26.3746	347.81	4
3	6.3801	40.7061	368.22	6
4	7.5883	57.5826	414.47	8

The 4-cell pattern corresponds to the lowest Ra. This should be the first convective pattern to occur when Ra is increased from zero. Thus the saturated porous medium differs from the fluid medium where the 2-cell pattern has the lowest threshold (Ladeinde and Torrance [29]).

(b) Linear Stability Analysis (Numerical Approach)

The linear stability analysis may also be solved through a numerical method. Equations (5.7), (5.8) and (5.9) in steady state ($\partial\tilde{T}/\partial t = 0$) define a eigenvalue problem. A finite-difference method is used to solve this eigenvalue problem. Arranging the discretized stream function and temperature in two N-component vectors $\mathbf{\Psi}$ and $\mathbf{\Theta}$, respectively, the discretized eigenvalue equations can be written out under the forms

$$A\mathbf{\Psi} + RaB\mathbf{\Theta} = 0 \tag{5.26}$$

$$C\mathbf{\Theta} + D\mathbf{\Psi} = 0 \tag{5.27}$$

where A, B, C and D are matrices $N \times N$ and with

$$N = (N_r - 1) \times N_\theta + 1 \tag{5.28}$$

N_r and N_θ are the grid numbers used in the radial and azimuthal directions, respectively.

The equations (5.26) and (5.27) may be reduced to the following canonical eigenvalue problem

$$(\lambda I - E)\mathbf{\Psi} = 0 \tag{5.29}$$

where I is the unit $N \times N$ matrix and

$$E = A^{-1}BC^{-1}D \tag{5.30}$$

$$\lambda = \frac{1}{Ra} \tag{5.31}$$

If

$$\lambda_1 \geq \lambda_2 \geq \cdots \geq \lambda_N \tag{5.32}$$

are eigenvalues of equations (5.29), then

$$Ra_{c1} = \frac{1}{\lambda_1} \tag{5.33}$$

Equation (5.29) may be solved easily by a standard computer software. Double roots are obtained ($\lambda_1 = \lambda_2, \lambda_3 = \lambda_4$, etc.) and corresponding Ra_c are deduced from Eq. (5.31). The associated eigen vector Ψ_i represents the corresponding flow patterns. It is seen in Table 5.2 that the precision of the critical value in Ra depends on the grid numbers N_r and N_θ and that the value with the mesh size of 14×100 agrees to the one from the analytical solution within 0.42% for Ra_{c1} and within 0.5% for Ra_{c2} with a mesh size of 25×105.

Table 5.2. Critical Rayleigh numbers from linear stability analysis

Mesh size	Ra_{c1}(4-cell)	Ra_{c2}(6-cell)
12×24	368.0	422.0
14×33	357.0	394.0
14×50	350.5	377.4
15×60	349.26	374.01
14×100	346.36	
25×105		370.06
27×108		
Analytical results	347.81	368.22

The flow patterns corresponding to different pairs of cells, i.e., to different thresholds are given in Fig. 5.1, where the mesh size used is 15×50. The purpose of these figures is to illustrate the type of flow pattern corresponding to different λ_i. The actual mesh size obviously does not provide a great accuracy in the determination of the threshold (critical Rayleigh). Each pair of eigenvalues generates two flow patterns, equivalent, but out of phase by $\pi/2n$. From those results, it appears that multiple finite amplitude solutions are theoretically possible at a given Ra number well above the first threshold ($Ra_{c1} \approx 348$).

(c) Numerical Approach For Finite Amplitude Convection

For Rayleigh numbers higher than the critical value, a numerical program has been developed to simulate the finite amplitude convection. Finite difference tech-

niques with regular mesh sizes of 18×36 are used to discretize the entire cylinder. The details of finite difference techniques used for the study can be found in chapter 3.

In order to test the stability and existence of multiple cell steady state solutions, initial conditions with flow fields containing various numbers of cells were used throughout the investigation of the finite amplitude convection.

5.1.3 Results and Discussion

Firstly it was found that for $Ra < Ra_{c1} \approx 348$, tests with the finite amplitude numerical program involving various initial conditions always ended up to the pure conduction solution. At $Ra = 360$, only a 4-cell structure pattern was found to occur at steady state, in agreement with the established first two thresholds of Table 5.1 ($Ra_{c1} \approx 348$ and $Ra_{c2} \approx 368$). However it was possible to obtain two different steady state flow regimes at $Ra \geq 400$, consistently with the thresholds tested in Table 5.1. Figure 5.2$a, b, c,$ and d shows flow and temperature fields (at left and right respectively) obtained numerically for two different Rayleigh numbers ($Ra = 600, 1000$). The symmetry of convective cells with respect to the vertical diameter of the cylinder is only for convenience of demonstration, not physically imposed. As a matter of fact there is no preferred position in the θ-direction for the isotropic case. Figure 5.2a, b and Figure 5.2c, d illustrate the fact that multiple solutions, containing different numbers of cells, are possible at a given Ra well above the first threshold $Ra_{c1} \approx 348$.

Fluid motion and heat transfer characteristics such as T_c (the temperature at the center), $\psi_{\max}$ (maximum stream function) and $Nu = T_{av}|_{\text{pure conduction}}/T_{av}$ (Nusselt number) are shown as function of Ra in Figs. 5.3, 5.4 and 5.5 respectively. Among those figures, T_c=0.25, Nu=1 and $\psi_{\max}$=0 represent the state associated with the pure conduction solution. The critical Rayleigh number at the onset of

convection, Ra_{c1}, as inferred from Figs. 5.3, 5.4 and 5.5 is within 3% of the values obtained by the linear stability analysis approach. It is seen in those figures that each curve (which corresponds to a given number of cells) has a limited range. A pure conduction where no convection takes place ($\bar{T}_c = 0.25, Nu = 1, \psi_{\max} = 0$) is maintained until Ra reaches the critical Rayleigh number Ra_{c1}. Consistent with the analytical solution and linear stability analysis, a 4-cell flow (wavenumber 2) is first observed at the onset of motion, when Ra is increased from zero. No matter what kind of initial flow condition is imposed, as predicted in the analytical solution and linear stability analysis, only 4-cell pattern is maintained for the range $Ra_{c1} \leq Ra \leq Ra_{c2}$. Both 4-cell and 6-cell patterns can be obtained for a part of the range $Ra_{c2} \leq Ra \leq Ra_{c3}$, provided that the initial condition contains the appropriate numbers of cells. As already mentioned, multiple solutions for the problem are therefore possible for high enough Ra. It was found numerically impossible to maintain the 4-cell structure when Ra exceeded the value of 700, beyond which the flow evolves always to a 6-cell pattern. In a comparable way, a 6-cell structure will shift to 8-cell as $Ra > 1030$.

It is observed in Figs. 5.3 and 5.4 that the fluid is more vigorously mixed with increasing Ra, leading to higher values of $\psi_{\max}$ and lower values of T_c. The decrease of T_c is accompanied by stronger temperature gradients on the cylinder boundary, which produces higher value of Nu, as observed in Fig. 5.5.

It is noticed in Figs. 5.4 and 5.5 that the value of $\psi_{\max}$ for the 6-cell pattern is smaller than for the 4-cell pattern at a given Ra. The behavior of Nu is more complex. Finally it should be recalled that a stable solution at higher Ra number requires more cells.

In short, the major findings are the following.

1) The configuration investigated is potentially unstable and Bénard cells are

found to occur when the critical Rayleigh number is above a threshold of 348 corresponding to the onset of motion.

2) Only 4-cell structure flow occurs at the incipient convection. Furthermore it is possible to obtain multiple solutions when $Ra \gg\sim 348$. Each of the patterns can be maintained for a wide range of Rayleigh numbers.

3) Heat transfer increases with the Ra increasing.

4) A stable solution at high Ra numbers will require more cells.

5.2 ANISOTROPIC POROUS MEDIUM

The behavior of an anisotropic Darcy porous medium within a horizontal circular cylinder rotating at high angular velocity is investigated analytically and numerically. Conditions are the same as those described for the isotropic case. Here again, the configuration is potentially unstable and gives rise to Bénard cells beyond a critical Rayleigh number.

5.2.1 Mathematical Formulation

The circular cylinder of infinite extent shown in Fig. 2.2*a* is filled with an anisotropic porous medium. In this figure K_1 and K_2 are the extreme permeabilities along to the principal axes of the anisotropic medium, and θ_k is the angle between the origin and the principal axis corresponding to K_2. As usual it is assumed that the Boussinesq approximation holds and that all fluid and solid properties are constant except for the density in the buoyancy term. By neglecting the terrestrial gravity force, Eqs. (2.38), (2.36) and (2.39) are the governing equations for the problem with boundary conditions given by Eqs. (2.46) and (2.47).

Here also the convective motion can be initiated only when the Ra is higher than a critical value, i.e., when the buoyancy force is strong enough to overcome the

viscous forces in the system. To determine this criterion for the onset of convection, a linear stability analysis is performed.

5.2.2 Linear Stability Analysis

The linear stability analysis is done exclusively with the help of a numerical method. The distribution of temperature and stream function for pure conduction is described as

$$\psi_0 = 0 \tag{5.34}$$

$$T_0 = \frac{r^2-1}{4} \tag{5.35}$$

and the solution perturbed from the pure conduction state can be written in the form of

$$\psi = \psi_0 + \tilde{\psi} = \tilde{\psi} \tag{5.36}$$

$$T = T_0 + \tilde{T} = \frac{r^2-1}{4} + \tilde{T} \tag{5.37}$$

Substituting (5.36) and (5.37) into (2.36) to (2.39) yields

$$\{R_{rr}\frac{\partial^2}{r^2\partial\theta^2} - 2R_{r\theta}\frac{\partial^2}{r\partial r\partial\theta} + R_{\theta\theta}\frac{1}{r}\frac{\partial}{\partial r}(r\frac{\partial}{\partial r}) + \frac{1-R}{r}[-\sin 2(\theta-\theta_k)\frac{\partial}{r\partial\theta} + \cos 2(\theta-\theta_k)\frac{\partial}{\partial r}]\}\tilde{\psi} + Ra\frac{\partial}{\partial\theta}\tilde{T} = 0 \tag{5.38}$$

$$(\frac{1}{r}\frac{\partial}{\partial r}r\frac{\partial}{\partial r} + \frac{1}{r^2}\frac{\partial^2}{\partial\theta^2})\tilde{T} - \frac{1}{2}\frac{\partial\tilde{\psi}}{\partial\theta} = 0 \tag{5.39}$$

together with boundary conditions

$$\begin{cases} r=1: & \tilde{\psi} = \tilde{T} = 0 \\ r=0: & \tilde{\psi},\ \tilde{T} < \infty \end{cases} \tag{5.40}$$

From now on, the same procedure as was employed for the isotropic case is applied, i.e., Eqs. (5.26) to (5.33) are also valid for this anisotropic case with matrices based on Eqs. (5.38) and (5.39).

Here again, Eq. (5.29) may be solved easily by a standard computer software.

5.2.3 Results and Discussion

The present section is restricted to the linear stability analysis and does not involve results from the finite amplitude numerical program. As opposed to the isotropic case there are no more double roots for the eigenvalues λ_i. Results from the linear stability analysis are shown in Figs. 5.6, 5.7, 5.8 and 5.9. In Figs. 5.6, 5.7 and 5.8, 4-cell, 6-cell and 2-cell flow pattern have been reproduced, respectively, based on the eigen vector $\mathbf{\Psi}$. It can be found that in those figures that the perpendicular line segments are placed at the center of cylinder to indicate the orientations of two extremum permeabilities and their ratio. This will apply to all flow and temperature patterns for the anisotropic cases in this thesis. For the anisotropic case the flow configuration occupies a specific position in the θ direction for which a symmetry exists with respect to the principal axes. Figure 5.9 gives Ra_c as a function of R on a semi-log graph, which produces a symmetry in results together with the particular definition of Ra for anisotropic porous medium in this thesis. Only the range $0.2 \leq R \leq 5$ is represented in this figure and the 8-cell flow configuration has been omitted for clearity. It may be first noticed that the values of Ra_c at $R = 1$ correspond to those of Table 5.1. Furthermore, it may be observed that with R departing from unity each flow configuration separates in two distinct branches. For the 2-cell configuration, one of the principal axes acts as a separating line between the cells, the other crossing the centers of the two cells. This creates two possibilities on each side of $R = 1$, according to the directions of maximum and minimum permeabilities. Figure 5.8 illustrates those two different types of flow configurations for various R below unity. Of course, the same counterpart exists for R larger than unity and the use of a logarithmic scale for R produces the symmetry with respect to the vertical line $R = 1$ observed for the curves. For the case of the 4-cell pattern there exist also two possibilities for symmetric flow configurations: as observed in

Figure 5.6, the principal axes may correspond to the separating lines between the cells or they may cross the centers of the cells. Cosequently for R far from unity two distinct flow configurations containing four cells do exist on each side of $R = 1$. With the 6-cell configuration one of the axes serves as a separating line between adjacent cells and the other crosses the centers of the two remaining cells. As for the 2-cell configurations, this situation provides two possibilities, according to the directions of maximum and minimum permeabilities.

As a conclusion, all these incipient flow configurations imply that multiple finite amplitude solutions are likely to exist, each one having its own heat transfer characteristics and value of Nusselt number. In particular, at a R departing largely from unity (for instance, at $R = 4$) it is seen in Fig. 5.9 that first threshold encountered is below the isotropic one ($Ra \approx 348$) and that the first flow configuration to appear contains six cells. Moreover the modification in the relative values of the various thresholds encountered with the increase or decrease of R from unity is expected to modify the range of each flow configuration shown in Figs. 5.3, 5.4 and 5.5, and would lead to entirely new graphs.

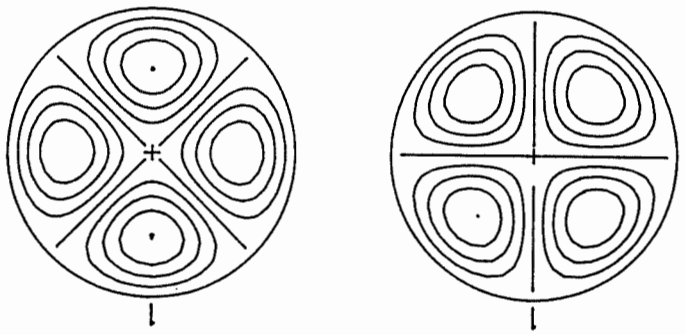

(*a*) $Ra_c = 350.5$, 4-cell structure

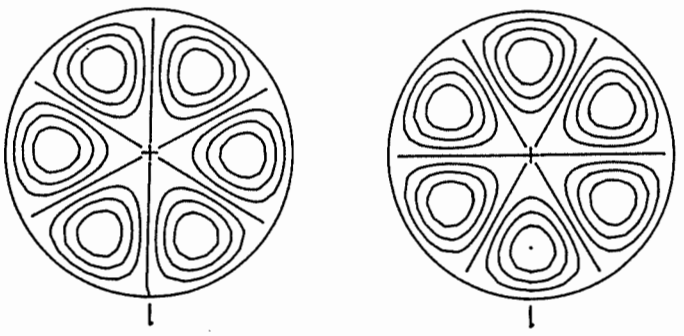

(*b*) $Ra_c = 377.4$, 6-cell structure

Figure 5.1: Flow patterns (Linear stability analysis)
(Mesh size: $N_r = 15; N_\theta = 50$)

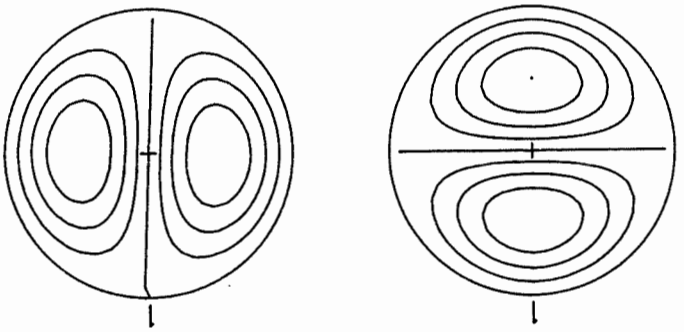

(*c*) $Ra_c = 430.0$, 2-cell structure

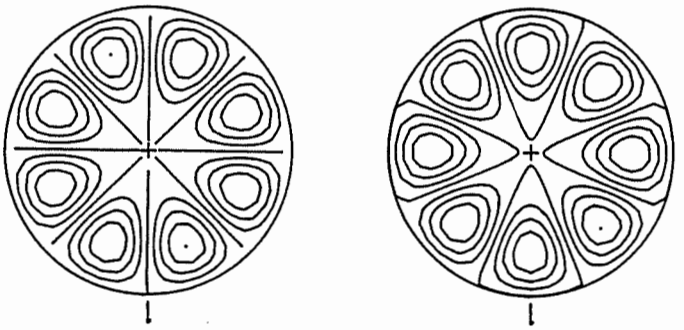

(*d*) $Ra_c = 434.9$, 8-cell structure

Figure 5.1 (*continued*)

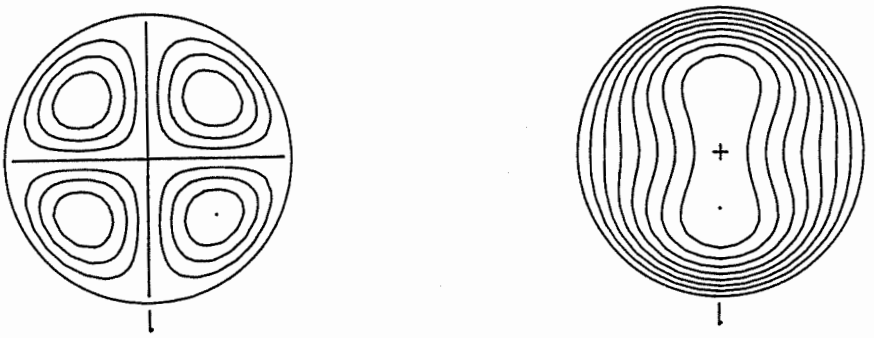

(*a*) $Ra = 600$, 4-cell structure

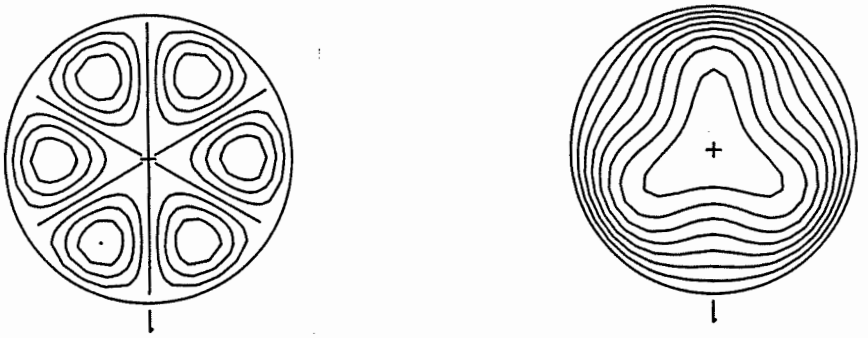

(*b*) $Ra = 600$, 6-cell structure

Figure 5.2: Flow patterns (Finite amplitude convection)

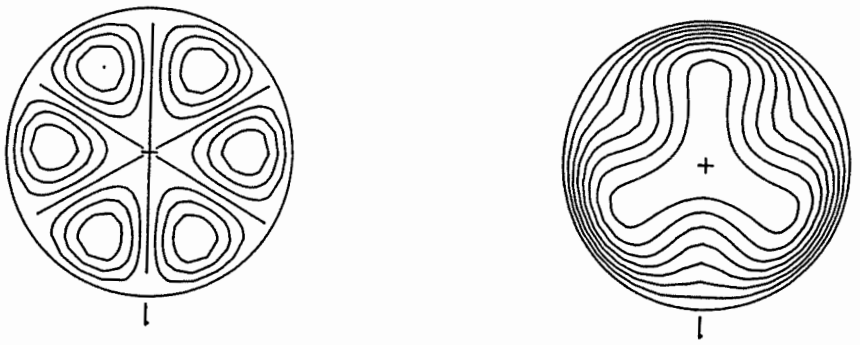

(*c*) $Ra = 1000$, 6-cell structure

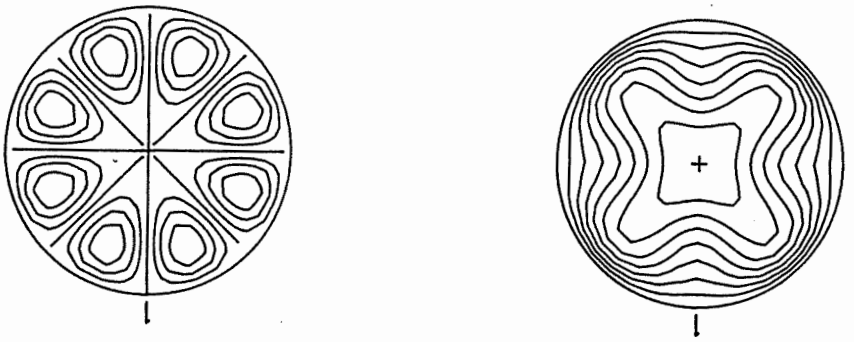

(*d*) $Ra = 1000$, 8-cell structure

Figure 5.2 (*continued*)

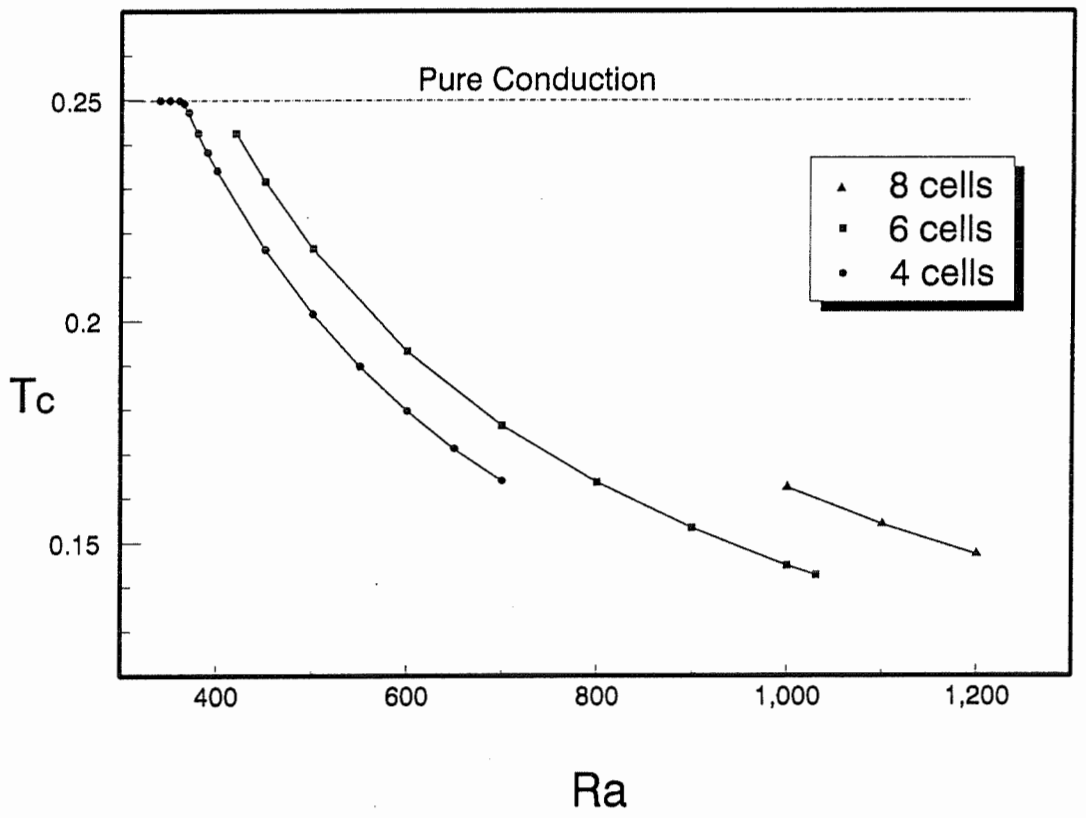

Figure 5.3: T_c, function of Ra

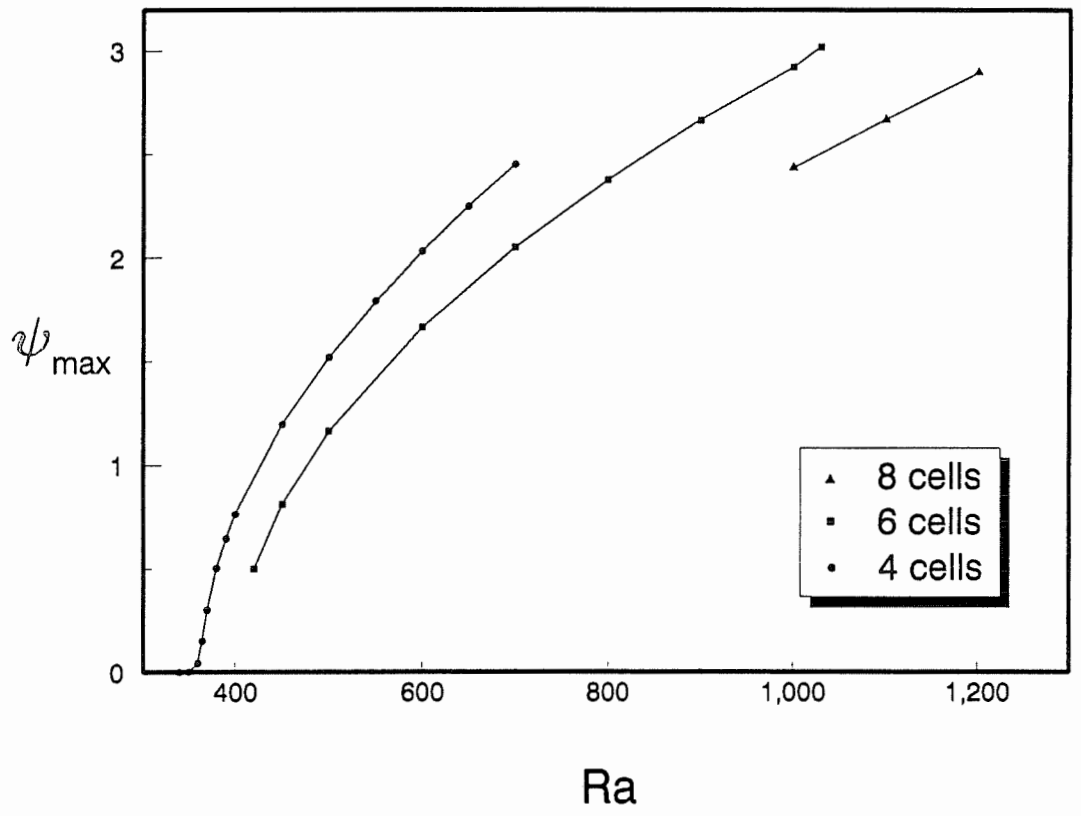

Figure 5.4: $\psi_{\mathbf{max}}$, function of Ra

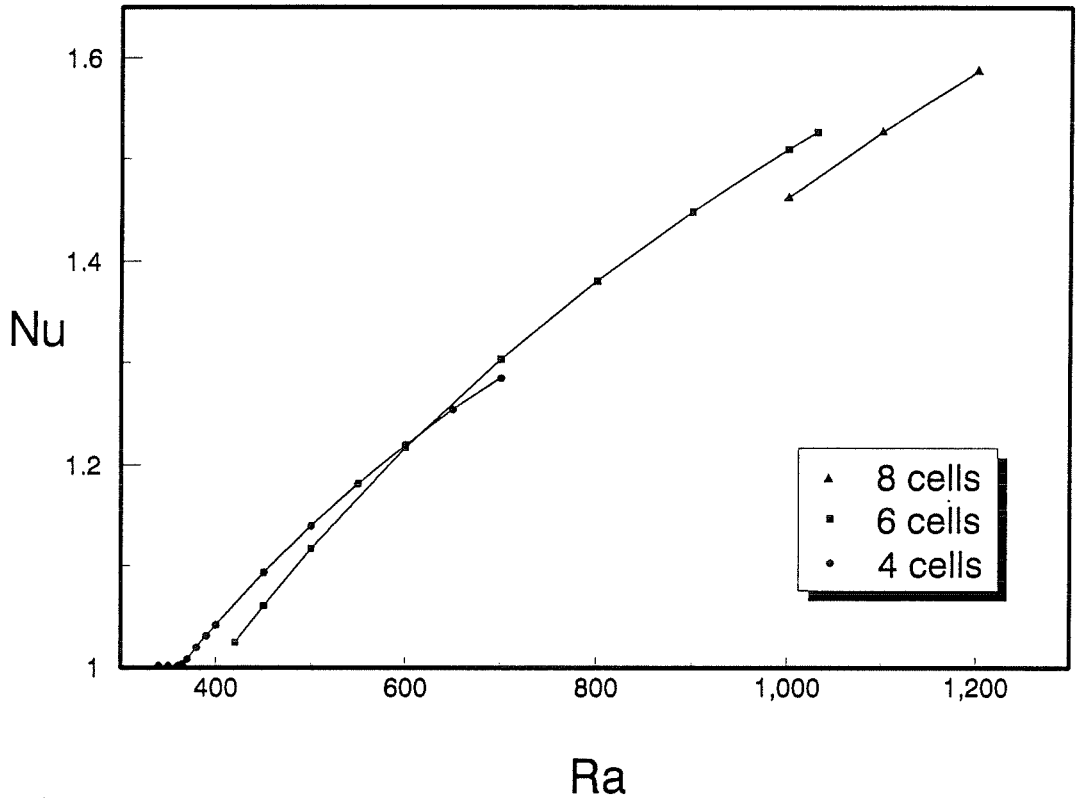

Figure 5.5: Nu, function of Ra

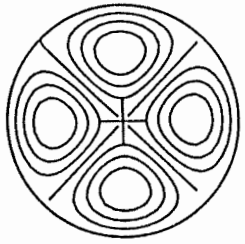

$Ra_c = 349.7778$

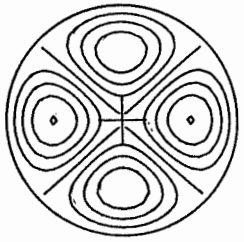

$Ra_c = 349.7228$

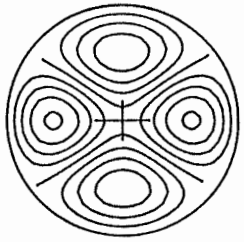

$Ra_c = 348.8097$

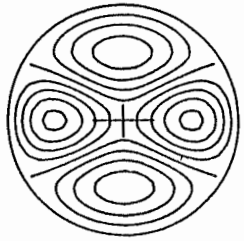

$Ra_c = 347.0700$

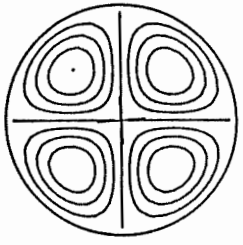

$Ra_c = 349.7978$

$R = 1$

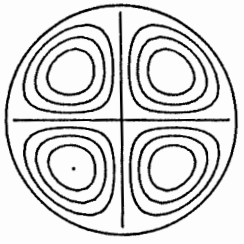

$Ra_c = 350.0534$

$R = 0.91$

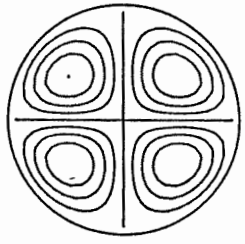

$Ra_c = 353.1967$

$R = 0.7$

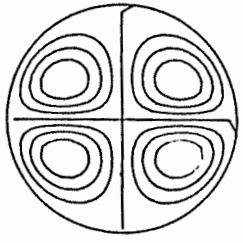

$Ra_c = 362.1700$

$R = 0.5$

Figure 5.6: Flow patterns (4-cell structure)

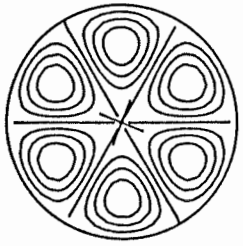

$Ra_c = 375.3058$

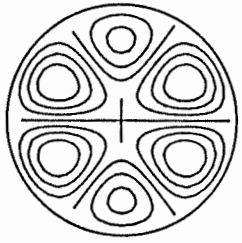

$Ra_c = 374.3359$

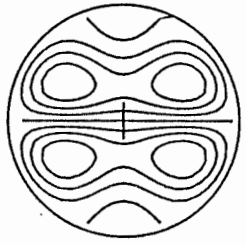

$Ra_c = 366.2084$

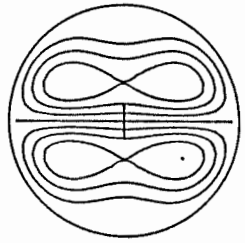

$Ra_c = 358.1100$

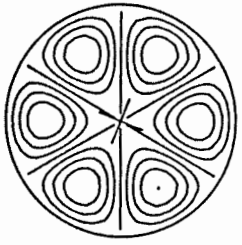

$Ra_c = 375.3146$

$R = 1$

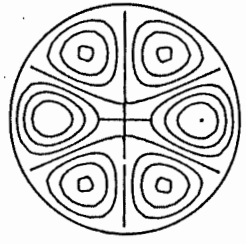

$Ra_c = 375.2099$

$R = 0.8$

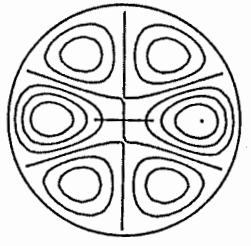

$Ra_c = 376.1086$

$R = 0.6$

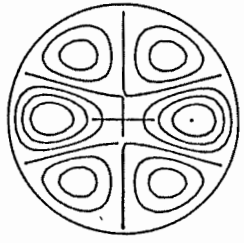

$Ra_c = 378.0200$

$R = 0.5$

Figure 5.7: Flow patterns (6-cell structure)

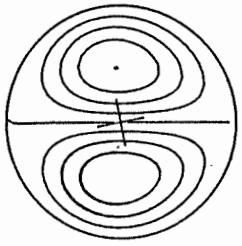

$Ra_c = 430.1448$

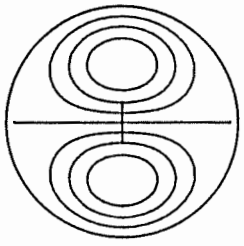

$Ra_c = 410.1453$

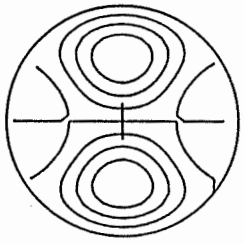

$Ra_c = 398.7838$

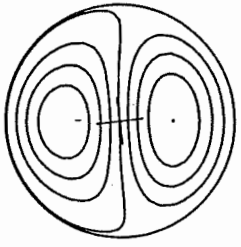

$Ra_c = 430.1703$

$R = 1$

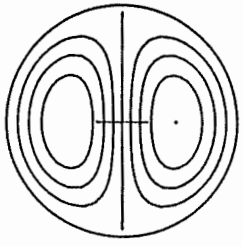

$Ra_c = 457.4589$

$R = 0.8$

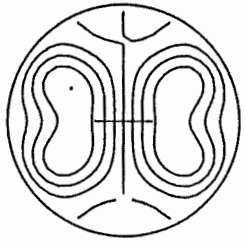

$Ra_c = 499.9722$

$R = 0.6$

Figure 5.8: Flow patterns (2-cell structure)

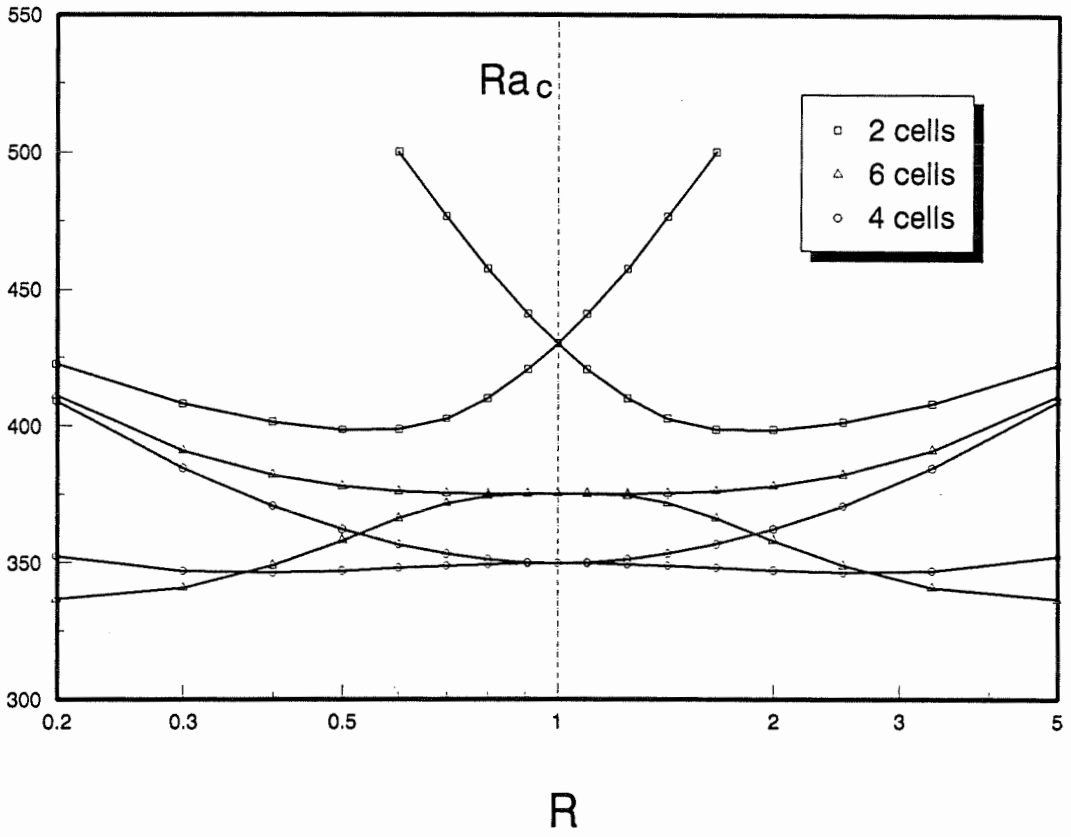

Figure 5.9: Ra_c, function of R

Chapter 6

INSTABILITY IN A NON-ROTATING CYLINDER

When a non-rotating circular cylinder filled with either a fluid or a fluid saturated porous medium is subject to a non-uniform heating, natural convection takes place in the presence of terrestrial gravity. A simple form of non-uniform heating is the case of a cosinoidal temperature distribution imposed on the boundary, which is equivalent to a linear thermal stratification of the surroundings in a given direction. In particular, when the temperature gradient is in the downward direction (bottom heating) a potentially unstable situation occurs with the presence of a pure conduction temperature field inside the cylinder and motion is expected beyond a threshold corresponding to a critical value for the Rayleigh number. Weinbaum [38] has considered analytically the fluid filled cylinder, for various inclinations of the stratification, including the bottom heating. All cases were characterized by a single cell convective flow pattern. The threshold value for bottom heating was established analytically and corresponds to $Ra_c \approx 576$. The case of a cylinder filled with a isotropic porous medium was considered by Storesletten and Tveitereid [56]. Their work was purely analytical and dealt with side heating and bottom heating. For the bottom heating, they found a critical Rayleigh of 23.13 with two types of incipient flow patterns consisting of two and three cells respectively, both structures being stable.

In this chapter the saturated porous medium is considered exclusively. We apply the linear stability analysis used in Chapter 5 to reconfirm the results of Storesletten and Tveitereid [56] at incipient convection for isotropic case and to establish thresholds for the anisotropic case. Furthermore the finite amplitude nu-

merical code is used to study in more detail the behavior of natural convection for Rayleigh numbers well above the established thresholds.

The whole chapter is divided in two parts, devoted respectively to the isotropic and anisotropic cases.

6.1 ISOTROPIC POROUS MEDIUM

The behavior of a saturated porous medium within a non-rotating horizontal cylinder with non-uniform heating is investigated in this section. The boundary is subject to a thermal stratification of arbitrary inclination with respect to the gravity. For bottom heating, the pure conduction temperature gradient is in the downward direction. This is a potentially unstable configuration, and motion occurs only when the Darcy-Rayleigh number is beyond a critical value. For bottom heating, a linear stability analysis is performed in order to establish the threshold value and the convective pattern at incipient convection. This multi-cell pattern may be predicted from considerations involving the hydrodynamic circulation on the boundary. Additional results are sought to obtain the flow and temperature fields and heat transfer characteristics at finite amplitude convection, for Darcy-Rayleigh numbers covering the range from 0 to 200 and for various inclinations of the thermal stratification imposed on the boundary.

6.1.1 Mathematical Formulation

The boundary of the horizontal cylinder shown in Fig. 6.1 is subject to an imposed non-uniform temperature of the form

$$T'\big|_{r'=r'_0} = T'_0 + \Delta T' \cos(\theta - \theta_0) \tag{6.1}$$

As mentioned in section 2.3.2 of the thesis, in this kind of boundary temperature condition the reference temperature T'_0 is an average value of the boundary temperature distribution and the characteristic temperature $\Delta T'$ stands for the amplitude

of the cosine temperature imposed on the boundary. The extremum temperatures on the boundary occur at the opposite ends of a diameter at angle θ_0 with the gravity. It is again assumed that the Boussinesq approximation holds and that all fluid and solid properties are constant except for the density in the buoyancy term. The governing eqations are Eqs. (2.38), (2.39) and (2.40) with the exception that the Rayleigh numbers based on the centrifugal force in (2.40) and that the heat sink term S' in (2.39) are set to zero. Boundary conditions are

$$r = 1: \quad \psi = \frac{\partial \psi}{\partial \theta} = 0, \quad T = \cos(\theta - \theta_0) \tag{6.2}$$

One useful relationship is obtained by introducing the hydrodynamic circulation Γ and by evaluating its value from Eq. (2.34*b*)

$$\frac{\Gamma}{r} = \int_0^{2\pi} u_\theta \, d\theta = Ra \int_0^{2\pi} T \sin\theta d\theta \tag{6.3}$$

The value of Γ on the boundary is found to be $\pi Ra \sin\theta_0$.

A motionless equilibrium is possible at $\theta_0 = 0, \pi$. For $\theta_0 = 0$ (bottom heating), the configuration is unstable since the density gradient is positive upward. In other words, there exists a threshold in Ra beyond which disturbances are amplified. A particularity of a Darcy porous medium, as opposed to a fluid medium, lies in the fact that a non-zero tangential velocity exists at the boundary. Thus for the unstable configuration ($\theta_0 = 0$), $\Gamma = 0$ means that a flow reversal must occur near the boundary, i.e., with a non-zero azimuthal velocity on the boundary, a single cell pattern does not exist, even at incipient convection.

6.1.2 Methods of Solution

(a) Regular Perturbation Method for $\theta_0 \neq 0, \pi$

For all cases where $\theta_0 \neq 0, \pi$, a fluid motion always occurs when $Ra > 0$. A regular perturbation approach, valid at low Ra, may be used to solve analytically

the steady state form of Eqs. (2.40) and (2.39). Expanding T and ψ in powers of Ra, according to

$$T = \sum_{n=0}^{\infty} Ra^n T_n$$

$$\psi = \sum_{n=0}^{\infty} Ra^n \psi_n$$

and replacing in (2.40) and (2.39), the following expressions are easily obtained

$$\begin{aligned} T_0 &= r\cos(\theta-\theta_0) \\ T_1 &= \frac{\sin\theta_0}{16}(r-r^3)\sin(\theta-\theta_0) \\ T_2 &= \sin\theta_0[\frac{(2r-3r^3+r^5)}{768}\sin(\theta-2\theta_0)+ \\ &\quad \frac{(r^3-r^5)}{3072}\sin(3\theta-2\theta_0)+\frac{(r-2r^3+r^5)}{1536}\sin\theta] \end{aligned} \tag{6.4}$$

$$\begin{aligned} \psi_0 &= 0 \\ \psi_1 &= \frac{\sin\theta_0}{4}(1-r^2) \\ \psi_2 &= \frac{\sin 2\theta_0}{256}(1-2r^2+r^4)+\frac{\sin\theta_0}{192}(r^2-r^4)\cos(2\theta-\theta_0) \end{aligned} \tag{6.5}$$

(b) Linear stability analysis for $\theta_0 = 0$

For bottom heating ($\theta_0 = 0$), a linear stability analysis was performed numerically by X. Zhang et al. [57] in order to determine the critical Rayleigh number (Ra_c). Assuming that $\tilde{\psi}$=ψ and $\tilde{T} = T - r\cos\theta$ are the perturbed stream function and temperature fields from the pure conduction state, the linearized equations of (2.40) and (2.39) can be written as

$$\nabla^2\tilde{\psi} + Ra\,(\sin\theta\frac{\partial}{\partial r}+\frac{\cos\theta}{r}\frac{\partial}{\partial\theta})\tilde{T} = 0 \tag{6.6}$$

$$\nabla^2\tilde{T} - (\sin\theta\frac{\partial}{\partial r}+\frac{\cos\theta}{r}\frac{\partial}{\partial\theta})\tilde{\psi} = 0 \tag{6.7}$$

together with boundary conditions

$$r = 1: \qquad \tilde{T} = 0, \ \tilde{\psi} = 0 \tag{6.8}$$

The linear stability analysis amounts to the determination of the minimum eigenvalue Ra of the homogeneous Eqs. (6.6) and (6.7) under the homogeneous boundary conditions (6.8). The approach follows quite closely the one described in section 5.1 through Eqs. (5.26) to (5.33) and will be omitted here.

Here again,

$$Ra_c = \frac{1}{\lambda_1} \tag{6.9}$$

is the critical Rayleigh number and the eigenvector $\mathbf{\Psi}_1$ corresponding to λ_1 represents the flow pattern at the onset of convection. As already mentioned, the precision of the critical Rayleigh number depends on the grid numbers N_r and N_θ. A grid of 14×33 was used. This grid size was adopted after mesh refinement tests had indicated that the result was affected less than 1%.

From the linearized equations (6.6) and (6.7), it can be proved that if $\mathbf{\Psi}_0$, $\mathbf{\Theta}_0$ is a solution at a given Ra, there $\mathbf{\Psi}_0 = -Ra\mathbf{\Theta}_0$, $\mathbf{\Theta}_0 = \mathbf{\Psi}_0$ is also a solution at the same Ra. This has been directly observed from the numerical analysis which shows that all eigenvalues of Equation (5.29) are double eigenvalues with two independent flow patterns at the onset of convection. The numerical results show that the critical Rayleigh number is $Ra \approx 23.3$ and the flow patterns at incipient convection are either a 2-cell or a 3-cell flow structure, as shown in Fig. 6.2*a* and *b*. Those results are in agreement with those of Storesletten and Tveitereid [56]. The multi-cell flow pattern contrasts with the single-cell configuration obtained by Weinbaum [38] for the fluid medium. As mentioned earlier, the multi-cell flow was expected from the constraint $\Gamma = 0$ on the boundary in the case of a Darcy porous medium.

It should be noted that Equations (6.6) and (6.7) are invariant under the transformations

$$\begin{aligned}(r, \theta, \tilde{\Psi}, \tilde{T}) &\rightarrow (r, \theta + \pi, \tilde{\Psi}, -\tilde{T}) \\ (r, \theta, \tilde{\Psi}, \tilde{T}) &\rightarrow (r, -\theta, -\tilde{\Psi}, \tilde{T})\end{aligned} \tag{6.10}$$

so that four distinct solutions exist theoretically, i.e., the increment between streamlines in Fig. 6.2a, b may be positive or negative. The temperature averaged over the domain is zero for this configuration.

(c) Numerical approach

At low Rayleigh numbers, Equations (6.4) and (6.5) may be used to obtain approximations of the flow and temperature fields for cases where $\theta_0 \neq 0$. Otherwise a numerical solution is required.

6.1.3 Results and discussion

A comparison is done in Fig. 6.3 between the values of the stream function at the center (ψ_c) obtained numerically for different heating phase angles θ_0 and the analytical curve from equations (6.5). A low value of the Rayleigh number was chosen (Ra=5) for which the second order analytical solution is valid.

The numerical results cover the range $0 \leq Ra \leq 200$ and $0^0 \leq \theta_0 \leq 180^0$. Fig. 6.4 and 6.5 show the steady state flow and temperature fields corresponding to bottom heating ($\theta_0 = 0$) at three different Rayleigh numbers, $Ra = 25, 40$ and $Ra = 50$. Streamlines (left) and isotherms (cneter) represent the flow and temperature fields respectively. The right column represents the perturbed temperature fields (actual temperature field minus pure conduction temperature field). These results have been obtained from zero flow and pure conduction temperature fields as initial conditions. In Fig. 6.4, the flow consists of three cells, as in Fig. 6.2b. However, with finite amplitude convection, the symmetry with respect to the vertical diameter

found in Fig. 6.2*b* is lost and the position of the two side cells is tilted.

The solutions shown in Fig. 6.4*a*, *b* and *c* are symmetric with respect to the center of the cylinder, or centro-symmetric, according to

$$\begin{aligned} \psi(r,\theta) &= \psi(r,\theta+\pi) \\ T(r,\theta) &= -T(r,\theta+\pi) \end{aligned} \tag{6.11}$$

Thus, the heat entering the cavity and the heat going out have identical distributions in θ with two extrema in opposite locations. Also, the temperature averaged over the domain remains equal to zero.

It is also possible to obtain numerically a stable steady-state flow pattern consisting of two cells such as the one predicted by the linear stability analysis (Fig. 6.2*a*). The results are shown in Fig. 6.5. Starting the computation from initial conditions that already contain a 2-cell configuration such as the one shown in Fig. 6.2*a*. With the increasing of Ra, the two original cells start to move vertically, downward if the velocity is downward on the vertical diameter as shown in Fig. 6.5. 2-cell flow patterns with an upward velocity on the vertical diameter are also possible (not shown). In the case of a 2-cell flow pattern, the temperature averaged over the domain differs from zero. For a downward velocity on the vertical diameter, the averaged temperature is below the mean temperature of the boundary. Fig. 6.6 shows how the extreme value of the stream function (ψ_{ext}) varies with Ra in the case of 2-cell and 3-cell flow patterns, at $\theta_0 = 0$. For the 3-cell flow pattern, ψ_{ext} is at the center ($\psi_{\text{ext}} = \psi_c$). For the range $0 \leq Ra \leq 23.3$, there is no flow and $\psi_{\text{ext}} = 0$. Above the threshold $Ra = 23.3$, two distinct curves exist for the two types of flow patterns. A qualitative representation of the bifurcation shown in Fig. 6.6 had already been provided by Storesletten and Tveitereid [56].

In Fig. 6.7 the extrema of the stream function obtained numerically for the

3-cell flow pattern are given as functions of Ra, for heating phase angles $\theta_0 = 0^0, 5^0, 10^0$ and 15^0. Such a perturbation on the heating phase angle is comparable to the asymmetric perturbation about the vertical diameter done by Storesletten and Tveitereid [56], which yields a 3-cell flow pattern. In this figure, ψ_c is the value of the stream function at the center and ψ_s, the other extrema characterizing the side cells. Steady states only are presented in this figure. When θ_0=0 (bottom heating), no fluid motion can exist unless $Ra > Ra_c \approx 23$. Beyond that threshold, a steady-state non-trivial solution exists. The steady-state convection covers the range $Ra_c < Ra < 93$. A Hopf bifurcation occurs at $Ra \approx 93$ beyond which the solution is characterized by strong periodic oscillations. When $\theta_0 \neq 0$, a 3-cell fluid motion always occurs for $Ra > 0$ and the steady-state cover a wider range with θ_0 increasing.

Numerical results for the 3-cell flow pattern are shown differently in Fig. 6.8 where ψ_c is given as a function of θ_0 for different values of Ra. With increasing θ_0, it is observed that the Hopf bifurcation occurs at larger Ra. For instance, steady state results corresponding to $Ra = 200$ are obtained at $\theta_0 \approx 32^0$. With increasing θ_0, the side cells are gradually reduced in size (see Fig. 6.7) until they disappear and a single-cell flow pattern, such as the one shown in Fig. 6.9 ($Ra = 80; \theta_0 = 90^0$) occurs at large heating phase angles. The dashed line in Fig. 6.8 separates the two types of flow patterns. The curves corresponding to Ra=40, 60 and 80 are above the threshold and cover the whole range $0^0 \leq \theta_0 \leq 180^0$. The extrapolating these curves in the negative θ_0 direction would correspond to "antinatural" solutions, according to Sen et al. [58], i.e., to the "isolated" branches of an unfolded supercritical bifurcation [59]. It was found impossible to obtain numerical results that would extend those curves to the left. Various attempts were made at different Ra, using the available flow and temperature fields at θ_0 =0 and choosing decrements in θ_0 as small as -0.5^0. In all cases, the flow and temperature

fields evolved toward a final steady state that was the symmetric counterpart of the initial conditions, in agreement with the invariance property (6.10). This behavior came as no surprise since Storesletten and Tveitereid [56] have predicted that "antinatural" solutions were unstable.

The finite-amplitude convection enhances the heat transfer across the cylinder. Figure 6.10 shows the local heat transfer along the boundary at Ra=25, 40 and 80 for the 3-cell flow pattern. Since the part of the boundary through which heat is entering is not fixed but varies with Ra, a measure of the heat exchange with the surroundings consists in integrating the absolute value of the local heat transfer over the whole boundary. Thus an overall Nusselt number may be defined as

$$Nu = \frac{\frac{1}{2\pi}\int_0^{2\pi}\left|\frac{\partial T}{\partial r}\right|_{r=1} d\theta}{\frac{1}{2\pi}\int_0^{2\pi}\left|\frac{\partial T_0}{\partial r}\right|_{r=1} d\theta} = \frac{1}{4}\int_0^{2\pi}\left|\frac{\partial T}{\partial r}\right|_{r=1} d\theta \qquad (6.12)$$

with $Nu = 1$ for pure conduction. This Nusselt number is given in Fig. 6.11 as a function of θ_0 for different Ra. Here again, the dashed line separates the single-cell (right) from the 3-cell flow pattern (left). For a given Ra, the maximum Nusselt number is obtained at a value of θ_0 slightly below 90^0. At θ_0=0 (bottom heating) the pure conduction heat transfer ($Nu = 1$) is maintained until Ra reaches the critical value. Then the Nusselt number starts to increase.

6.1.4 Summary

When the heat is entering from below, i.e., when the maximum temperature is at the lowest point on the boundary (bottom heating), a motionless and potentially unstable equilibrium exists. A linear stability analysis predicts that the critical Rayleigh number (Ra_c) for the onset of convection is $\approx$23.3, in agreement with Storesletten and Tveitereid [56]. Also according to the linear stability analysis, two flow configurations consisting of two and three cells are likely to occur beyond the threshold. The results for finite amplitude convection, as obtained from a numerical

code specially developed to this end, indicate that both the 3-cell and 2-cell patterns are stable configurations.

Numerical solutions were also obtained at different Rayleigh numbers for an arbitrary location of the maximum temperature on the boundary. The flow is then unicellular unless the maximum temperature lies somewhere in the neighborhood of the unstable location ($\theta_0 = 0$).

6.2 ANISOTROPIC POROUS MEDIUM

The behavior of an anisotropic porous medium is studied theoretically for conditions equivalent to those of section 6.1. The anisotropy involved concerns as usual in this work the permeability. Unlike the isotropic case, only the bottom heating $\theta_0 = 0$ is considered for the anisotropic case. A linear stability analysis is performed to investigate the criterion for the onset of convection and associated flow patterns. It is found that the flow patterns at the onset of convection are either a 2-cell or a 3-cell structure, depending on the inclination of the principal axes of the porous matrix. It is shown that both the permeability ratio and inclination of the principal axes have a strong influence on the critical value of Ra and the flow pattern at the onset of convection. A numerical code is developed to study the finite amplitude convection beyond the critical Ralyeigh number. Results are analysed in terms of the ratio of permeability and the orientation angle of the principal axes.

6.2.1 Mathematical Formulation

The problem considered is described in Fig. 6.12. In this figure K_1 and K_2 are the extreme permeabilities along to the principal axes of the anisotropic medium, with $R = K_2/K_1$ and θ_k is the angle between the gravity direction and the principal axis corresponding to K_2.

Dropping the centrifugal force term in (2.36) and the heat sink term in (2.39),

the problem can be stated as follows in dimensionless form

$$R_{rr}\frac{\partial^2\psi}{r^2\partial\theta^2} - 2R_{r\theta}\frac{\partial^2\psi}{r\partial r\partial\theta} + R_{\theta\theta}\frac{1}{r}\frac{\partial}{\partial r}(r\frac{\partial\psi}{\partial r}) + \frac{1-R}{r}[-\frac{\partial\psi}{r\partial\theta}\sin 2(\theta-\theta_k) + \frac{\partial\psi}{\partial r}\cos 2(\theta-\theta_k)] = -Ra(\frac{\partial T}{\partial r}\sin\theta + \frac{\partial T}{r\partial\theta}\cos\theta) \quad (6.13)$$

$$\frac{\partial T}{\partial t} + u\frac{\partial T}{\partial r} + \frac{v}{r}\frac{\partial T}{\partial\theta} = \frac{1}{r}\frac{\partial}{\partial r}(r\frac{\partial T}{\partial r}) + \frac{1}{r^2}\frac{\partial^2 T}{\partial\theta^2} \quad (6.14)$$

with boundary condition

$$r = 1: \quad u = 0, \quad T = \cos\theta \quad (6.15)$$

Here also, the Rayleigh number is based on gravity, $Ra = g'\beta\Delta T' r_0'\sqrt{K_1K_2}/\nu\alpha$. Under the conditions imposed to the problem, three governing parameters are involved, namely Ra, R and θ_k.

6.2.2 Methods of Solution

(a) Linear Stability Analysis

A linear stability analysis was performed numerically in a way comparable to parts 5.1, 5.2 and 6.1 in order to determine the critical Rayleigh number (Ra_c). Here the pure conduction flow and temperature fields are $\psi_0 = 0, T_0 = r\cos\theta$.

For the isotropic porous medium ($R = 1$), which was studied by Storesletten and Tveitereid [56] and by Robillard et al. [57], the critical Rayleigh number was about 23.3, and the flow pattern consisted theoretically of a 2-cell or a 3-cell structure at the onset of convection in relation with the existence of double eigenvalues at $R = 1$. However, some dramatic changes appear for an anisotropic porous medium, i.e., no double eigenvalues are obtained and the flow pattern at the onset of convection is either a 2-cell or a 3-cell structure, depending on the inclination angle θ_k. Besides the stability criterion and the corresponding flow pattern at the onset of convection which is refered to as the primary mode, the second eigenvalue and its corresponding

eigenfunction representing a priority flow is the secondary mode at supercritical Rayleigh numbers ($Ra > Ra_c$).

Noticing that R is always positive, it is observed that

$$\begin{aligned} \psi(Ra, R, \theta_k) &= \psi(Ra, R, \pi + \theta_k) \\ \psi(Ra, R, \theta_k) &= -\psi(Ra, R, -\theta_k) \end{aligned} \tag{6.16}$$

and the discussion can be limited to the range of $0 \leq \theta_k \leq 90^0$ while choosing R either larger or smaller than unity. Moreover, if R is allowed to vary from 0 to ∞, there exists

$$\psi(Ra, R, \theta_k) = -\psi(Ra, 1/R, \pi/2 - \theta_k) \tag{6.17}$$

and consequently the investigation may be limited to the range $0 \leq \theta_k \leq 45^0$.

The critical Rayleigh numbers Ra_c for $0 \leq \theta_k \leq 90^0$, $R = 0.125$ and $R = 0.5$ are graphically presented in Fig. 6.13. It is found that for a fixed permeability ratio $R < 1$, the critical Rayleigh number is a decreasing function of θ_k in the range of $0 \leq \theta_k \leq 90^0$ (the maximum permeability being in the horizontal direction for $\theta_k = 0$ and $R < 1$). For $R = 0.125$, it is also found that the primary and secondary modes consist of 3-cell and 2-cell vortices respectively as $0 \leq \theta_k \sim 30^0$, and of 2-cell and 3-cell vortices respectively in the range of $30^0 \leq \theta_k < 90^0$. For $R = 0.5$ the primary mode is 3-cell for the range $0 < \theta_k < 40^0$. Beyond $\theta_k = 40^0$, the primary mode is 2-cell. Furthermore, it is seen by comparing Fig. 6.13*a* and 6.13*b* that Ra_c may be a decreasing or increasing function of R according to the value of the angle θ_k. Physically, the anisotropy in permeability destroys the homogeneity of the resistance to the flow and favors the flow in the direction of higher permeability, resulting in a preference between the 2-cell and 3-cell flow patterns.

The primary and secondary modes (left and right) for $R = 0.125$ at $\theta_k = 0^0, 30^0, 60^0$ and 90^0 are shown in Fig. 6.14. It can be observed that the symmetry

axis for the flow and temperature fields deviates from the vertical central symmetric line of the cylinder for θ_k between 0^0 to 90^0.

(b) Finite Amplitude Convection

The numerical results cover the range $0 \leq Ra \leq 100$ and were obtained for various permeability ratios R and angles θ_k. According to the results from the linear stability analysis shown in Fig. 6.13a ($R = 0.125$), a 2-cell flow pattern is the primary mode for the range of $30^0 \leq \theta_k < 90^0$. That means a 2-cell flow pattern must exist at least for values of Ra in the small gap between the two curves in Fig. 6.13a. The results from the numerical code for finite amplitude convection confirmed this fact as seen in Fig. 6.15 which shows flow and temperature fields obtained numerically for $\theta_k = 75^0, R = 0.125$ and $Ra = 20.79$. For $\theta_k \neq n\pi/2$, (n being an arbitrary integer) and for Ra larger than the values within that gap, it was found impossible to obtain numerically a steady state flow pattern consisting of an even number of cells. Various attempts were tried at different Ra and θ_k, starting the computation from initial conditions that already contain a 2-cell flow field. With time, even at small angles such as $\theta_k = 0.5^0$, one of the cells grows to the detriment of the other and slowly moves toward the center. The other cell gradually shrinks and moves toward the boundary. A cell appears near the opposite side of the cylinder and the asymptotic result is the configuration with three cell or cells of odd number.

When $\theta_k = 0$, or 90^0, pairs of solutions consisting of 2-cell and 3-cell flow patterns may exist for given Rayleigh numbers and permeability ratios. Fig. 6.16a, b, c shows three typical pairs of flow patterns obtained for $Ra = 70$. The intermediate pair of flow pattern ($R = 1$) is given for comparison purpose. The upper pair corresponds to $\theta_k = 0$ and $R = 0.125$, i.e., the maximum permeability is in the horizontal direction. The lower pair corresponds to $\theta_k = 90^0$ and $R = 0.125$ or

equivalently to $\theta_k = 0$ and $R = 8$. As expected, the 2-cell flow configuration is symmetric with respect to the vertical diameter and the 3-cell flow configuration is centro-symmetric. As for the isotropic case, in the case of a centro-symmetric flow, the heat entering the cavity and the heat going out have identical distributions in θ with extrema in opposite locations. Consequently, the temperature averaged over the domain remains equal to zero for that type of flow pattern.

In Fig. 6.17, ψ_{ext}, the extreme value of the stream function obtained numerically, is given as a function of Ra at $R = 0.125$ for $\theta_k = 0$ and $\theta_k = 90^0$ respectively. ψ_{ext} corresponds to the value of stream function at the center for the centro-symmetric patterns, and to the value characterizing the side cells closest to the center for the flows having the symmetry with respect to the vertical diameter.

6.2.3 Summary

Both the permeability ratio and inclination angle of the principal axes have a strong influence on the critical value of Ra and on the initial flow pattern at the onset of convection. A minimum critical Ra can be achieved if the porous matrix is arranged such that the principal axis with higher permeability is in the vertical direction ($R < 1$, $\theta_k = \pi/2$). The initial flow pattern predicted by the linear stability analysis has a 3-cell structure or a 2-cell structure according to the value of θ_k.

No fluid motion exists unless $Ra > Ra_c$. To the difference of the isotropic porous medium [57], the critical Rayleigh number Ra_c is a function of θ_k and R. It is found from the linear stability analysis that Ra_c corresponding to $R = 0.125$, $\theta_k = 90^0$ is about 20, a value lower than the threshold for the isotropic case.

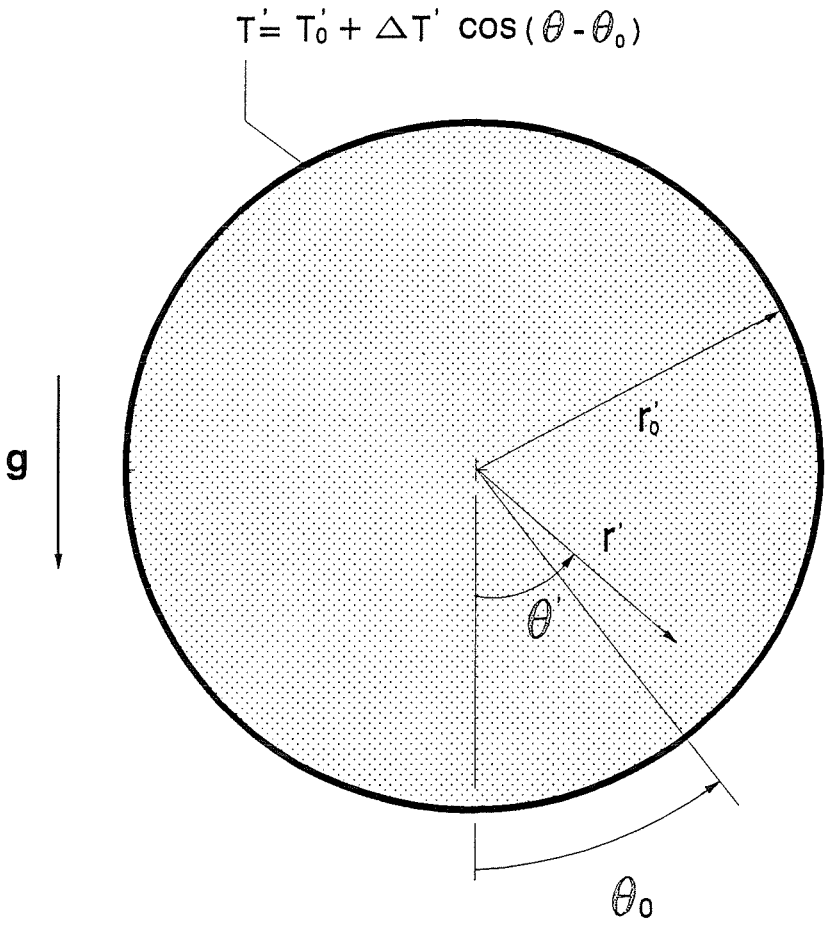

Figure 6.1: Definition sketch

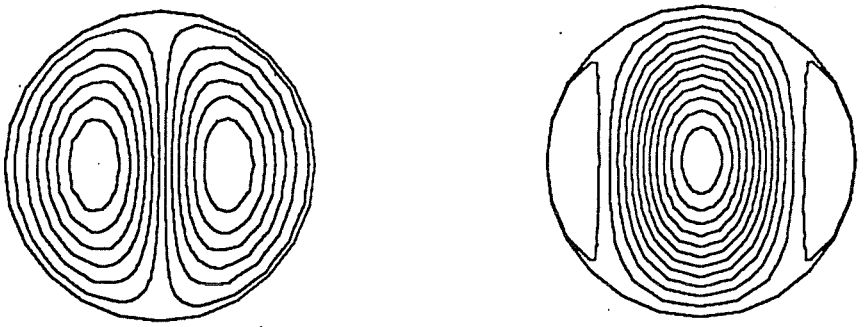

(a) 2-cell structure (b) 3-cell structure

Figure 6.2: Flow patterns at the onset of convection

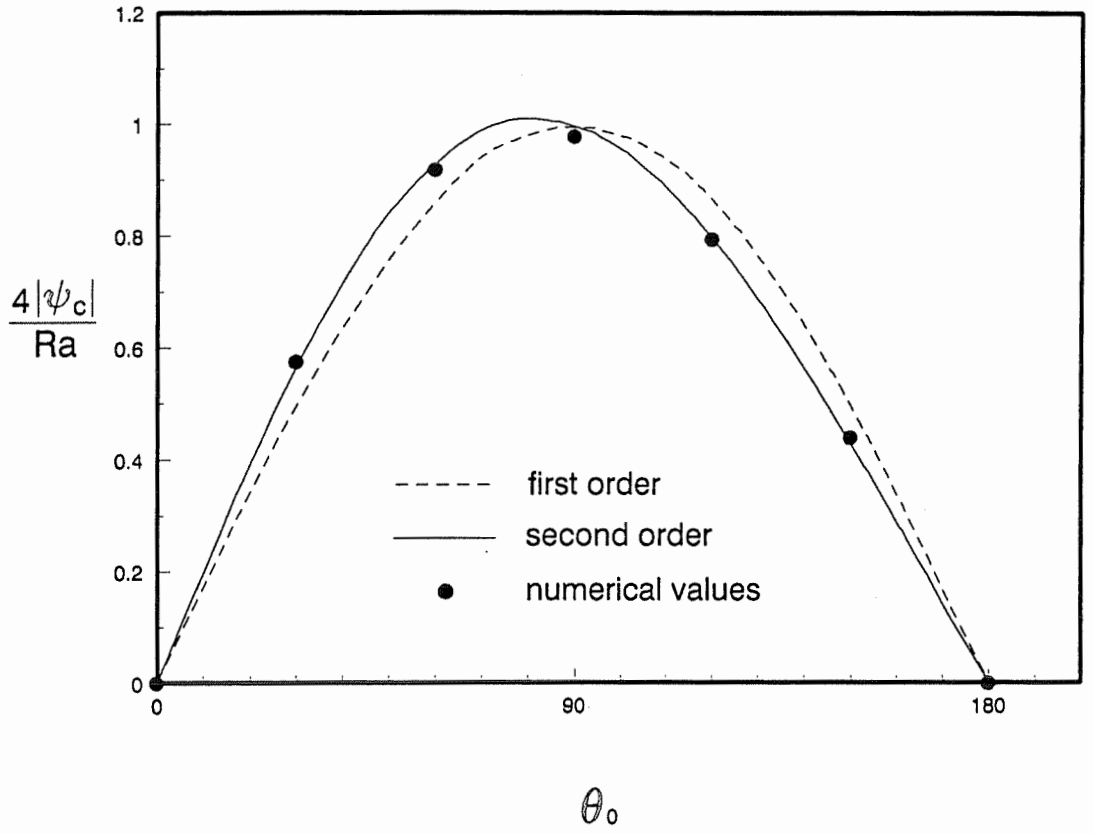

Figure 6.3: Comparison between analytical and numerical results (Ra=5)

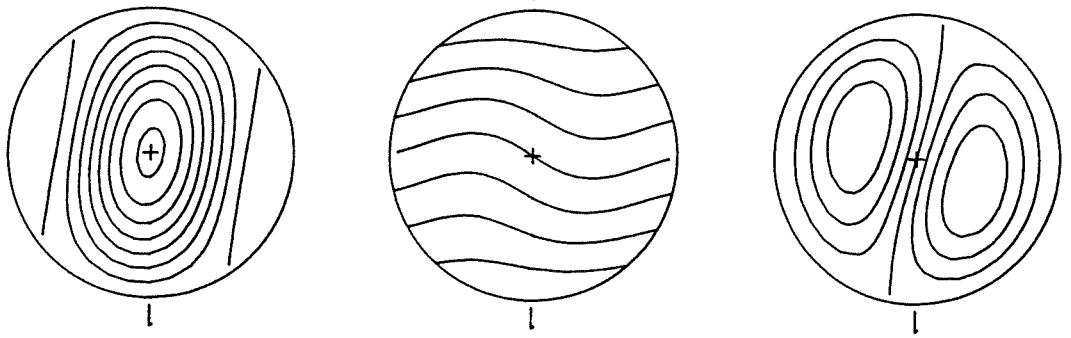

(*a*) $Ra = 25$, $\psi_c = -1.1879$, $\psi_s = 0.1162$

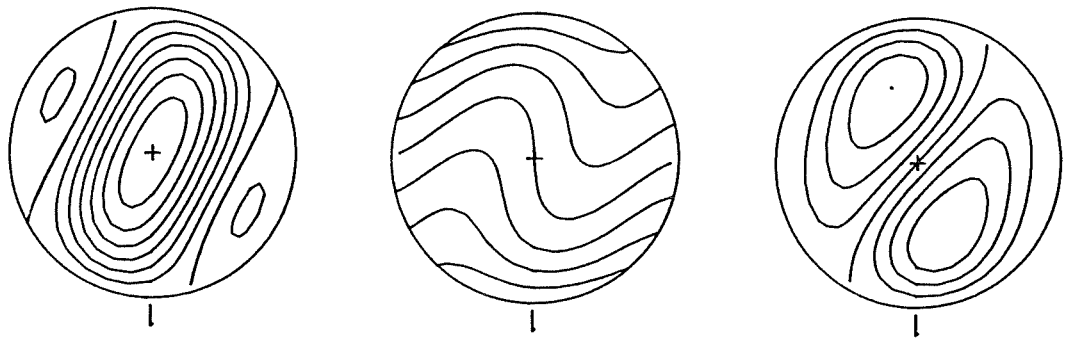

(*b*) $Ra = 40$, $\psi_c = -3.6482$, $\psi_s = 0.6350$

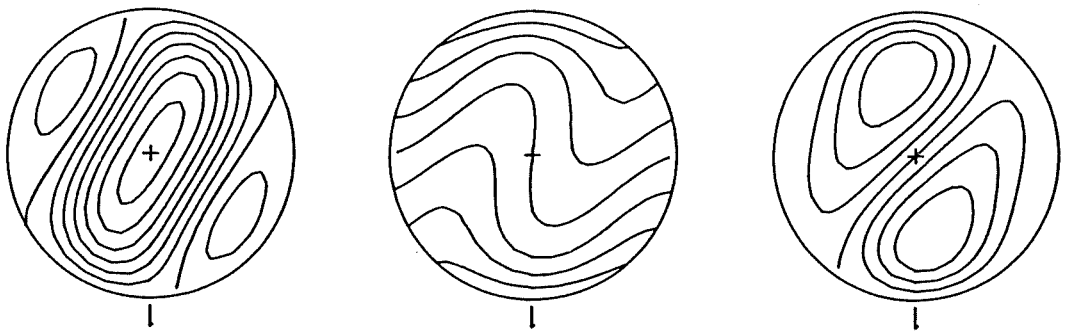

(*c*) $Ra = 50$, $\psi_c = -4.3942$, $\psi_s = 1.0524$

Figure 6.4: Flow and temperature fields (3-cell structure, $\theta_0 = 0$)

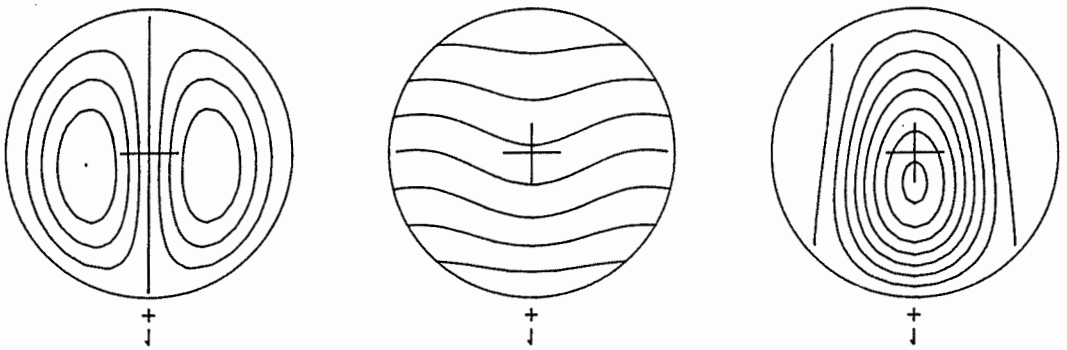

(*a*) $Ra = 25$, $\psi_{\max} = 0.7165$

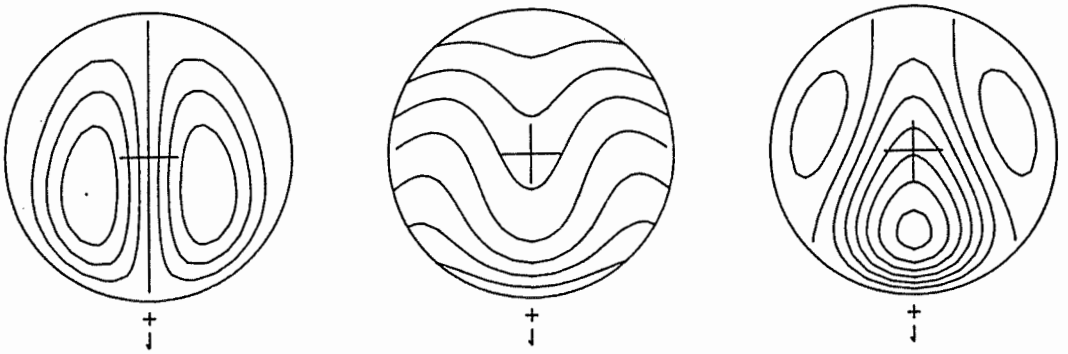

(*b*) $Ra = 40$, $\psi_{\max} = 2.7757$

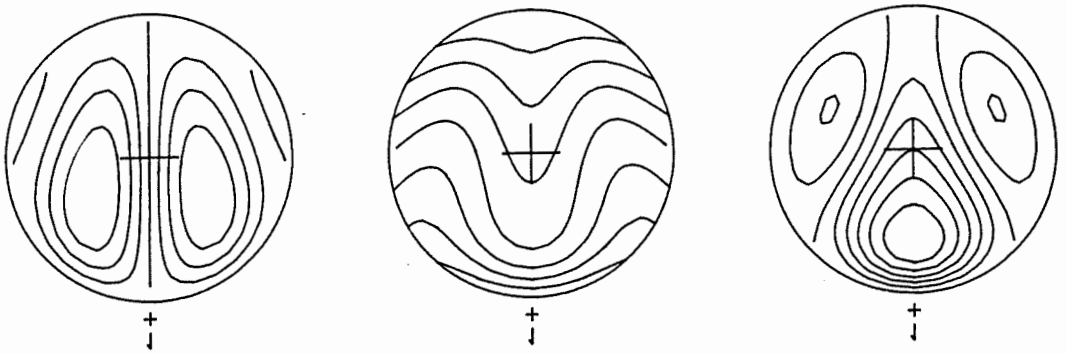

(*c*) $Ra = 50$, $\psi_{\max} = 3.5445$

Figure 6.5: Flow and temperature fields (2-cell structure, $\theta_0 = 0$)

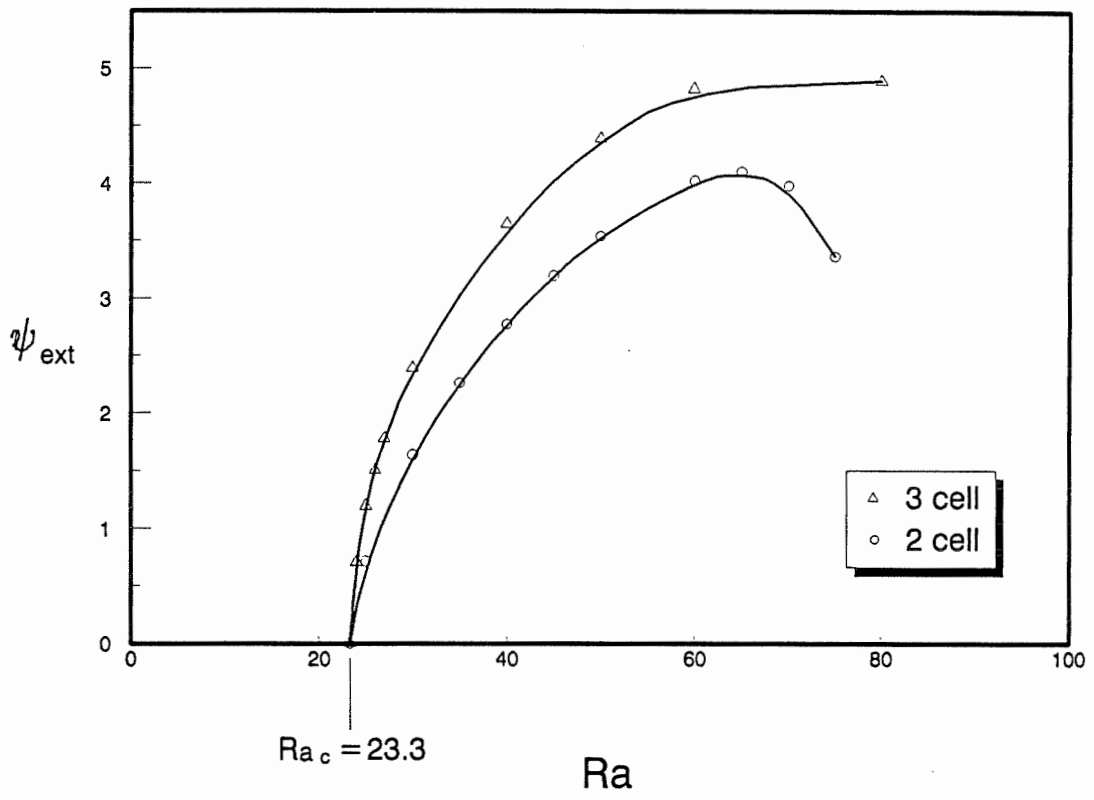

Figure 6.6: ψ_{ext} for 2-cell and 3-cell flow patterns, function of Ra ($\theta_0 = 0$)

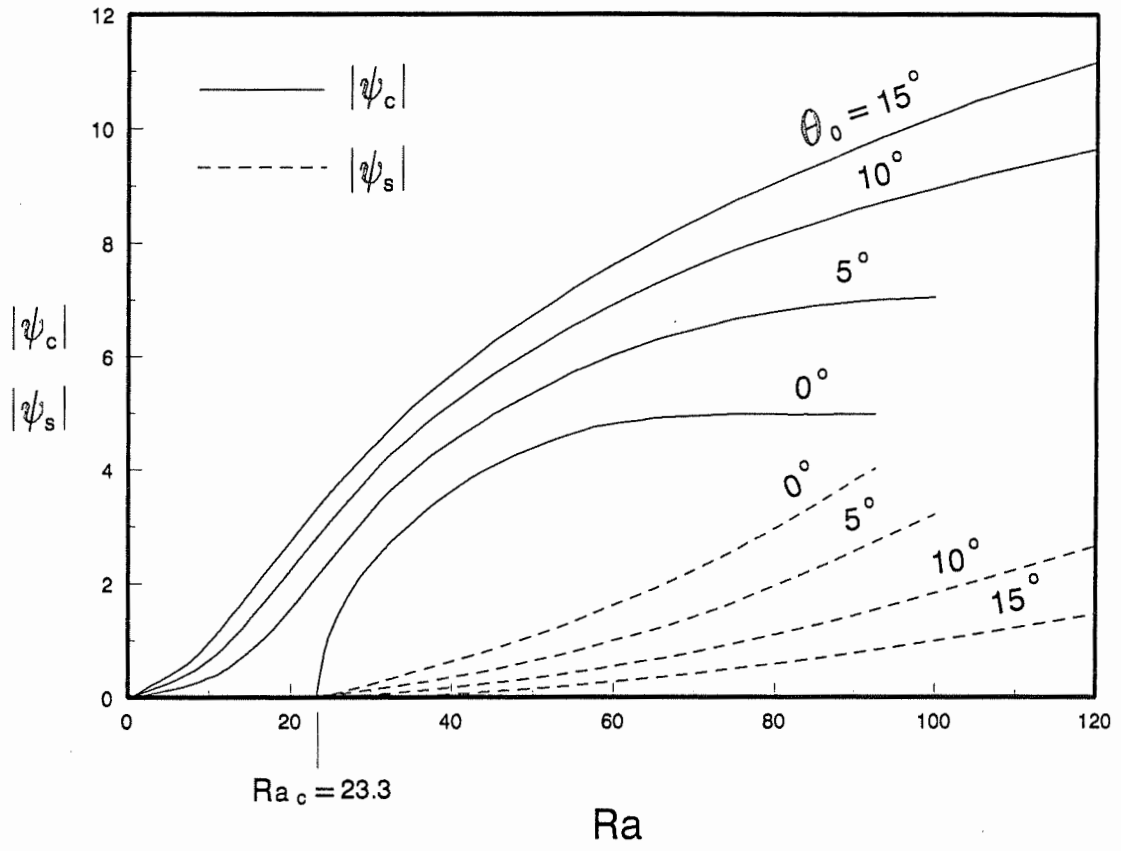

Figure 6.7: ψ_c and ψ_s, function of Ra and θ_0 (3-cell flow pattern)

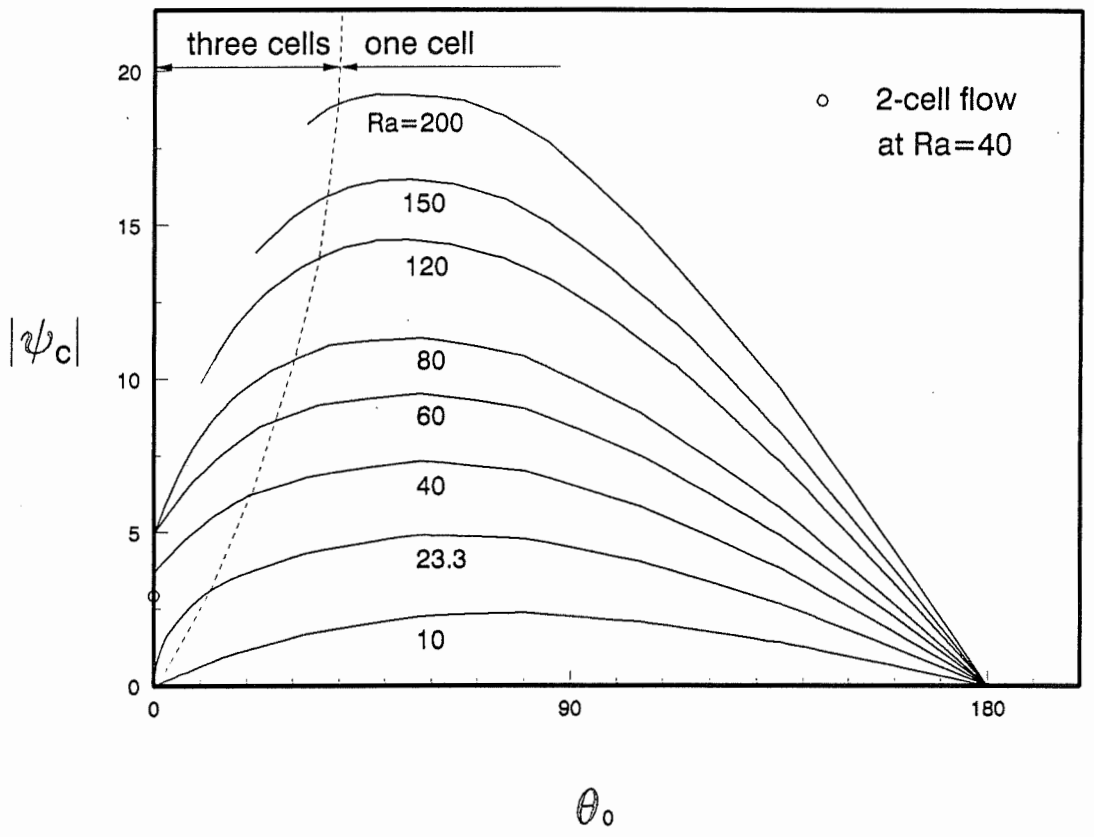

Figure 6.8: ψ_c, function of θ_0, for different values of Ra
(3-cell/1-cell flow pattern)

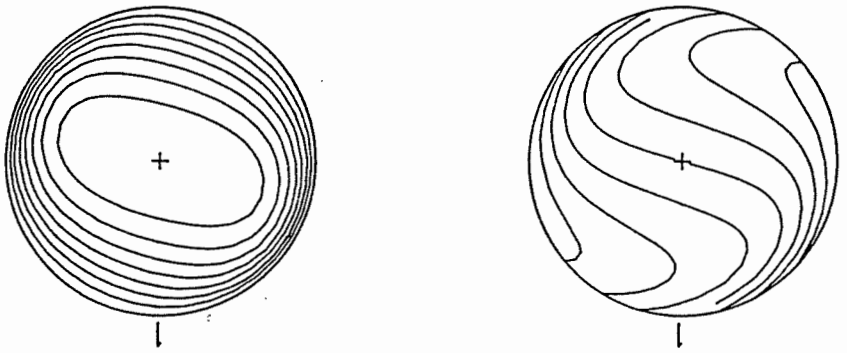

Streamlines ($\psi_c = -10.2391$) Isotherms

Figure 6.9: Single cell flow pattern ($Ra = 80$, $\theta_0 = 90^0$)

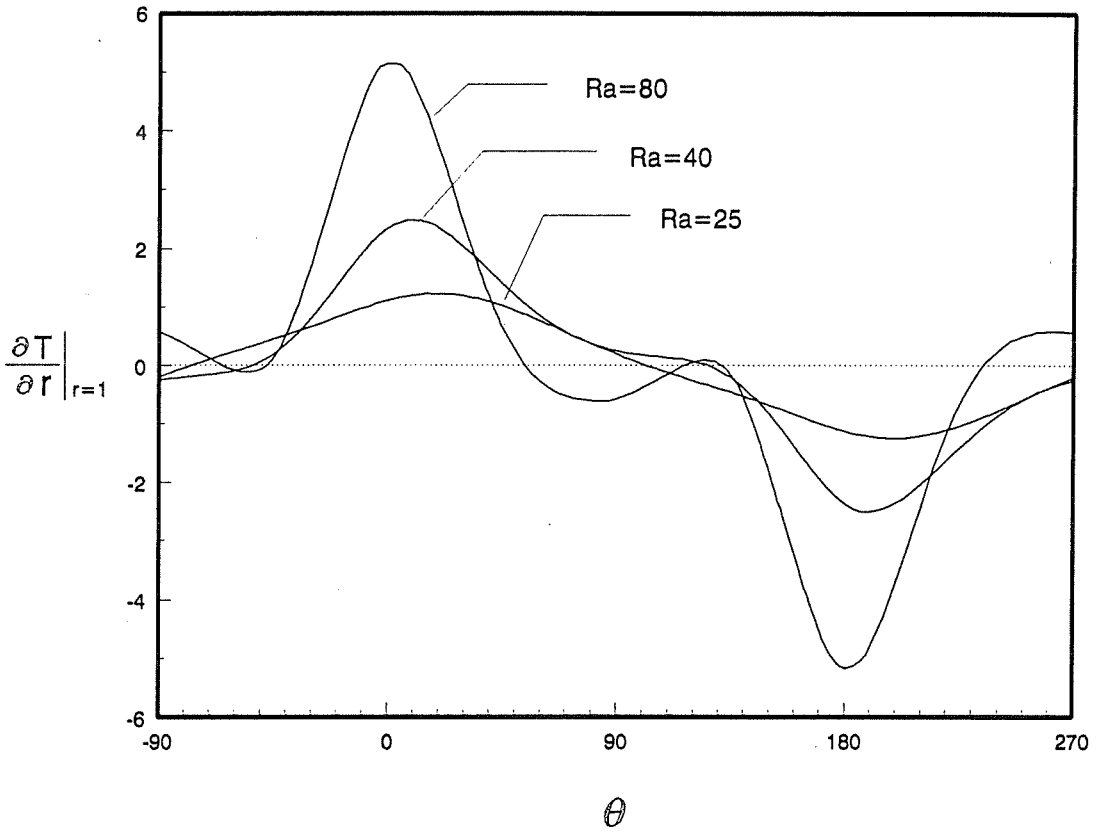

Figure 6.10: Local heat transfer at $\theta_0 = 0$ (3-cell flow pattern)

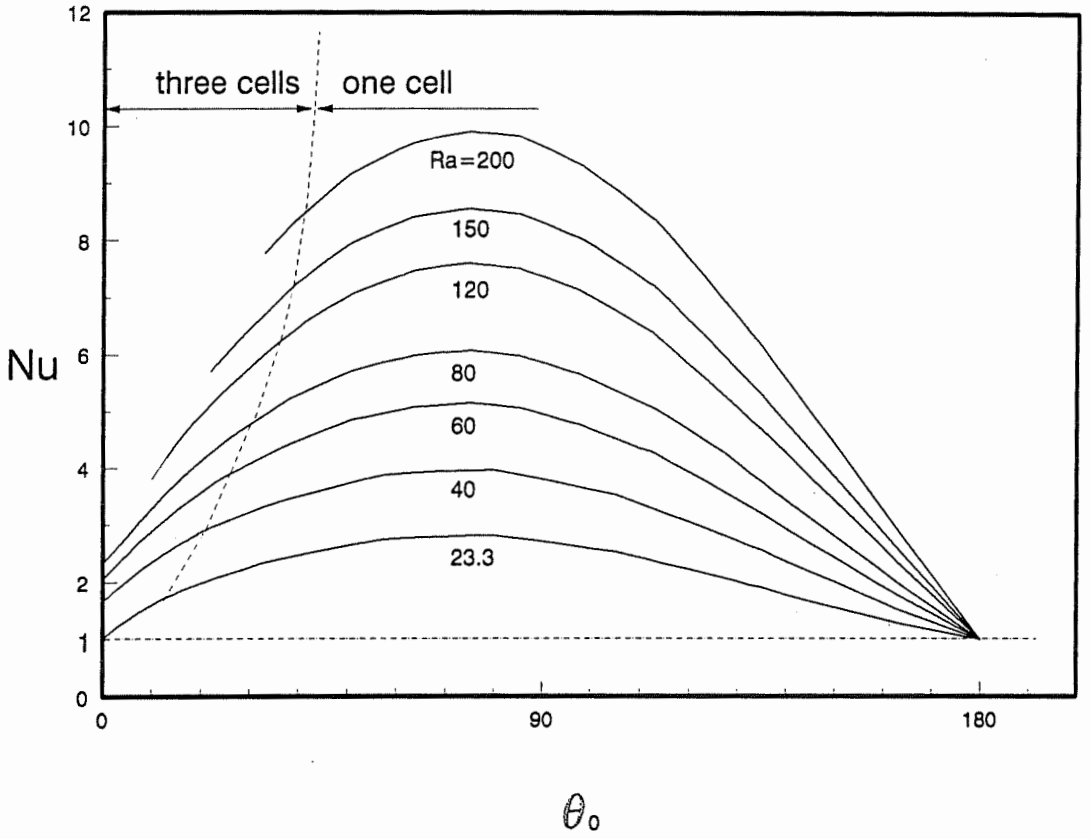

Figure 6.11: Nu, function of θ_0, for different values of Ra
(3-cell/1-cell flow pattern)

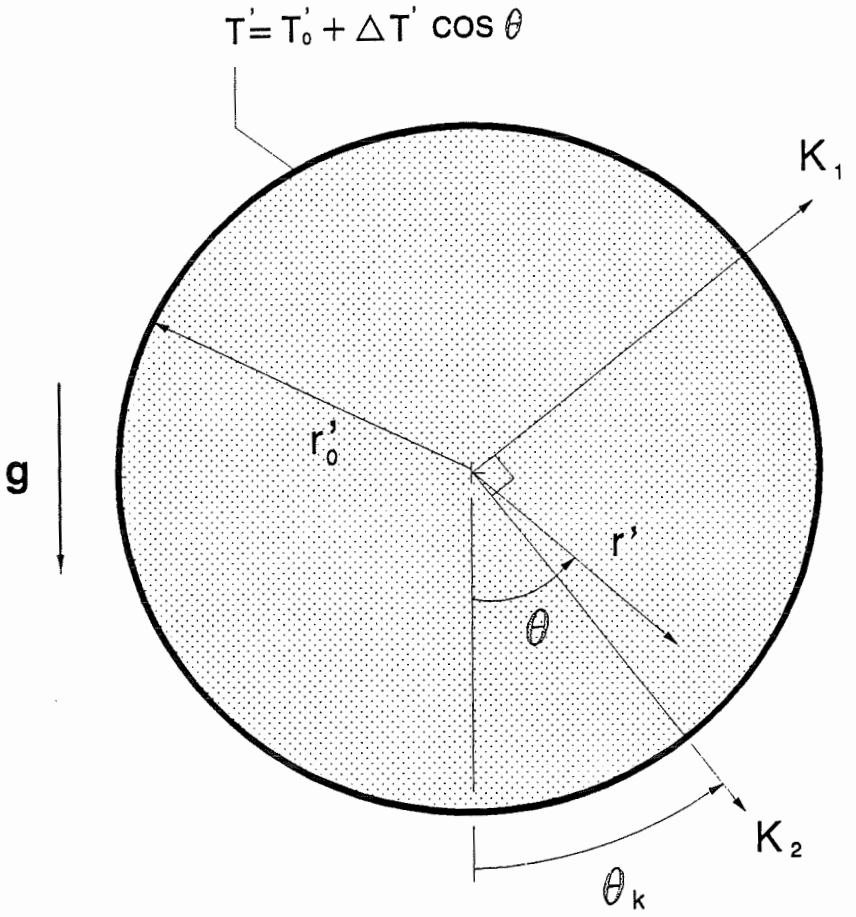

Figure 6.12: Definition sketch for anisotropic porous cylinder

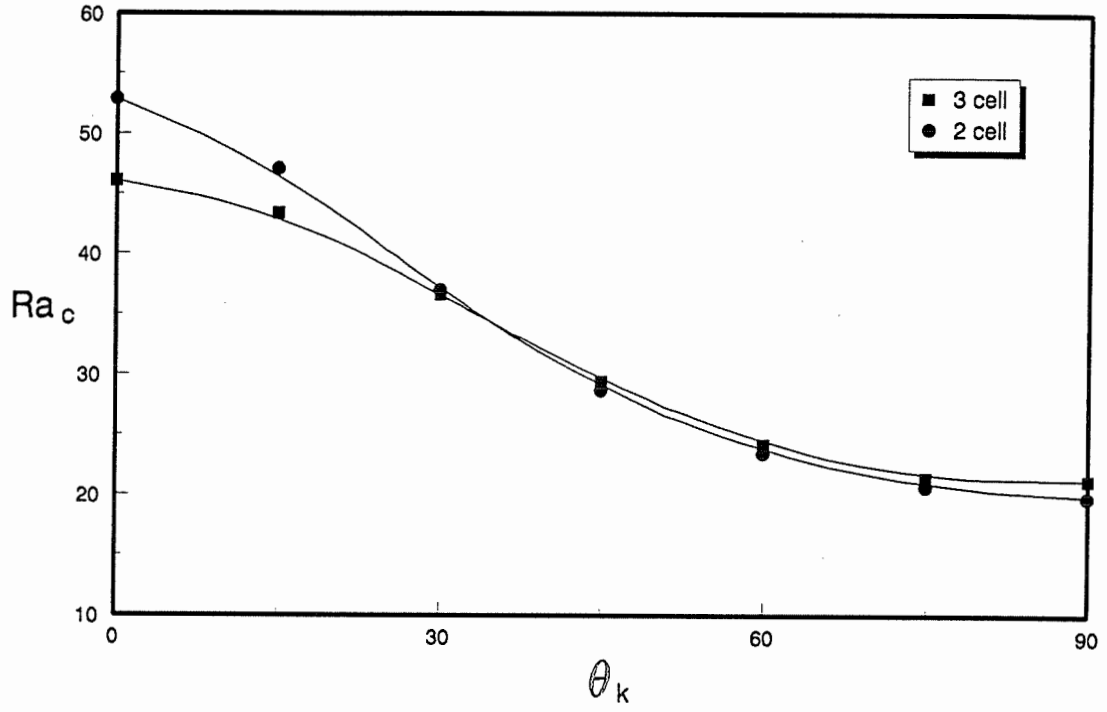

(*a*) $R = 0.125$

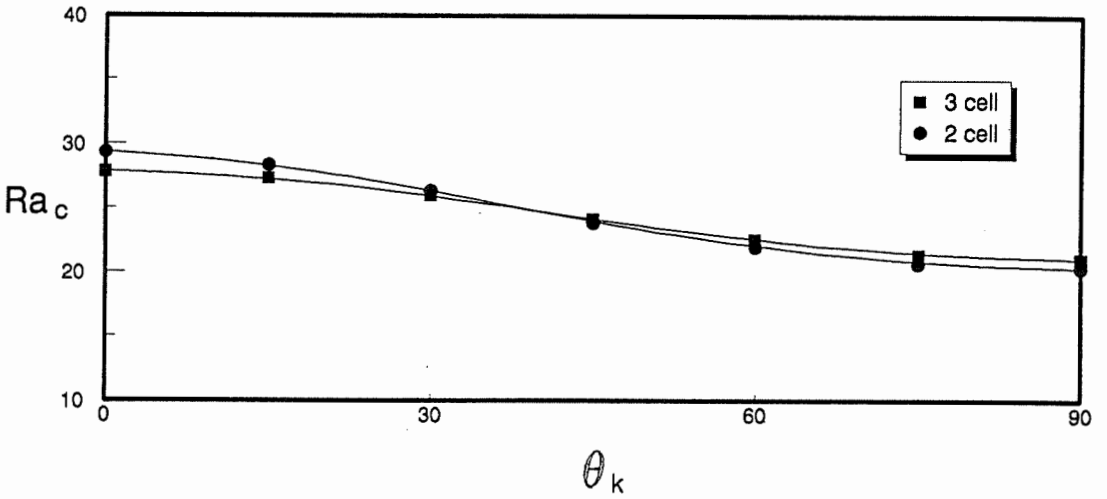

(*b*) $R = 0.5$

Figure 6.13: Critical Rayleigh number (primary and secondary modes), function of θ_k, for $R = 0.125$ and $R = 0.5$

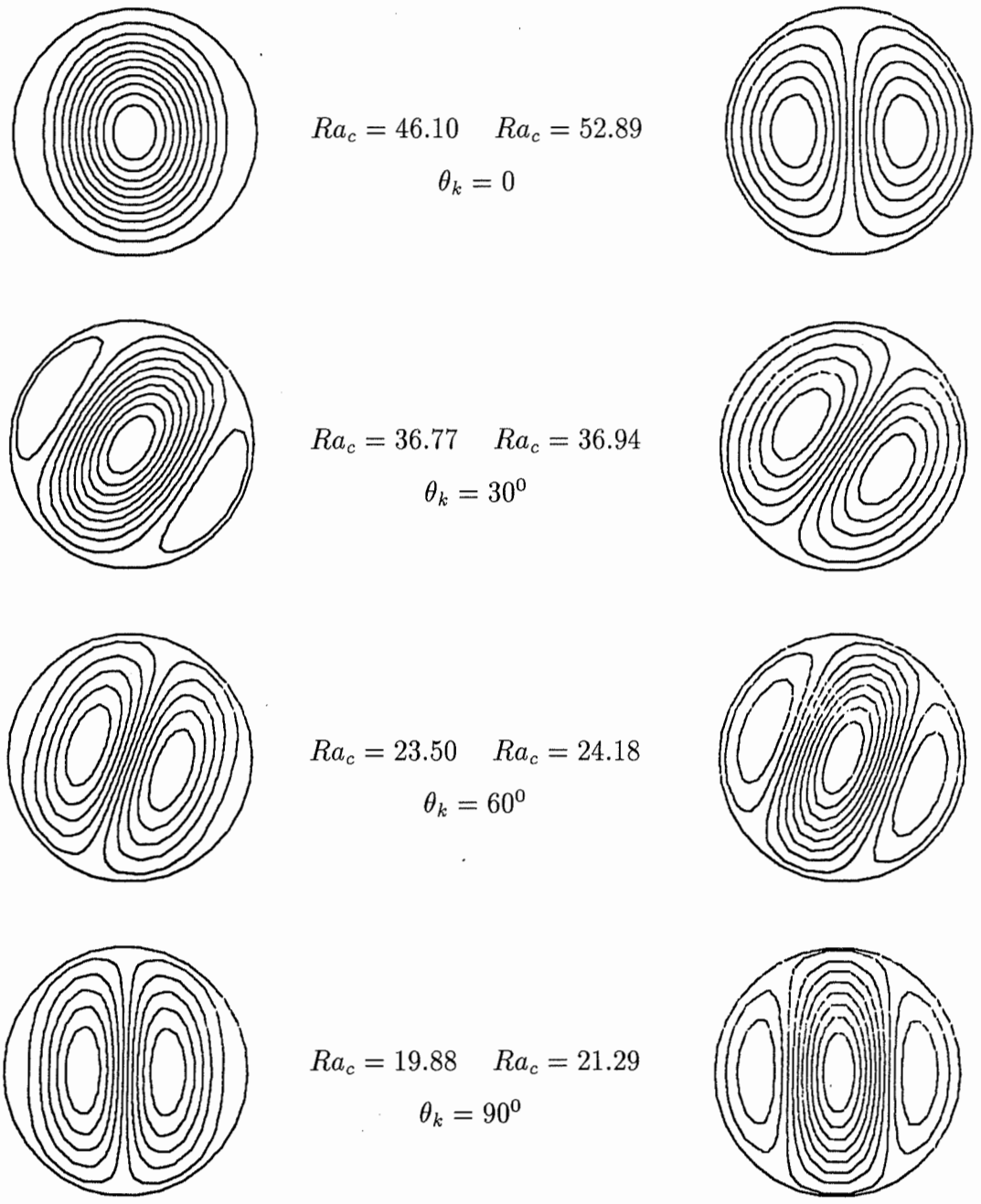

Figure 6.14: Incipient convection at various angles θ_k ($R = 0.125$)

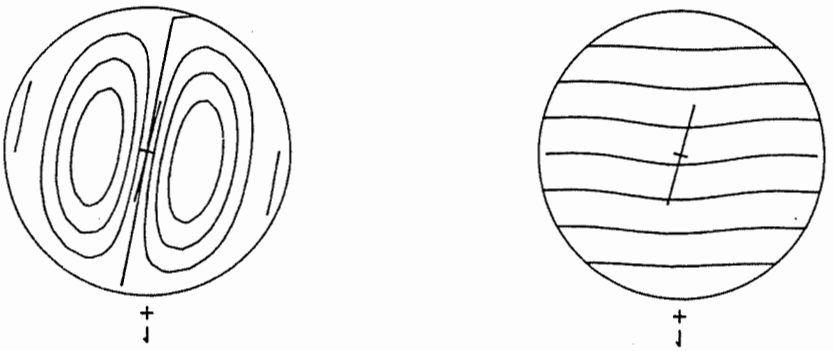

Streamlines ($|\psi_{\text{ext}}| = 0.2311$) Isotherms

Figure 6.15: Flow and temperature fields

($R = 0.125$, $\theta_k = 75^0$, $Ra = 20.79$)

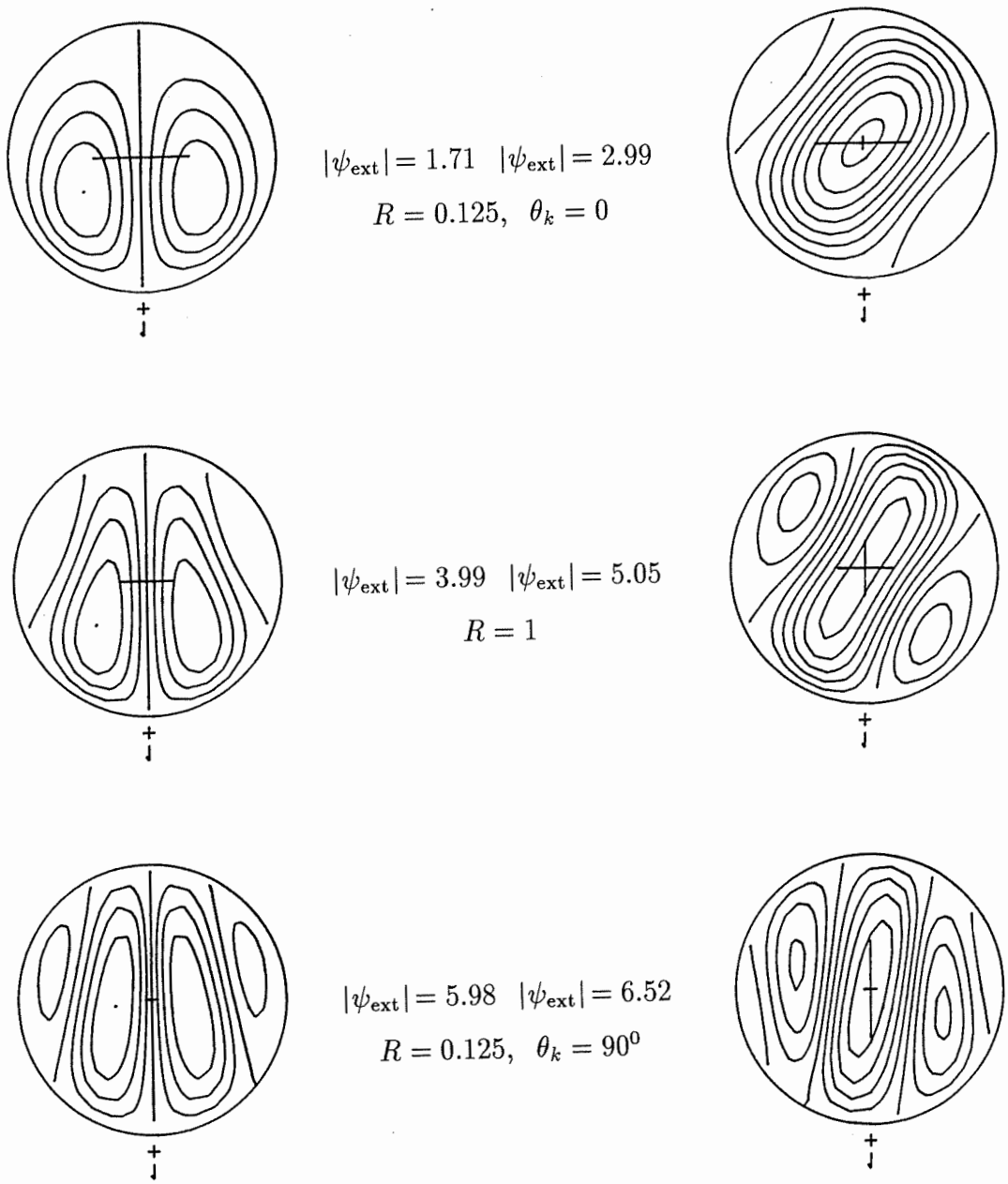

Figure 6.16: Finite amplitude convection ($Ra = 70$) - pairs of flow patterns

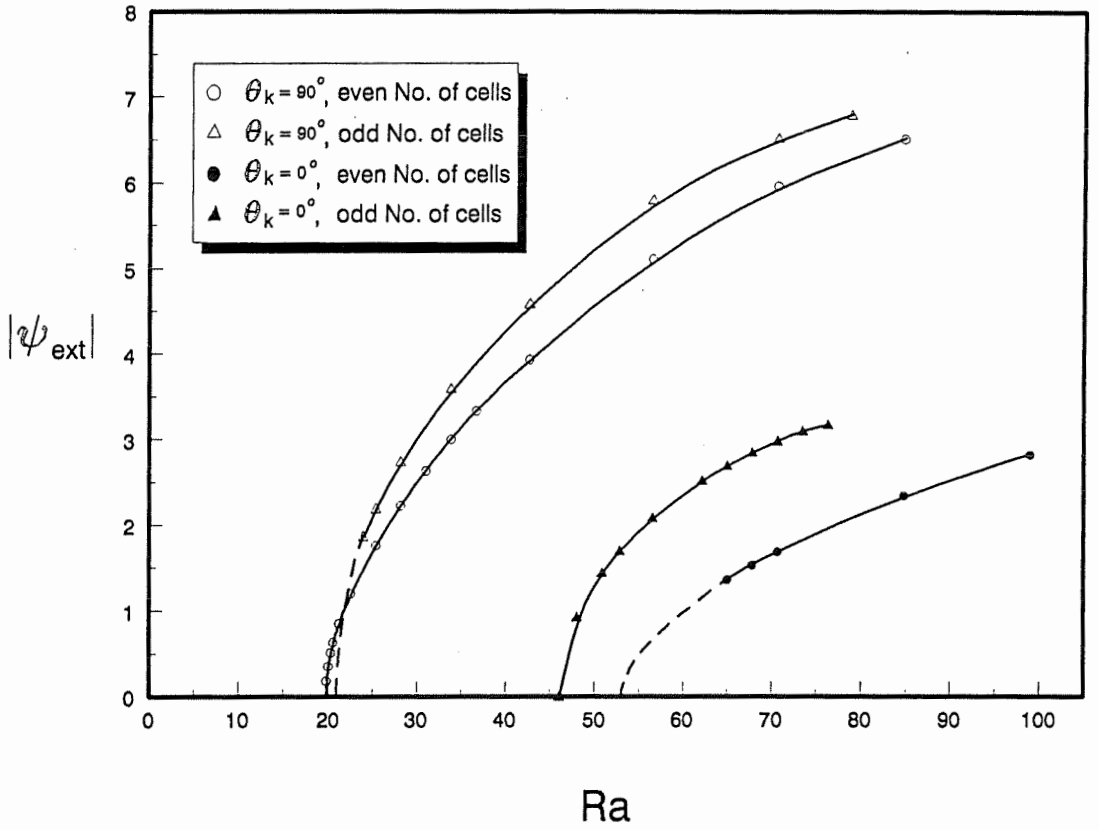

Figure 6.17: $|\psi_{\text{ext}}|$, function of Ra ($R = 0.125$)

Chapter 7

CONCLUSIONS AND RECOMMENDATIONS

In this study, the theoretical, i.e., numerical and analytical approaches have been developed to model fluid flow and heat transfer in fluid / isotropic / anisotropic porous media which confined in a horizontal circular cylinder. The study has been carried out by the means of numerical simulation, perturbation method and linear stability analysis. Results from different approaches have been found to coincide.

Within the present framework, some cases with fundamental and practical interests have been studied: A) mixed convection in a low rotation isotropic porous / fluid cylinder, B) natural convection in a fast rotation isotropic / anisotropic porous cylinder and C) thermal stability analysis in a non-rotating isotropic / anisotropic porous cylinder subject to a sinusoidal temperature distribution on its boundary.

By contrast with many previous works on the same geometry, the whole circular cylinder was considered as a flow domain for each of these three cases. This was of necessity for the first and last case since no symmetry with respect to the vertical diameter could be involved. The numerical finite difference approach, based on cylindrical coordinates had to handle the artificial (or mathematical) singularity at the center in a way to avoid any bias to the flow. The special features of the numerical approach aimed at solving that difficult are described in Chapter 2. They were successful in reproducing results from previous studies and some predicted values from the numerical approach were confirmed by analytical approaches for case A) and C).

Detailed conclusions for each one of the aforementioned cases are

A) The behavior of natural and mixed convection in a low rotation horizontal cylinder filled with an isotropic porous / fluid medium with isothermal boundary condition and uniformly distributed heat sink is first investigated. This kind of problem is equivalent to the case without heat sink or source and with boundary temperature increasing at a steady rate with time. Weak rotation regime only were undertaken, for which the force field is terrestrial gravity exclusively. A qualitatively similar behavior for both isotropic porous medium and fluid medium under same conditions were found. The interaction between convective rolls resulting from standard free convection case and the effects of rotation were studied numerically and by perturbation method. For the finite amplitude convection, the numerical results based on finite difference scheme cover a broad range of Rayleigh and Peclet numbers. In addition, a regular perturbation method was used to study the incipient rotation and validate the numerical approach. Results from both approaches coincide. Those approaches were applied both to the isotropic porous medium and to the fluid medium.

For the isotropic porous medium case, both approaches revealed that a large part of the saturated fluid does not participate to rotation at low rotation speed. Thus the stream function at the center may differ largely from zero. However, with increasing angular velocity, the fluid is gradually entrained and a solid body rotation regime develops for which the convective heat transfer is eventually reduced to zero. Similarly, for the fluid medium case, a net flow relative to cylinder boundary is found at low rotation speed (shear flow regime) and a solid body rotation occur at high angular velocities (solid body rotation regime) in which the rotational effects on convection are found to reduce the heat transfer towards the pure conduction level. The difference between both media is that the net flow in fluid medium has a drastic drop at high Rayleigh number due to the oscillating behavior caused by the inertial term in fluid medium, whereas the transition to solid body rotation regime

occurs gradually for the porous medium without oscillating (unsteady) behavior. By comparison to the study of Ladeinde and Torrance [29], one has gained better understanding in the physical behavior of fluid in the same case: Nusselt number, dimensionless shear stress and stream function at center have been quantitatively related to the rotating speed expressed by the Peclet number; and the relationship between incipient rotation and the value of the stream function at center has been established, characterizing the part of flow mass tied to the terrestrial gravity.

B) Then Bénard convection in a fast rotation isotropic / anisotropic porous cylinder with isothermal condition on the boundary and uniformly distributed heat sink is studied. In the situation of fast rotation, only the centrifugal force is involved, the terrestrial gravity being assumed negligible. Under those conditions, the direction of the pure conduction density gradient is toward the geometric center of cylinder and the centrifugal force field is acting on fluid in the opposite direction. Such a force balance is potentially unstable and Bénard cells are expected to occur beyond a critical Rayleigh number. For the isotropic case, a linear stability analysis solved analytically was used to predict the critical Rayleigh number for incipient convection and the results were compared with those from a linear stability analysis solved numerically. Moreover, results from finite amplitude convection are consistent with those concerning incipient convection. The results of the present investigation revealed that there exists a threshold $Ra_c = 348$ beyond which convection takes place and multiple solutions are possible for Rayleigh numbers well above this critical value. Only a 4-cell structure flow occurs at the incipient convection and a stable solution at high Ra numbers will contain more cells. This is in contrast with the case of fluid medium, where a 2-cell pattern appears first. Anisotropy of permeability was found to have a strong effect on Ra_c, which can be lower than the threshold aforementioned. Moreover the first flow configuration for anisotropic porous medium to appear may even contain six cells instead of four cells if the per-

meability ratio is far enough from unity. Also unlike the isotropic case, no more double roots exist at incipient convection. Furthermore it has been observed that the flow pattern takes an angular position such that it possesses symmetry with respect to the principal axes, which is different from the isotropic case where there is no physical requirement on angular position of the flow pattern.

C) Final investigation of the present study is about the Bénard instabilities in a non-rotating isotropic / anisotropic porous cylinder having sinusoidally distributed temperature on the boundary in the presence of terrestrial gravity. Such a distribution in temperature is equivalent to a linear thermal stratification of the surroundings in a given direction. A particular case is that the maximum temperature is at the bottom ($\theta_0 = 0$, bottom heating). The thermal stratification imposed on the circular boundary is then in the vertical direction and consequently the direction of the density gradient is opposite to the terrestrial gravity, giving rise to a potentially unstable force balance in pure conduction. For the isotropic porous medium with bottom heating, the critical value of the Rayleigh number for convective motion to appear has been found to be approximately 23.3, with two types of flow configurations: a flow configuration involving two convective cells, symmetric with respect to the vertical diameter, and a centro-symmetric flow configuration containing three cells. Also numerical results for finite amplitude convection at $\theta_0 = 0$ show that both 2-cell and 3-cell are stable configurations for a given range of Ra. Numerical solutions were also obtained at different Rayleigh numbers for an arbitrary location of the maximum temperature on the boundary. The flow is then unicellular unless the maximum temperature lies somewhere in the neighborhood of the unstable position ($\theta_0 = 0$). Results from linear stability analysis, regular perturbation and numerical simulation were found to be in good agreement. For the anisotropic case, our discussion was limited to bottom heating only. Both the ratio of permeability R and the angle of the principal axes θ_k have a strong influence

on the critical values of the Rayleigh number and the initial flow patterns. The minimum critical Ra is obtained when the principal axis with higher permeability is in the vertical direction ($R < 1$, $\theta_k = \pi/2$). It is found from the linear stability analysis that Ra_c corresponding to $R = 0.125$ and $\theta_k = 90^0$ is about 20, a value lower than the threshold for the isotropic case. The initial flow pattern predicted by the linear stability analysis has a 3-cell structure or a 2-cell structure according to the value of θ_k. To the difference of the isotropic porous medium [57], the critical Rayleigh number Ra_c does not have a fixed value but is function of θ_k and R. Finite amplitude convection was investigated numerically and results from linear stability analysis and numerical simulation agree well.

For the case where combined terrestrial gravity and centrifugal forces are involved simultaneously, further investigations are needed. As mentioned at the beginning of Chapter 2, a better understanding of the asymptotic cases discussed in this study was a prerequisite to the undertaking of the intermediate cases.

Finally, it can be stated on a general basis that the effect of anisotropy is equivalent, under certain circumstances where the Maxwell and momentum equations are uncoupled, to the effect of a magnetic field on the flow behavior, as evidenced by the relevant equations of Chapter 2. It should be recalled that the use of magnetic field has been proposed as a means of reducing the natural convection in the process of crystal growth.

Bibliography

[1] P. VADASZ. (1993). Three-dimensional free convection in a long rotating porous box. J. Heat Transfer, 115, 639-644.

[2] H. Q. YANG, K. T. YANG, and J. R. LLOYK. (1988). Rotational effects on natural convection in a horizontal cylinder. AICHE Journal, 34, 1627-1633.

[3] C. O. BALL and F. C. W. OLSON. (1957). Sterilization in Food Technology, McGraw-Hill.

[4] L. E. CLIFCORN, G. T. PETERSON, J. M. Boyd, and J. H. O'Neil. (1950). A new principle for agitating in processing of canned foods. Fd. Technol., 4, 450-460.

[5] F. LADEINDE. (1988). Studies of Thermal Convection in Self-Gravitating and Rotating Horizontal Cylinders in a Vertical External Gravity Field. PhD thesis, Cornell University.

[6] A. LOPEZ. (1981). A Complete Course in Canning, Book 1, Basic Infomation on Canning, The Canning Trade, Baltimore.

[7] R. HANNEMANN. (1990). Thermal control for mini-and microcomputers: The limits of air cooling. Heat Transfer in Electronic and Microelectronic Equipment, 61-82.

[8] A. BAR-COHEN and A. D. KRANS. (1983). Thermal Analysis and Control of Electronic Equipment, Hemisphere Publishing Corporation.

[9] A. D. KRAUS. (1965). Cooling Electronic Equipment, Prentice - Hall, Englewood Cliffs, N.J.

[10] Y. T. LIN, M. CHAI, and R. GREIF. (1991). A three-dimensional analysis of the flow and heat transfer for the modified chemical vapor deposition process including buoyancy, variable properties, and tube rotation. Trans. ASME C: J. Heat Transfer, 113, 400-406.

[11] Y. T. LIN, M. CHAI, and R. GREIF. (1992). A three-dimensional analysis of particle deposition for the modified chemical vapor deposition (MCVD) process. Trans. ASME C: J. Heat Transfer, 114, 735-742.

[12] E.H. SCHMIDT. (1951). Heat Transmission by Natural Convection at High Centrifugal Acceleration in Water-Cooled Gas-Turbine Blades, General Discussion on Heat Transfer. Inst. Mech. Engr., London.

[13] W. ZHENG and W. M. WOREK. (1993). Numerical simulation of combined heat and mass transfer processes in a rotary dehumidifier. Numerical Heat Transfer, 23, 211-232.

[14] R. V. DUNKLE. (1965). A method of solar air conditioning. Mechanical and Chemical Transactions, MCI, 1, 73-78.

[15] E. VAN DEN BULCK, S.A. KLEIN, and J.W. MITCHELL. (1988). Second law analysis of solid desiccant rotary dehumidifiers. ASME: J. Solar Energy Eng., 110, 2-9.

[16] R. HIDE and P. J. MASON. (1970). Baroclinic wavess in a rotating fluid subject to inernal heating. Phil. Trans. R. Soc. Lond., A268, 201-232.

[17] A. T. HSUI, D. L. TURCOTTE, and K. E. TORRANCE. (1972). Finite amplitude thermal convection within a self-gravitating fluid sphere. Geophys. Fluid Dyn., 3, 35-44.

[18] A. D. WEIR. (1976). Axisymmetric convection in a rotating sphere. J. Fluid Mech., 75, 49-79.

[19] P. RANDRIAMAMPLANINA, A. BONTOUX and B. ROUX. (1987) Ecoulements induits par la force gravifique dans une cavite cylindrique en rotation. Int. J. Heat Mass Transfer, 30, 1275-1292.

[20] F. H. BUSSE. (1986). Asymptotic theory of convection in a rotating, cylindrical annulus. J. Fluid Mech., 173, 545-556.

[21] R. HIDE. (1967). Theory of axisymmetric thermal convection in a rotating fluid annulus. Phys. Fluids, 10, 56-68.

[22] R. HIDE and P. J. MASON. (1974). Sloping convection in a rotating fluid. Adv. Phys., 24, 47-100.

[23] I. S. BJORDLUND and W. M. KAYS. (1959). Heat transfer between concentric rotating cylinders. J. Heat Transfer, 81, 175-719.

[24] J. KAYE and E. C. ELGAR. (1958). Modes of adiabatic and diabatic fluid flow in an annulus with an inner rotating cylinder. ASME Trans., 80, 753-765.

[25] C. GAZLEY. (1958). Heat transfer characteristics of the rotational and axial flow between concentric cylinders. ASME Trans., 80, 79-90.

[26] T. S. LEE. (1984). Numerical experiments with laminar fluid convection between concentric and excentric heated rotating cylinders. Num. Heat Transfer, 7, 77-87.

[27] T. FUSEGI, B. FAROUK, and K. S. BALL. (1986). Mixed convection flows within a horizontal concentric annulus with a heated rotating inner cylinder. Num. Heat Transfer, 9, 591-604.

[28] L. ROBILLARD and K. E. TORRANCE. (1990). Convective heat transfer inhibition in an annular porous layer rotating at weak angular velocity. Int. J. Heat Mass Transfer, 33, 953-963.

[29] F. LADEINDE and K. E. TORRANCE. (1991). Convection in a rotating, horizontal cylinder with radial and normal gravity forces. J. Fluid Mech., 228, 361-385.

[30] L. PRUD'HOMME, M. ROBILLARD and M. HILAL. (1993). Natural convection in an annular fluid layer rotating at weak angular velocity. Int. J. Heat Mass Transfer, 36, 1529-1540.

[31] M. HASNAOUI, P. VASSEUR, E. BILGEN, and L. ROBILLARD. (1995). Analytical and numerical study of natural convection heat transfer in vertical porous annulus. Chem. Eng. Comm., 80, 77-94.

[32] G. M. HOMSY and J. L. HUDSON. (1969). Centrifugally driven thermal convection in a rotating cylinder. J. Fluid Mech., 35, 33-52.

[33] H. BENARD. (1900). The cellular motion in a liquid layer transporting heat by convection in a steady regime. Rev. Gen. Sci. Pur. Appl., 12, 1261.

[34] H. QUACK. (1970). Naturliche konvektion innerhalb eines horizontalen zylinders bei klein Grashof zahlen. Wärme-und-stoffübertragung, 3, 134-138.

[35] F. K. DEAVER and E. R. G. ECKERT. (1970). An interferometeric investigation of convective heat transfer in a horizontal fluid cylinder with wall temperature increasing at a uniform rate. Proc. 4th Int. Heat Transfer Conf., Toronto, 6, 13-43.

[36] M. TAKEUCHI and K. C. CHENG. (1976). Transient natural convection in horizontal cylinders with constant cooling rate. Wärme-und-stoffübertragung, 9, 215-225.

[37] D. L. NGUYEN and T. H. NGUYEN. (1986). Analysis of convective heat transfer in a horizontal cylinder with computer-extended perturbation series. Proc. 8th Int. Heat Transfer Conf., San Francisco, 2, 331-336.

[38] S. WEINBAUM. (1964). Natural convection in a horizontal circular cylinder. J. Fluid Mech., 18, 409-437.

[39] P.J. BRUNS, L.C. CHOW, and C.L. TIEN. (1977). Convection in a vertical slot filled with porous insulation. Int. J. Heat and Mass Transfer, 120, 919-926.

[40] T. NILSEN and L. STORESLETTEN. (1990). An analytical study on natural convection in a isotropic and anisotropic porous channels. Trans. ASMEC: J. Heat Transfer, 112, 396-401.

[41] P. A. TYVAND and L. STORESLETTEN. (1991). Onset of convection in an anisotropic porous medium with oblique principal axes. J. Fluid Mech., 226, 371-382.

[42] X. ZHANG. (1993). Convective heat transfer in vertical porous layer with anisotropic permeability. Proc. 14th CANCAM, 2, 579-580.

[43] J. CALTAGIRONE. (1976). Thermoconvective instabilities in a porous medium bounded by two concentric horizontal cylinders. J. Fluid Mech., 76, 337-362.

[44] W. R. C. PHILLIPS. (1988). The Generalized Lagrangian Mean Equations and Streamwise Vortices. Near Wall Turbulence, Hemisphere, New York.

[45] P. VASSEUR, M. HASNAOUI, E. BILGEN, and L. ROBILLARD. (1995). Natural convection in an inclined fluid layer with a transverse magnetic field: Analogy with a porous medium. J. Heat Transfer, 117, 121-129.

[46] G. K. BATCHELOR. (1967). An Introduction to Fluid Dynamisc, Cambridge University Press, London.

[47] P. CHENG. (1978). Heat transfer in geothermal systems. Advances in Heat Transfer, 14, 1-105.

[48] J. BEAR. (1972). Dynamics of Fluids in Porous Media, Elsevier, New York.

[49] P. VASSEUR and L. ROBILLARD. (1987). The Brinkman model for boundary layer regime in a rectangular cavity with uniform heat flux from the side. Int. J. Heat Mass Transfer, 30, 717-727.

[50] G. NEALE. (1977). Degrees of anisotropy for fluid flow and diffusion (electrical conduction) through anisotropic porous media. AIChE Journal, 23, 56-62.

[51] P. J. ROACHE. (1980). Numerical Heat Transfer and Fluid Flow, Hemisphere Publishing Corporation, New York.

[52] P. J. ROACHE. (1982). Computational Fluid Dynamics, Hermosa Publisher, Albuquerque.

[53] G. DE VAHL DAVIS. (1979). A note on a mesh for use with polar coordinates, Num. Heat Transfer, 2, 261-266.

[54] R. J. KEE and A. A. MCKILLOP. (1977). A numerical method for predicting natural convection in horizontal cylinders with asymmetric boundary conditions, Computer and Fluids, 5, 1-14.

[55] M. R. SPIEGEL. (1985). Mathematical handbook of formulas and tables. (French Version), McGraw-Hill.

[56] L. STORESLETTEN and M. TVEITEREID. (1987). Thermal convection in a porous medium confined by a horizontal cylinder. ASME HTD.

[57] L. ROBILLARD, X. ZHANG, and M. ZHAO. (1993). On the instability of a fluid-saturated porous medium contained in a horizontal circular cylinder, ASME Winter Annual Meeting. 264, 49-55.

[58] M. SEN, P. VASSEUR, and L. ROBILLARD. (1987). Multiple steady states for unicellular natural convection in an inclined porous layer. Int. J. Heat Mass Transfer, 30, 2097-2113.

[59] P. EHRHARD and U. MULLER. (1990). Dynamical behavior of natural convection in a single-phase loop. J. Fluid Mech., 217, 487-518.

Appendix A

THE BOUSSINESQ APPROXIMATION AND THE MIXED CONVECTION

In the momentum equation (2.1) for the fluid medium in the rotating coordinate system, the body force acting on the fluid medium consists of three parts, i.e., the terrestrial gravity, centrifugal force and Coriolis force. The fluid velocity $\mathbf{V}'$ is of order of ϵ since $\mathbf{V}'$ is exclusively caused by the density difference. When splitting the density term as $\rho = \rho_0 + \Delta\rho$ and apply the Boussinesq approximation ($\Delta\rho \ll \rho$) to the Eq. (2.1), the product of $\Delta\rho D\mathbf{V}'/Dt$ is of the order of ϵ^2 and was dropped in the magnitude analysis as shown in Chapter 2.

It has been simply specified that the relationships (2.22) could be used in transforming the momentum equation in the rotating coordinate system to the non-rotating coordinate system. If the momentum equation is deduced directly in the non-rotating coordinate system, the terrestrial gravity is the only body force on fluid.

$$\rho\frac{D\bar{\mathbf{V}}'}{D\bar{t}'} = -\nabla p' + \rho\mathbf{g}' + \mu\nabla^2\bar{\mathbf{V}}' \tag{A.1}$$

A question arises: how can one obtain from Eq. (A.1) a term equivalent to that based on the centrifugal force in Eq. (2.1)? To handle this problem, it has to be considered that Eq. (A.1) involves a mixed convection type problem. This means that the velocity $\bar{\mathbf{V}}'$ involved in the acceleration term may be expressed as follows

$$\bar{\mathbf{V}}' = \mathbf{V}' + \boldsymbol{\Omega}' \times \bar{\mathbf{r}}' \tag{A.2}$$

in which $\mathbf{V}'$ is the velocity relative to the boundary, i.e., caused exclusively by the density difference of fluid and $\boldsymbol{\Omega}' \times \bar{\mathbf{r}}'$ ($\bar{\mathbf{r}}' = \mathbf{r}'$), the azimuthal velocity corresponding

to solid body rotation entrained by the rotating boundary of the cylinder. Among these two terms, only $\mathbf{V}'$ can be set to the order of ϵ, according to the approach given in section 2.1.

In order to obtain the equivalent term mentioned above, one needs to explicit the term $D(\mathbf{V}'+\mathbf{\Omega}'\times\bar{\mathbf{r}}')/d\bar{t}'$ in the present coordinate system. Let us start by looking at an arbitrary vector $\mathbf{A}$ being fixed in a moving frame (x, y) which is rotating at an angular velocity $\mathbf{\Omega}'$ with respect to the non-rotating coordinate system $(\bar{x}, \bar{y})$. (x, y) and $(\bar{x}, \bar{y})$ have a same origin O. $\mathbf{i}$ and $\mathbf{j}$ are unit vectors along with two coordinate axes x and y, respectively. Thus $\mathbf{A}$ can be expressed in the system (x, y) as

$$\mathbf{A} = A_x\mathbf{i} + A_y\mathbf{j} \tag{A.3}$$

The material derivative of $\mathbf{A}$ in the coordinate system $(\bar{x}, \bar{y})$ is

$$\frac{d\mathbf{A}}{dt} = \frac{dA_x}{dt}\mathbf{i} + \frac{dA_y}{dt}\mathbf{j} + A_x\frac{d\mathbf{i}}{dt} + A_y\frac{d\mathbf{j}}{dt} \tag{A.4}$$

When being viewed from the coordinate system (x, y), $\mathbf{i}$ and $\mathbf{j}$ are rotating at a same angular velocity $\mathbf{\Omega}'$. We therefore have

$$\begin{cases} \dfrac{d\mathbf{i}}{dt} = \mathbf{\Omega}\times\mathbf{i} \\ \dfrac{d\mathbf{j}}{dt} = \mathbf{\Omega}\times\mathbf{j} \end{cases} \tag{A.5}$$

Substituting Eq. (A.5) into (A.4) yields

$$\frac{d\mathbf{A}}{dt} = \frac{d^*\mathbf{A}}{dt} + \mathbf{\Omega}\times\mathbf{A} \tag{A.6}$$

where the first term in the right-hand side stands for the material derivative of $\mathbf{A}$ in the system (x, y)

$$\frac{d^*\mathbf{A}}{dt} = \frac{dA_x}{dt}\mathbf{i} + \frac{dA_y}{dt}\mathbf{j} \tag{A.7}$$

Now let us keep (A.6) in mind and come back to the present problem. Applying Eq. (A.6) to vector $\bar{\mathbf{r}}'$ yields

$$\bar{\mathbf{V}}' = \frac{d\,\bar{\mathbf{r}}'}{d\bar{t}'} = \frac{d^*\,\bar{\mathbf{r}}'}{d\bar{t}'} + \boldsymbol{\Omega}' \times \bar{\mathbf{r}}' \tag{A.8}$$

where

$$\frac{d^*\,\bar{\mathbf{r}}'}{d\bar{t}'} = \mathbf{V}' \tag{A.9}$$

$\mathbf{V}'$ being the velocity vector in the rotating coordinate system. It should be noticed that Eq. (A.8) is identical to Eq. (A.2).

Applying Eq. (A.6) to vector $\bar{\mathbf{V}}'$ reads

$$\frac{d\bar{\mathbf{V}}'}{d\bar{t}'} = \frac{d^*\bar{\mathbf{V}}'}{d\bar{t}'} + \boldsymbol{\Omega}' \times \bar{\mathbf{V}}' \tag{A.10}$$

Replacing $\bar{\mathbf{V}}$ in (A.10) with the expression (A.8) leads to

$$\begin{aligned} \frac{d\bar{\mathbf{V}}'}{d\bar{t}'} &= \frac{d^{2*}\bar{\mathbf{r}}'}{d\bar{t}'^2} + \frac{d^*\boldsymbol{\Omega}'}{d\bar{t}'} \times \bar{\mathbf{r}}' + \boldsymbol{\Omega}' \times \frac{d^*\bar{\mathbf{r}}'}{d\bar{t}'} + \boldsymbol{\Omega}' \times (\frac{d^*\bar{\mathbf{r}}'}{d\bar{t}'} + \boldsymbol{\Omega}' \times \bar{\mathbf{r}}') \\ &= \frac{d^{2*}\bar{\mathbf{r}}'}{d\bar{t}'^2} + \frac{d^*\boldsymbol{\Omega}'}{d\bar{t}'} \times \bar{\mathbf{r}}' + \boldsymbol{\Omega}' \times (\boldsymbol{\Omega}' \times \bar{\mathbf{r}}') + 2\boldsymbol{\Omega}' \times \frac{d^*\bar{\mathbf{r}}'}{d\bar{t}'} \end{aligned} \tag{A.11}$$

Considering a constant angular velocity and multiplying (A.11) by density ρ, one obtains

$$\rho\frac{d\bar{\mathbf{V}}'}{d\bar{t}'} = \rho\frac{d\mathbf{V}'}{d\bar{t}'} + \rho\boldsymbol{\Omega}' \times (\boldsymbol{\Omega}' \times \bar{\mathbf{r}}') + 2\rho\boldsymbol{\Omega}' \times \mathbf{V}' \tag{A.12}$$

Equation (A.12) evidences that the acceleration term of the momentum equation in the non-rotating coordinate system can be split into three parts and that the last two parts are equivalent to the centrifugal and Coriolis force terms of Eq. (2.1) in the rotating coordinate system.

Moreover, when one splits the density term as $\rho = \rho_0 + \Delta\rho$ and applies the Boussinesq approximation ($\Delta\rho \ll \rho$) to the Eq. (A.1), the term

$$\Delta\rho\frac{d\bar{\mathbf{V}}'}{d\bar{t}'} = \Delta\rho[\frac{d\mathbf{V}'}{d\bar{t}'} + \boldsymbol{\Omega}' \times (\boldsymbol{\Omega}' \times \bar{\mathbf{r}}') + 2\boldsymbol{\Omega}' \times \mathbf{V}'] \tag{A.13}$$

is not of the order of ϵ^2 and can not be dropped in the magnitude analysis as shown in Chapter 2. Consequently the term $\Delta\rho\boldsymbol{\Omega}' \times (\boldsymbol{\Omega}' \times \bar{\mathbf{r}}')$ is turned into a correspondence of the centrifugal force-based source term that appears on the right-hand side of Eq. (2.9) based on the rotating coordinate system.

Appendix B

GOVERNING EQUATIONS IN THE NON-ROTATING COORDINATE SYSTEM

Aside from the transformation described in section 2.2.2, the governing equations (2.42) and (2.43) for isotropic porous medium can be directly expressed in the non-rotating coordinate system shown in Fig. 2.2*b*.

B.1 Darcy Equation

Similar to Eq.(2.27), the Darcy equation in the non-rotating coordinate system without the centrifugal force reads

$$\bar{\mathbf{V}}' = \mathbf{V}' + \mathbf{\Omega}' \times \bar{\mathbf{r}}' = -\frac{K}{\mu}[\rho\beta(T' - T_0')\,\mathbf{g}' + \nabla p'] \tag{B.1}$$

in which $\mathbf{V}'$ is the filtration velocity and $\mathbf{\Omega}' \times \bar{\mathbf{r}}'$, the azimuthal velocity of the rigid matrix. With the expression of $\hat{\mathbf{g}} = \hat{\mathbf{r}}\cos\bar{\theta} - \hat{\theta}\sin\bar{\theta}$, its component form is

$$\begin{cases} \bar{u}' = -\dfrac{K}{\nu} g\beta(\bar{T}' - T_0')\cos\bar{\theta} - \dfrac{K}{\mu}\dfrac{\partial \bar{p}'}{\partial \bar{r}'} \\ \bar{v}' - \Omega'\bar{r}' = \dfrac{K}{\nu} g\beta(\bar{T}' - T_0')\sin\bar{\theta} - \dfrac{K}{\mu}\dfrac{\partial \bar{p}'}{\bar{r}'\partial\bar{\theta}} \end{cases} \tag{B.2}$$

Taking the curl of (B.2) yields

$$\frac{1}{\bar{r}'}\frac{\partial}{\partial \bar{r}'}\left(\bar{r}'\frac{\partial \bar{\psi}'}{\partial \bar{r}'}\right) + \frac{1}{\bar{r}'^2}\frac{\partial^2 \bar{\psi}'}{\partial \bar{\theta}^2} = -2\Omega' - \frac{Kg\beta}{\nu}\left[\sin\bar{\theta}\frac{\partial(\bar{T}' - T_0')}{\partial \bar{r}'} + \frac{\cos\bar{\theta}}{\bar{r}'}\frac{\partial(\bar{T}' - T_0')}{\partial\bar{\theta}}\right] \tag{B.3}$$

B.2 Energy Equation

In order to deduce properly the energy equation for the non-rotating coordinate system in which the solid (or rigid) matrix moves, a fixed control volume in a polar

coordinate system that is tied to the ground is considered, as illustrated in Fig. $B.1$. The heat flux crossing the border of the control volume will now be discussed separately. $\Delta Q'$ is used to represent the net heat flux.

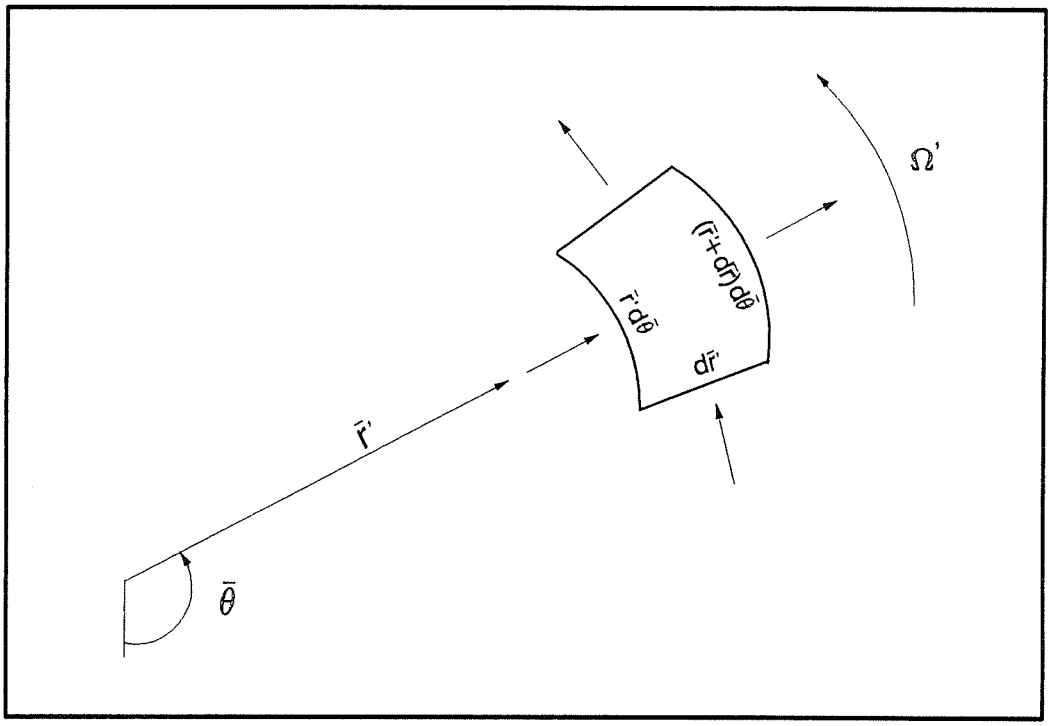

Figure: $B.1$ Sketch of the control volume

θ-direction:

a) Heat transport due to solid body rotation of saturated porous medium (fluid and solid matrix) in a steady angular speed Ω' (in counterclockwise direction)

$$\Delta Q'_a = (\rho c)_p \Omega' \bar{r}' [\bar{T}' + \frac{\partial \bar{T}'}{\partial \bar{\theta}} d\bar{\theta}] d\bar{r}' - (\rho c)_p \Omega' \bar{r}' \bar{T}' d\bar{r}' = (\rho c)_p \Omega' \frac{\partial \bar{T}'}{\partial \bar{\theta}} \bar{r}' d\bar{r}' d\bar{\theta}' \qquad \text{(B.4)}$$

b) Heat transport due to fluid velocity relative to the solid matrix v'_r (v'_r is filtration velocity and $v'_r = \bar{v}' - \Omega' \bar{r}'$)

$$\Delta Q'_b = (\rho c)_f [v'_r \bar{T}' + \frac{\partial v'_r \bar{T}'}{\partial \bar{\theta}} d\bar{\theta}] d\bar{r}' - (\rho c)_f v'_r \bar{T}' d\bar{r}' = (\rho c)_f \frac{\partial v'_r \bar{T}'}{\bar{r}' \partial \bar{\theta}} \bar{r}' d\bar{r}' d\bar{\theta} \quad \text{(B.5)}$$

c) Heat conduction

$$\Delta Q'_c = [-k \frac{\partial \bar{T}'}{\bar{r}' \partial \bar{\theta}} - k \frac{\partial^2 \bar{T}'}{\bar{r}' \partial \bar{\theta}^2} d\bar{\theta}] d\bar{r}' - (-k \frac{\partial \bar{T}'}{\bar{r}' \partial \bar{\theta}'} d\bar{r}') = -\frac{k}{\bar{r}'^2} \frac{\partial^2 \bar{T}'}{\bar{r}' \partial \bar{\theta}^2} \bar{r}' d\bar{r}' d\bar{\theta}' \quad \text{(B.6)}$$

<u>*r*-direction:</u>

d) Heat convection in fluid

$$\Delta Q'_d = (\rho c)_f [\bar{r}' \bar{u}' \bar{T}' + \frac{\partial \bar{r}' \bar{u}' \bar{T}'}{\partial \bar{r}'} d\bar{r}'] d\bar{\theta} - (\rho c)_f \bar{r}' \bar{u}' \bar{T}' d\bar{\theta} = \frac{(\rho c)_f}{\bar{r}'} \frac{\partial \bar{r}' \bar{u}' \bar{T}'}{\partial \bar{r}'} \bar{r}' d\bar{r}' d\bar{\theta} \quad \text{(B.7)}$$

e) Heat conduction

$$\begin{aligned} \Delta Q'_e &= [-k \frac{\partial \bar{T}'}{\partial \bar{r}'} \bar{r}' - k \frac{\partial}{\partial \bar{r}'} (\bar{r}' \frac{\partial \bar{T}'}{\partial \bar{r}'}) d\bar{r}'] d\bar{\theta} - (-k \frac{\partial \bar{T}'}{\partial \bar{r}'} \bar{r}' d\bar{\theta}) \\ &= -\frac{k}{\bar{r}'} \frac{\partial}{\partial \bar{r}'} (\bar{r}' \frac{\partial \bar{T}'}{\partial \bar{r}'}) \bar{r}' d\bar{r}' d\bar{\theta} \end{aligned} \quad \text{(B.8)}$$

At last, the rate of heat increase inside the control volume $\bar{r}' d\bar{r}' d\bar{\theta}$ is expressed as

$$(\rho c)_p \frac{\partial \bar{T}'}{\partial \bar{t}'} \bar{r}' d\bar{r}' d\bar{\theta} \quad \text{(B.9)}$$

Considering an uniformly distributed heat sink S' and applying energy conservation in the control volume, one obtains

$$(\rho c)_p \frac{\partial \bar{T}'}{\partial \bar{t}'} \bar{r}' d\bar{r}' d\bar{\theta} + \sum \Delta Q' + S' = 0 \quad \text{(B.10)}$$

Substituting all the terms into (B.10) and dividing by $\bar{r}' d\bar{r}' d\bar{\theta}$ produce

$$\begin{aligned} (\rho c)_p \frac{\partial \bar{T}'}{\partial \bar{t}'} + (\rho c)_f [\frac{\partial \bar{r}' \bar{u}' \bar{T}'}{\bar{r}' \partial \bar{r}'} + \frac{\partial v'_r \bar{T}'}{\bar{r}' \partial \bar{\theta}}] + (\rho c)_p \Omega' \frac{\partial \bar{T}'}{\partial \bar{\theta}} \\ = k [\frac{\partial}{\bar{r}' \partial \bar{r}'} (\bar{r}' \frac{\partial \bar{T}'}{\partial \bar{r}'}) + \frac{\partial^2 \bar{T}'}{\bar{r}'^2 \partial \bar{\theta}^2}] - S' \end{aligned} \quad \text{(B.11)}$$

Since $v_r' = \bar{v}' - \Omega' \bar{r}'$

$$(\rho c)_p \frac{\partial \bar{T}'}{\partial \bar{t}'} + (\rho c)_f [\frac{\partial \bar{r}' \bar{u}' \bar{T}'}{\bar{r}' \partial \bar{r}'} + \frac{\partial \bar{v}' \bar{T}'}{\bar{r}' \partial \bar{\theta}'}] + [(\rho c)_p - (\rho c)_f] \Omega' \frac{\partial \bar{T}'}{\partial \bar{\theta}} = k \nabla^2 \bar{T}' - S' \quad \text{(B.12)}$$

Making use of the continuity equation (2.38)

$$(\rho c)_p \frac{\partial \bar{T}'}{\partial \bar{t}'} + (\rho c)_f [\bar{u}' \frac{\partial \bar{T}'}{\partial \bar{r}'} + \frac{\bar{v}'}{\bar{r}'} \frac{\partial \bar{T}'}{\partial \bar{\theta}}] + [(\rho c)_p - (\rho c)_f] \Omega' \frac{\partial \bar{T}'}{\partial \bar{\theta}} = k \nabla^2 \bar{T}' - S' \quad \text{(B.13)}$$

Dividing by $(\rho c)_f$ and using the definitions $\sigma = (\rho c)_p / (\rho c)_f$ and $\alpha = k/(\rho c)_f$ yields

$$\sigma \frac{\partial \bar{T}'}{\partial \bar{t}'} + \bar{u}' \frac{\partial \bar{T}'}{\partial \bar{r}'} + \frac{\bar{v}'}{\bar{r}'} \frac{\partial \bar{T}'}{\partial \bar{\theta}} + (\sigma - 1) \Omega' \frac{\partial \bar{T}'}{\partial \bar{\theta}} = \alpha \nabla^2 \bar{T}' - S'/(\rho c)_f \quad \text{(B.14)}$$

B.3 Dimensionless Form

With the following dimensionless variables

$\bar{r} = \bar{r}'/r_0'$

$\bar{t} = \bar{t}' \alpha / \sigma r_0'^2$

$(\bar{u}, \bar{v}) = (\bar{u}', \bar{v}') r_0'/\alpha$

$Pe^* = \sigma \Omega' \bar{r}_0'^2/\alpha$

$\bar{p} = \bar{p}_d' K/\alpha\mu$

$\bar{T} = (\bar{T}' - T_0')/\Delta T'$

$\Delta T' = S' r_0'^2/k$

$\bar{\psi} = \bar{\psi}'/\alpha$

Equations (B.2), (B.3) and (B.14) become in dimensionless form

$$\begin{cases} \bar{u} = -Ra\, \bar{T} \cos\bar{\theta} - \dfrac{\partial \bar{p}}{\partial \bar{r}} \\ \bar{v} - \dfrac{Pe^* \bar{r}}{\sigma} = Ra\, \bar{T} \sin\bar{\theta} - \dfrac{\partial \bar{p}}{\bar{r} \partial \bar{\theta}} \end{cases} \quad \text{(B.15)}$$

$$\frac{1}{\bar{r}}\frac{\partial}{\partial\bar{r}}(\bar{r}\frac{\partial\bar{\psi}}{\partial\bar{r}})+\frac{1}{\bar{r}^2}\frac{\partial^2\bar{\psi}}{\partial\bar{\theta}^2}=-2\frac{Pe^*}{\sigma}-Ra\,(\sin\bar{\theta}\frac{\partial\bar{T}}{\partial\bar{r}}+\frac{\cos\bar{\theta}}{\bar{r}}\frac{\partial\bar{T}}{\partial\bar{\theta}}) \tag{B.16}$$

$$\frac{\partial\bar{T}}{\partial\bar{t}}+\bar{u}\frac{\partial\bar{T}}{\partial\bar{r}}+\frac{\bar{v}}{\bar{r}}\frac{\partial\bar{T}}{\partial\bar{\theta}}+Pe^*\bar{r}\,(1-\frac{1}{\sigma})\frac{\partial\bar{T}}{\bar{r}\partial\bar{\theta}}=\nabla^2\bar{T}-1 \tag{B.17}$$

σ appears in $\bar{\theta}$-component of Darcy equation, energy equation and stream function equation. In order to eliminate σ $\bar{v}$ and $\bar{\psi}$ are redefined

$$\begin{cases}\bar{\bar{v}}=\bar{v}+Pe^*\bar{r}\,(1-\dfrac{1}{\sigma})\\ \bar{\bar{\psi}}=\bar{\psi}-\dfrac{Pe^*\bar{r}^2}{2}(1-\dfrac{1}{\sigma})\end{cases} \tag{B.18}$$

Finally Eqs. (B.15), (B.16) and (B.17) change to

$$\begin{cases}\bar{u}=-Ra\,\bar{T}\cos\bar{\theta}-\dfrac{\partial\bar{p}}{\partial\bar{r}}\\ \bar{\bar{v}}-Pe^*\bar{r}=Ra\,\bar{T}\sin\bar{\theta}-\dfrac{\partial\bar{p}}{\bar{r}\partial\bar{\theta}}\end{cases} \tag{B.19}$$

$$\nabla^2\bar{\bar{\psi}}=-2\,Pe^*-Ra\,(\sin\bar{\theta}\frac{\partial\bar{T}}{\partial\bar{r}}+\frac{\cos\bar{\theta}}{\bar{r}}\frac{\partial\bar{T}}{\partial\bar{\theta}}) \tag{B.20}$$

$$\frac{\partial\bar{T}}{\partial\bar{t}}+\bar{u}\frac{\partial\bar{T}}{\partial\bar{r}}+\frac{\bar{\bar{v}}}{\bar{r}}\frac{\partial\bar{T}}{\partial\bar{\theta}}=\nabla^2\bar{T}-1 \tag{B.21}$$

Thus the σ is incorporated in the definition of $\bar{\bar{v}}$ and $\bar{\bar{\psi}}$. Equations (B.20) and (B.21) correspond to Eqs. (2.42) and (2.43) where $\bar{v}$ instead of $\bar{\bar{v}}$ is used. It is obvious that when one wants to recover a dimensional velocity from $\bar{\bar{v}}$ in Eqs. (2.42) and (2.43), the product $\bar{\bar{v}}(\alpha/r_0')$ does not correspond to the sum of the (dimensional) filtration velocity and the (dimensional) azimuthal velocity of the rigid matrix.

As a conclusion, an appropriate definition of the dimensionless velocity component in $\bar{\theta}$-direction and of the stream function provides a form of the governing equations where σ does not appear explicitly.

Appendix C

MATRIX PARTITION PROCEDURE

Let us consider the equation

$$\mathbf{A}\,\mathbf{X} = \mathbf{B} \tag{C.1}$$

where $\mathbf{X}$ and $\mathbf{B}$ are vectors and $\mathbf{A}$ is a $(m \times m)$ tridiagonal matrix, except for the non-zero terms a_{1m} and a_{m1}, which arise from periodicity condition (3.13)

Eq. $(C.1)$ may be written as

$$\begin{bmatrix} \mathbf{C} & \mathbf{D} \\ \mathbf{E} & F \end{bmatrix} \cdot \left(\begin{Bmatrix} \mathbf{X}^{+} \\ X_m \end{Bmatrix} + \begin{Bmatrix} \mathbf{X}^{-} \\ 0 \end{Bmatrix} \right) = \begin{Bmatrix} \mathbf{G} \\ G_m \end{Bmatrix} \tag{C.2}$$

where $\mathbf{C}$ is a tridiagonal $((m-1) \times (m-1))$ matrix; $\mathbf{D}$ and $\mathbf{G}$ are column vectors and $\mathbf{E}$ is a row vector, all of dimension $(m-1)$. Except for its last term X_m, the unknown vector $\mathbf{X}$ is expressed as the sum of two vectors $\mathbf{X}^{+}$ and $\mathbf{X}^{-}$ of dimension $(m-1)$. The vector $\mathbf{G}$ corresponds to the first $(m-1)$ terms of $\mathbf{B}$. X_m, F and G_m are scalars.

The $(m-1)$ vector $\mathbf{X}^{*}$ is defined as

$$\mathbf{X}^* = -\mathbf{X}^+/X_m \tag{C.3}$$

The following equations

$$\mathbf{C}\,\mathbf{X}^+ = \mathbf{G} \tag{C.4}$$

and

$$\mathbf{C}\,\mathbf{X}^* = \mathbf{D} \tag{C.5}$$

may be solved easily for $\mathbf{X}^+$ and $\mathbf{X}^*$ by recurrence formulas applicable to tridiagonal matrices such as the Thomas algorithm. The solution of the last row of $(C.2)$ provides the value X_m

$$X_m = \frac{(G_m - \mathbf{E}\,\mathbf{X}^+)}{(F - \mathbf{E}\,\mathbf{X}^*)} \tag{C.6}$$

Finally the solution vector $\mathbf{X}$ is given by

$$\left\{ \begin{array}{c} \\ \mathbf{X} \\ \\ \end{array} \right\} = \left\{ \begin{array}{c} \mathbf{X}^+ \\ \\ X_m \end{array} \right\} - X_m \left\{ \begin{array}{c} \mathbf{X}^* \\ \\ 0 \end{array} \right\} \tag{C.7}$$

Appendix D

COEFFICIENTS IN PERTURBATION SOLUTION

The coefficients generated in the perturbation method for a low rotation cylinder of fluid medium in section 4.2 are given in this appendix.

For practical purposes, the series (4.34) and (4.35) are approximated by the first three terms and first two terms, respectively, such that

$$\begin{aligned} \psi &= \psi_0 + Ra\psi_1 + Ra^2\psi_2 \\ &= \psi_0 + Ra(f_0 + Re\, f_1) + Ra^2(h_0 + Re\, h_1) \qquad \text{(D.1)} \\ T &= T_0 + RaT_1 \\ &= T_0 + Ra(g_0 + Re\, g_1) \qquad \text{(D.2)} \end{aligned}$$

According to section 4.2,

$$\begin{cases} \psi_0 = 0 \\ T_0 = (r^2 - 1)/4 \end{cases} \qquad \text{(D.3)}$$

$$\begin{cases} f_0 = \sin\phi(a_1^0 r + a_2^0 r^3 + a_3^0 r^5) \\ f_1 = \cos\phi(a_1^1 r + a_2^1 r^3 + a_3^1 r^5 + a_4^1 r^7) \end{cases} \qquad \text{(D.4)}$$

$$\begin{cases} g_0 = \cos\phi(b_1^0 r + b_2^0 r^3 + b_3^0 r^5 + b_4^0 r^7) \\ g_1 = \sin\phi(b_1^1 r + b_2^1 r^3 + b_3^1 r^5 + b_4^1 r^7 + b_5^1 r^9) \end{cases} \qquad \text{(D.5)}$$

The term h_0 vanishes due to its angular dependence at $r = 0$. Only h_1 contains terms which are independent of ϕ and therefore is given

$$h_1 = a_0^2 + a_1^2 r^2 + a_2^2 r^4 + a_3^2 r^6 + a_4^2 r^8 + a_5^2 r^{10} + a_6^2 r^{12} \tag{D.6}$$

At the center of cylinder ($r = 0$), Eq. (D.1) becomes

$$\psi|_{r=0} = \psi_c = a_0^2 \, Re \, Ra^2 = C \, Re \, Ra^2 \tag{D.7}$$

The coefficients leading to a_0^2 or C are listed

$$\begin{cases} a_0^2 = a_2^2 + 2a_3^2 + 3a_4^2 + 4a_5^2 + 5a_6^2 \\ a_1^2 = -(2a_2^2 + 3a_3^2 + 4a_4^2 + 5a_5^2 + 6a_6^2) \\ a_2^2 = a_0/64 \\ a_3^2 = a_1/576 \\ a_4^2 = a_2/2304 \\ a_5^2 = a_3/6400 \\ a_6^2 = a_4/14400 \end{cases} \tag{D.8}$$

$$\begin{cases} a_0 = [8(a_1^0 \times a_2^1 - a_2^0 + a_1^1) + b_1^1]/Pr \\ a_1 = [48(a_1^0 \times a_3^1 - a_3^0 + a_1^1) + 2b_2^1]/Pr \\ a_2 = (144a_1^0 \times a_4^1 + 48a_2^0 \times a_3^1 - 48a_3^0 \times a_2^1 + 3b_3^1)/Pr \\ a_3 = (160a_2^0 \times a_4^1 + 4b_4^1)/Pr \\ a_4 = (120a_3^0 \times a_4^1 + 5b_5^1)/Pr \end{cases} \tag{D.9}$$

$$\begin{cases} b_1^1 = -(b_2^1 + b_3^1 + + b_4^1 + b_5^1) \\ b_2^1 = -(Pr\, b_1^0 + a_1^1/2)/8 \\ b_3^1 = -(Pr\, b_2^0 + a_2^1/2)/24 \\ b_4^1 = -(Pr\, b_3^0 + a_3^1/2)/48 \\ b_5^1 = -(Pr\, b_4^0 + a_4^1/2)/80 \end{cases} \tag{D.10}$$

$$\begin{cases} b_1^0 = -(a_1^0/16 + a_2^0/48 + a_3^0/96) \\ b_2^0 = a_1^0/16 \\ b_3^0 = a_2^0/48 \\ b_4^0 = a_3^0/96 \end{cases} \tag{D.11}$$

$$\begin{cases} a_1^1 = a_2^0/24 + a_3^0/24 \\ a_2^1 = -(a_2^0/12 + a_3^0/16) \\ a_3^1 = a_2^0/24 \\ a_3^1 = a_3^0/48 \end{cases} \tag{D.12}$$

$$\begin{cases} a_1^0 = 1/384 \\ a_2^0 = -1/192 \\ a_3^0 = 1/384 \end{cases} \tag{D.13}$$